CRACOW UNIVERSITY OF
TECHNOLOGY
FACULTY OF MECHANICAL ENGINEERING
INSTITUTE OF APPLIED MECHANICS

CONSTITUTIVE MODELLING OF FUNCTIONALLY GRADED MATERIALS FOR LOW TEMPERATURE STRUCTURAL APPLICATIONS

Monika Sitko

Supervisor: prof. dr hab. inż. Błażej Skoczeń

Kraków 2011

TABLE OF CONTENTS

ACKNOWLEDGEMENTS

I would like to express sincere gratitude to my supervisor prof. Błażej Skoczeń for encouraging me to work on constitutive modelling of materials and phenomena related to cryogenic temperatures. I am grateful for many inspiring discussions and suggestions concerning the Thesis. I would also like to thank dr Adam Wróblewski for help in applying finite element numerical procedures.

I would like to thank my family and friends, especially my parents, brother and sister, for motivation, support and understanding during writing the Thesis.

NOTATION

SCALARS AND SCALAR FUNCTIONS

A_f - austenite finish temperature

A_s - austenite start temperature

C_0 - linear hardening parameter

E - Young's modulus

E_t - tangent stiffness modulus

F - Helmholtz free energy

G - Gibbs free energy or shear modulus (depending on the context)

H - enthalpy or the Heavyside step function (depending on the context)

J_2 - second invariant of stress tensor

k - bulk modulus

k_m - bulk modulus of martensite

k_{MT} - bulk modulus obtained by Mori-Tanaka homogenisation

k_{ta} - tangent bulk modulus of austenite

M_f - martensite finish temperature

M_s - martensite start temperature

p - pressure or accumulated plastic strain (depending on the context)

R - isotropic hardening parameter

S - entropy

T - temperature

T_e - equilibrium temperature

U - internal energy

V - volume

α' - body-centred-cubic structure; martensite

β - Bauschinger parameter

γ - face-centred-cubic structure; austenite

ε_0 - strain at yield point

ε_L^p - plastic strain at saturation of phase transformation

ε_ξ^p - plastic strain at the onset of phase transformation

μ - shear modulus

μ_m - shear modulus of martensite

μ_{MT} - shear modulus obtained by Mori-Tanaka homogenisation

μ_{ta} - tangent shear modulus of austenite

ν - Poisson's ratio

ν_a - Poisson's ratio of austenite

ν_m - Poisson's ratio of martensite

ξ - volume fraction of martensite

ξ_L - saturation level of volume fraction of martensite

σ_0 - yield stress

τ - shear stress

2ND RANK TENSORS

$\underline{\underline{s}}$ - stress deviator

$\underline{\underline{X}}$ - back stress tensor

$\underline{\underline{\varepsilon}}$ - strain tensor

$\underline{\underline{\varepsilon}}^{bs}$ - Bain strain tensor

$\underline{\underline{\varepsilon}}^{p}$ - plastic strain tensor

$\underline{\underline{\varepsilon}}^{th}$ - thermal strain tensor

$\underline{\underline{\sigma}}$ - stress tensor

4$^{\text{TH}}$ RANK TENSORS

$\underline{\underline{\underline{\underline{E}}}}$ - stiffness tensor

$\underline{\underline{\underline{\underline{E}}}}_{\text{eff}}$ - effective stiffness tensor

$\underline{\underline{\underline{\underline{E}}}}_{\text{m}}$ - stiffness tensor of martensite

$\underline{\underline{\underline{\underline{E}}}}_{\text{MT}}$ - effective stiffness tensor obtained by Mori-Tanaka homogenisation

$\underline{\underline{\underline{\underline{E}}}}_{\text{ta}}$ - tangent stiffness tensor of austenite

$\underline{\underline{\underline{\underline{I}}}}$ - identity tensor

$\underline{\underline{\underline{\underline{J}}}}$ - projector representing hydrostatic state

$\underline{\underline{\underline{\underline{K}}}}$ - projector representing shear state

ABBREVIATIONS

b.c.c. - body-centred-cubic

b.c.t. - body-centred-tetragonal

f.c.c. - face-centred-cubic

FEM - finite element method

FGM - functionally graded materials

FGSM - functionally graded structural member

RVE - representative volume element

TRIP - transformation-induced plasticity

UPF's - user programmable features

1. INTRODUCTION

1.1. Structural materials in cryogenic applications

Nowadays cryogenic technologies are more commonly implemented in various engineering applications. Initially, they were reserved only for scientific laboratories but currently cryogenics is also used in medicine as well as industry and is strongly combined with superconductivity, which is employed in such devices as particle accelerators or modern magnetic trains [1]. Ever increasing interest in applications of low temperatures imposes on engineers the requirement of designing structures working in extreme conditions. The choice of structural materials which assure reliable functioning of structures is crucial [2].

Response of materials at cryogenic temperatures is often contradictory with respect to room temperature experience. For instance, materials such as polymers or rubbers, which are usually elastic at room temperatures, become brittle and can be easily damaged when cooled down to cryogenic temperatures. Fracture toughness is always fundamental and one of the most important factors in choosing the material to cryogenic structural applications. One of the reasons of metallic materials embrittlement at low temperatures is the body-centred-cubic (b.c.c.) crystalline structure. Therefore, carbon steels, ferritic steels or iron – the most popular engineering materials characterized by the b.c.c. structure – should not be used at cryogenic temperatures and should be avoided especially in structures carrying loads.

The materials that remain ductile and can work even at extremely low temperatures are characterized by the face-centred-cubic (f.c.c.) crystalline structure. To this group of materials belong among others aluminium, copper, lead, nickel and brass. Nevertheless, the most often used structural materials for cryogenic applications are type AISI 300 stainless steels, especially metastable 304 and 316 alloys (*Tab. 1.1*) [3]. The austenitic stainless steels are known as materials with high ductility, low yield stress and relatively high ultimate tensile strength in comparison with typical carbon steels. High contents of chromium (at least 11 wt. %) and nickel (minimum 8 wt. %) suppress the transformation on cooling to a mixture of ferrite and cementite, keeping the material fully austenitic. Due to the corrosion resistance and very good mechanical properties, austenitic stainless steels are often used in civil, automotive, aerospace and chemical engineering, as industrial equipment, surgical instruments and in many other common applications.

Table 1.1: Chemical composition of typical AISI 300 stainless steels.

AISI type	C % max	Cr %	Ni %	Mn % max	N %	Other
304	0.08	18-20	8-12	2	-	-
304L	0.03	18-20	8-12	2	-	-
304LN	0.03	18-20	8-12	2	0.10-0.16	1% Si max 10.6 % P max 0.03 % S max
316	0.08	16-18	10-14	2	-	-
316L	0.03	16-18	10-14	2	-	-
316LN	0.03	16-18	10-14	2	0.10-0.16	1% Si max 10.6 % P max 0.03 % S max

Mechanical properties of the most common materials at cryogenic temperatures differ from room temperature properties [3]. The Young modulus, the yield and the ultimate stresses usually increase with decreasing temperature, though the yield stress depends significantly on material processing. Fatigue behaviour of the f.c.c. materials seems to change in favour of low temperatures. Thermal contraction of materials changes non-linearly below room temperature. The biggest thermal contraction appears down to 50-70K, further cooling causes minor contraction.

Properties of austenitic stainless steels at cryogenic temperatures can be modified by changing the alloy composition and by thermomechanical processing [4]. Strength of the material can be increased by adding nitrogen. Steels with higher nitrogen content tend to have higher yield strength. Addition of nitrogen through alloying is an easy and cheap method of improving the low-temperature properties of steel. The influence of nitrogen content is especially significant in liquid helium temperature range (~ 4K). Reducing grain size and cold working also result in strengthening of steels. Toughness of the austenitic steels can be strongly enhanced by adding nickel. The nickel content beyond 8 wt. % increases the ductility at low temperatures, the stability of the austenite and the stacking-fault energy.

Most of the austenitic stainless steels are metastable at cryogenic temperatures, which means that they can undergo phase transformation from f.c.c. to b.c.c. structure [5]. Complete, spontaneous phase transformation is disadvantageous and can lead to structure damage. However, controlled strain-induced phase transformation, carried out in the most loaded regions, causes nucleation of hard martensitic inclusions in a soft austenitic matrix. These inclusions increase strength of the material due to their elastic properties and capability of interacting with dislocations. It enables us to create structures with functionally graded properties varying from the austenitic elastic-plastic part to the two-phase austenitic-martensitic regions.

1.2. Thermodynamic fundamentals of phase transformations

Phase transition can be defined as a change in macroscopic configuration of atoms or molecules caused by change of thermodynamic variables characterizing the system, such as temperature, pressure or magnetic field. A phase is understood here as homogeneous microstructure, having identical properties and defined boundaries.

Thermodynamic state of a system can by described by means of four scalar functions of natural variables that are known as thermodynamic potentials: internal energy, enthalpy, Helmholtz free energy and Gibbs free energy [6]. If a system is described in terms of thermodynamic potential, all the thermodynamic properties of the system can be determined by computing partial derivatives of this potential function with respect to its natural variables. On the other hand, if all state functions of the system are known, the potentials can be calculated by integration. This type of description is useful in the case of complex systems undergoing transitions such as chemical reactions or phase transformations.

The internal energy U is a sum of the kinetic energy associated with motion of molecules and the potential energy associated with the interaction between molecules by means of the atomic forces.

The enthalpy H consists of energy and work done by the system with respect to its surrounding, expressed as the product of pressure p and volume V, often called flow work:

$$H = U + pV \tag{1.1}$$

The Helmholtz free energy F is a thermodynamic potential that defines the amount of work obtained from a closed system with constant temperature T and volume V:

$$F = U - TS \tag{1.2}$$

where S is the entropy.

The Gibbs free energy G constitutes a thermodynamic potential that expresses the maximum amount of work which can be extracted from a closed system with constant temperature T and pressure p, defined as:

$$G = H - TS = U + pV - TS \tag{1.3}$$

Stability of a system corresponds to minimum of potentials F (for constant temperature and volume) and G (for constant temperature and pressure). Undergoing phase transition means that for given conditions the thermodynamic potential of one phase becomes lower than of the other phase. Thus, if the system is described in terms of Gibbs free energy and each phase is represented by a surface, the phase transition takes place at the point where the surfaces cross each other. *Figure 1.1* shows the Gibbs free energy of phase α and β as a function of temperature. As long as the temperature of the system stays below the equilibrium temperature T_e, the free energy of α-phase has lower value and this phase is stable. At the temperature T_e the thermodynamic potentials G_α and G_β have the same value and both phases can coexist. When the temperature increases above T_e, the free energy of phase β becomes lower which leads to the phase transformation from α to β-phase.

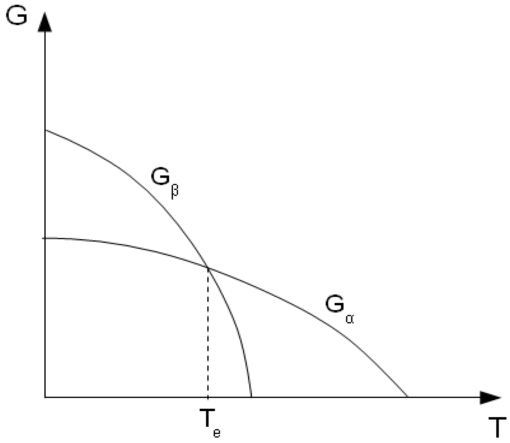

Figure 1.1. Gibbs free energy of phases α and β as a function of temperature.

The state of equilibrium of completely isolated system corresponds to the maximum of entropy, which implies the fact that all virtual variations of entropy are equal to zero ($\delta S = 0$). Let us write the entropy increment ΔS in the form of an expansion in the vicinity of equilibrium [7]:

$$\Delta S=\delta S+\frac{1}{2}\delta^2 S+\frac{1}{3!}\delta^3 S+\frac{1}{4!}\delta^4 S+\ldots \qquad (1.4)$$

where the terms $\delta^2 S$, $\delta^3 S$, $\delta^4 S$ ... are the second-, third-, and fourth-order differentials with respect to the state variables. The equilibrium is stable if all differentials are negative ($\delta^2 S$, $\delta^3 S$, $\delta^4 S$ ...< 0). Thus, the system tends to equilibrium after the perturbation has been applied. The equilibrium is metastable if the conditions $\delta S = 0$ and $\delta^2 S < 0$ are fulfilled but it may happen that third- or higher-order differentials are positive. It means that after having applied a small perturbation all parameters of the system return towards their original values, but after having applied a large perturbation they will rather tend to state transition. When for certain perturbations the condition $\delta^2 S > 0$ is satisfied, the equilibrium is unstable and even in the case of very small perturbations the system will move further and further away from the equilibrium.

The classification of phase transformations is historically based on the Ehrenfest proposal [8]. He proposed to group phase transitions according to the lowest discontinuous derivative of the free energy. The modern classification scheme divides the phase transitions into two broad categories:

- 1st order phase transition can be qualified as the one with discontinuous first derivative of the free energy. Good examples of the first-order phase transition are all gas-liquid-solid type transitions where discontinuous change in density (therefore also volume) can be easily observed:

$$\left(\frac{\partial G}{\partial p}\right)_T = V \tag{1.5}$$

As a consequence of the discontinuous change of entropy, the first-order phase transitions involve latent heat – a fixed amount of energy which is either absorbed or released in a system:

$$\left(\frac{\partial G}{\partial T}\right)_p = -S \tag{1.6}$$

In the first-order transitions two different phases can coexist with each other when system is approaching the unstable state, creating mixed-phase regimes in which some parts of the system have completed the transition and the others have not.

- 2nd order phase transition (also called continuous phase transition) is characterized by continuous first and discontinuous second derivative of the free energy:

$$\left(\frac{\partial^2 G}{\partial p^2}\right) = \left(\frac{\partial V}{\partial p}\right)_T = -\beta V \tag{1.7}$$

$$\left(\frac{\partial^2 G}{\partial T^2}\right) = -\left(\frac{\partial S}{\partial T}\right)_p = -\frac{c_p}{T} \tag{1.8}$$

$$\left(\frac{\partial^2 G}{\partial p \partial T}\right) = -\left(\frac{\partial V}{\partial T}\right)_p = \alpha V \tag{1.9}$$

where α and β denote the thermal expansion and the compressibility, respectively, and c_p is the heat capacity at constant pressure. The second-order phase transitions do not have the associated latent heat and the system passes continuously from one phase to another without the possibility of coexistence of phases. This type of phase transition has in general the character of the order-disorder transition. Typical examples of the second-order phase transitions are the ferromagnetic transitions, the transition from normal-conducting to superconducting state in some materials or the superfluid transition observed in liquid helium at cryogenic temperatures.

An excellent example of the second-order phase transformation is the so-called lambda transition in liquid helium. The transition takes place at the temperature $T_\lambda = 2.17$K (at atmospheric pressure) and transforms the normal helium (He I) into the superfluid helium (He II). Due to the fact that in the case of second-order phase transitions the coexistence of phases is not possible, there exists a distinct boundary between phases and the transition can be modelled as a moving front, called further the lambda front. The superfluid state of helium is characterised by very special properties: vanishing viscosity and excellent heat transport capabilities.

Heat transport in superfluid helium has quantum nature and its classical description is based on the mechanisms characteristic of Bose-Einstein condensates. However, it is not possible to use this description in the engineering calculations that are required in the design process of cryogenic systems. Thus, the two-fluid model proposed by Tisza is used [9], which assumes that superfluid helium is a mixture of the normal and the superfluid components and all properties of He II depend on the ratio between these two components, that changes as a function of temperature. This approach allows us to describe quantitatively the mass and heat transport in a narrow channel, filled initially with He I, by means of equations analogical to classical liquids [10], [11].

On the basis of Tisza theory, the Gorter-Mellink law is defined [12]. It describes heat transfer in superfluid helium and forms an analogy to the Fourier law:

$$\dot{q} = \left[f(T) \frac{dT}{dx} \right]^{\frac{1}{3}} \tag{1.10}$$

where *f(T)* represents the conductivity function.

In order to derive the temperature profile in He II the Gorter-Mellink law is integrated assuming that, for the sake of simplicity, the heat flux along the channel is constant:

$$x(T) = \frac{\int_{T_0}^{T} f(\eta)\, d\eta}{\dot{q}_{HeII}^{3}} \tag{1.11}$$

The temperature profile in He I is obtained by solving the problem of a solid (e.g. copper wire) in the liquid helium cylindrical enclosure. As an example, the heat transport in a concentric configuration of copper wire located in the middle of long, narrow channel filled with liquid helium is recalled [11]. The Fourier law written both for solid and for helium, with the assumption of perfect heat transport between solid and fluid in the radial direction, reads:

$$\left[(\rho c_p A)_{HeI} + (\rho c_p A)_{Cu} \right] \frac{\partial T}{\partial t} = \left[(k A)_{HeI} + (k A)_{Cu} \right] \frac{\partial^2 T}{\partial x^2} \tag{1.12}$$

As the specific heat of copper is small when compared to helium and the conductivity of liquid helium is insignificant when compared to copper, one can simplify *Eq. 1.12* to the following form:

$$\frac{\partial T}{\partial t} = D \frac{\partial^2 T}{\partial x^2} \tag{1.13}$$

where *D* denotes combined thermal diffusivity and is assumed to be constant here:

$$D = \frac{(kA)_{Cu}}{(\rho c_p A)_{HeI}} = const. \tag{1.14}$$

For a spacio - temporary problem the transformation of variables is usually applied. Assuming that the beginning of coordinate system moves together with the lambda front at the velocity *v*:

$$\xi = x - vt \tag{1.15}$$

The heat transport equation (*Eq. 1.13*) transforms to the following form:

$$\frac{\partial T}{\partial t}=D\frac{\partial^2 T}{\partial \xi^2}-v(t)\frac{\partial T}{\partial \xi} \tag{1.16}$$

The solution is obtained by applying the method of separation of variables. It is assumed that the general solution is expressed as a product of function of spatial variable ξ and a function of time t with additional constant value T_{end} which denotes the temperature at the end of the channel (cold reservoir):

$$T(\xi,t)=\Phi(t)\Psi(\xi)+T_{end} \tag{1.17}$$

Substituting the general solution (*Eq. 1.17*) to the heat transport equation (*Eq. 1.16*) one obtains:

$$\Psi\frac{\partial \Phi}{\partial t}=D\Phi\frac{\partial^2 \Psi}{\partial \xi^2}-v(t)\Phi\frac{\partial \Psi}{\partial \xi} \tag{1.18}$$

For the sake of simplicity, the assumption of constant velocity v of the lambda front is made. The final form of the heat diffusion equation can be written as follows:

$$\frac{1}{D\Phi}\frac{\partial \Phi}{\partial t}=\frac{1}{\Psi}\frac{\partial^2 \Psi}{\partial \xi^2}-\frac{v}{D\Psi}\frac{\partial \Psi}{\partial \xi} \tag{1.19}$$

Since the left hand side of *Eq. 1.19* is a function of t alone and the right hand side is function of ξ alone, the only possible solution implies that they are both equal to a separation constant k^2. Thus:

$$\frac{1}{D\Phi}\frac{\partial \Phi}{\partial t}=-k^2 \tag{1.20}$$

$$\frac{1}{\Psi}\frac{\partial^2 \Psi}{\partial \xi^2}-\frac{v}{D\Psi}\frac{\partial \Psi}{\partial \xi}=-k^2 \tag{1.21}$$

Eq. 1.20 can be simply solved by integrating both sides of the equation:

$$\int\frac{d\Phi}{\Phi}=\int -k^2 D\,dt \tag{1.22}$$

Then, the general solution of *Eq. 1.20* reads:

$$\Phi(t)=C_1 e^{(-k^2 D t)} \tag{1.23}$$

Eq. 1.21 represents a linear homogeneous second order differential equation:

$$\frac{\partial^2 \Psi}{\partial \xi^2}-\frac{v}{D}\frac{\partial \Psi}{\partial \xi}+k^2\Psi=0 \tag{1.24}$$

in which the general solution takes the form of exponential function:

$$\Psi=e^{\lambda\xi} \tag{1.25}$$

Substituting this general solution to the main equation one obtains:

$$e^{\lambda\xi}(\lambda^2+\frac{v}{D}\lambda+k^2)=0 \tag{1.26}$$

A non-trivial, real solution of the differential equation (*Eq. 1.24*) exists if the expression in brackets in *Eq. 1.26* has real roots, which implies that the following condition must be satisfied:

$$\Delta=\left(\frac{v}{D}\right)^2-4\mathrm{k}^2\geqslant 0 \tag{1.27}$$

Thus, the solution of *Eq. 1.24* takes the form:

$$\Psi(\xi)=C_2e^{\lambda_1\xi}+C_3e^{\lambda_2\xi} \tag{1.28}$$

where:

$$\begin{aligned}\lambda_1&=\frac{-v+\sqrt{v^2-4D^2k^2}}{2D}\\ \lambda_2&=\frac{-v-\sqrt{v^2-4D^2k^2}}{2D}\end{aligned} \tag{1.29}$$

The general solution of *Eq. 1.19* is derived as a product of *Eq. 1.23* and *Eq. 1.28*:

$$T(\xi,t)=e^{-k^2Dt}\cdot(Ae^{\lambda_1\xi}+Be^{\lambda_2\xi}) \tag{1.30}$$

where $A=C_1\cdot C_2$ and $B=C_1\cdot C_3$ are constants, calculated by applying suitable boundary conditions regarding the temperature value and the temperature gradient at the point of the phase transition:

$$\begin{aligned}T(\xi\to 0)&=T_\lambda\\ \frac{\partial T}{\partial\xi}(\xi\to 0)&=\frac{A_{HeII}}{A_{Cu}k_{Cu}}\dot{q}_\lambda\end{aligned} \tag{1.31}$$

Finally, the temperature profile in He I takes the form [11]:

$$T(\xi,t)=T_{end}+\frac{T_{end}-T_\lambda}{\lambda_1-\lambda_2}\left(\lambda_2e^{\lambda_1\xi}-\lambda_1e^{\lambda_2\xi}\right)+\frac{\tilde{D}\dot{q}_\lambda}{\lambda_1-\lambda_2}\left(e^{\lambda_1\xi}-e^{\lambda_2\xi}\right) \tag{1.32}$$

A complete temperature profile on either side of the phase transformation front is shown in *Fig. 1.2*. Motion of this front along the channel reflects the nature of the second-order phase transition – both phases can not coexist in thermodynamic equilibrium. The lambda front moves as long as the remnants of He I exist and disappears only when the total volume of He I has been replaced by He II.

On the other hand, any first-order phase transformation allows coexistence of both phases in thermodynamic equilibrium. Good example of such process consists in the transition from f.c.c. lattice to b.c.c. lattice and is called martensitic transformation.

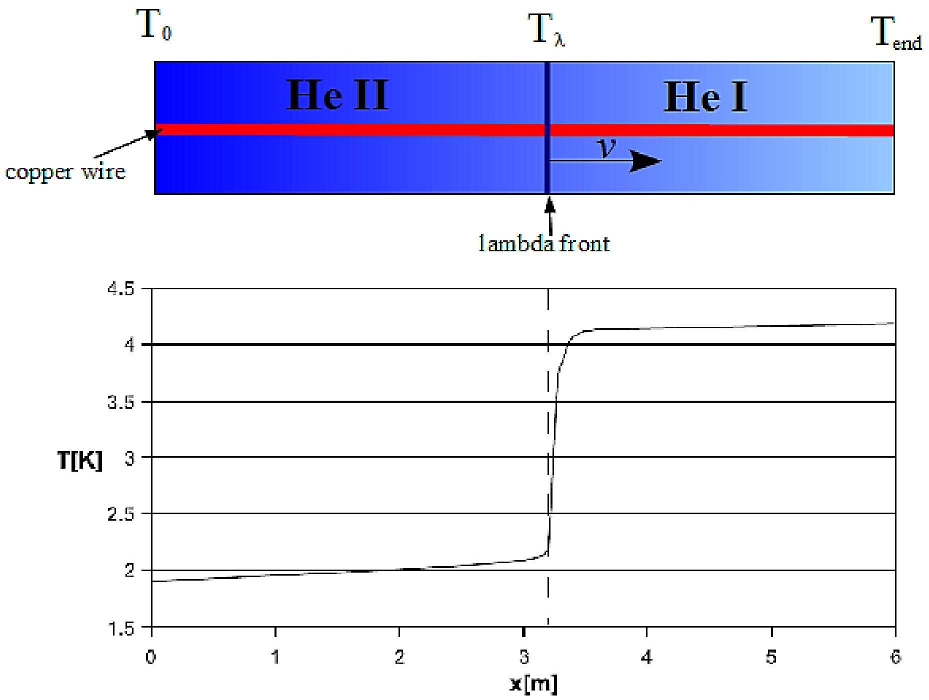

Figure 1.2: Illustration of the propagation of phase transformation front in liquid helium (2^{nd} order phase transition according to Ehrenfest).

1.3. Martensitic transformation

Diffusionless phase transformations in solids, also known as displacive transformations, consist in coordinated displacements of atoms at very small distances in such a way that they retain their original relationships with neighbouring atoms. This implies change of crystallographic configuration but without the diffusion mechanism. Relative displacements of atoms are usually smaller than interatomic distances. According to the classification of diffusionless transformations proposed by Cohen et al. [13], they can be divided into the transformations dominated by homogeneous lattice-distortive strains, known also as the Bain strains, and shuffles (*Fig. 1.3*).

Shuffle transformations change the symmetry or structure of the crystal by intercellular atom displacements, whereas the strain in the lattice is either negligible or not observed. Thus, the energy increase in the system is mainly due to interfacial energy, while the contribution of strain energy is rather small. Homogeneous lattice-distortive transformations consist in changes of the lattice shape and the strain energy term is significant here. They are subdivided into dilatation and deviatoric (shear) transformations, depending on the type of dominant deformation.

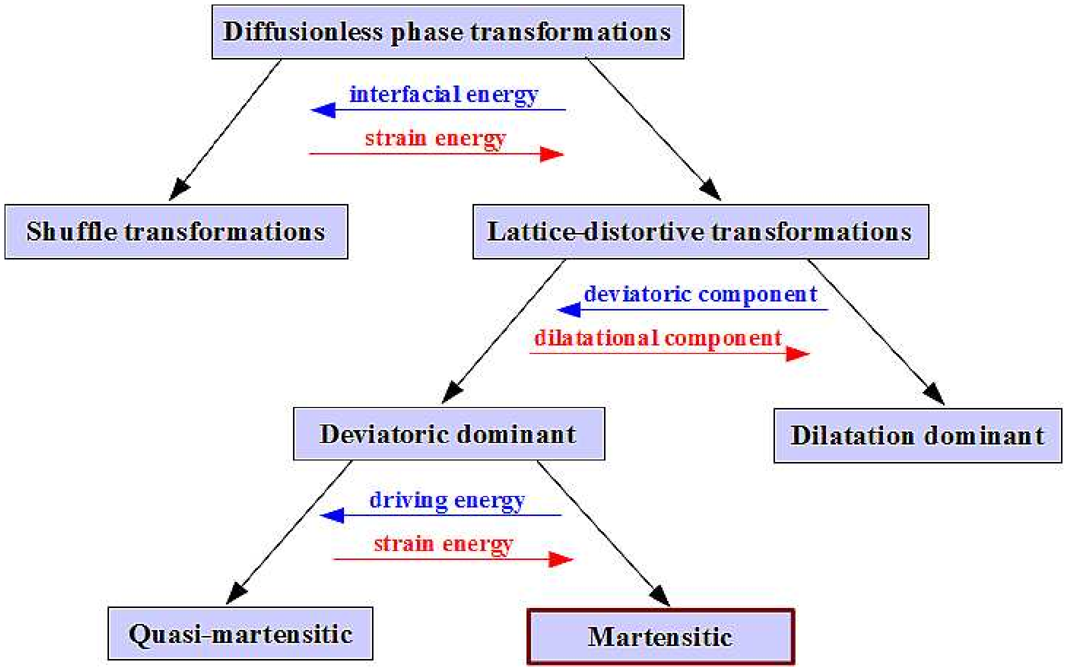

Figure 1.3: Classification of diffusionless transformations (Cohen et al. [13]).

An example of dilatation dominant transformation is the increase in size of cubic lattice along all three axes (*Fig. 1.4*). In this case, the sphere after the transformation remains the sphere, however it is not possible to find a vector with unchanged length. On the other hand, pure shear transforms the sphere into the ellipsoid but there is a set of vectors with unchanged lengths. This means that there is an invariant line which remains undistorted during the transformation. The necessary condition for deviatoric dominant transformation is the existence of such an invariant line.

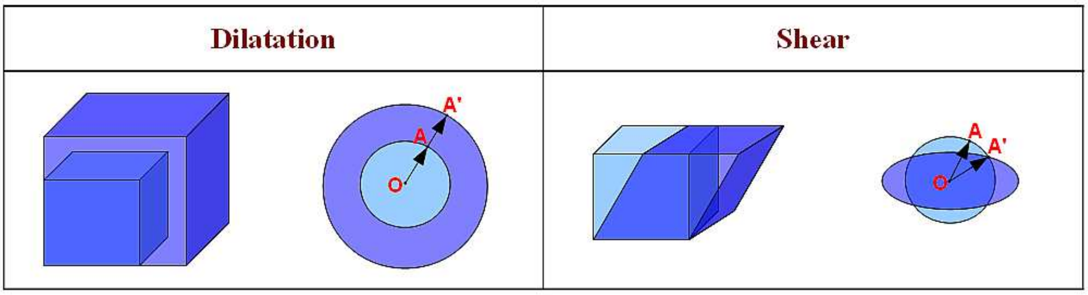

Figure 1.4: Mechanisms of dilatation and shear.

Comparing the magnitude of lattice-distortive displacements and vibrational displacements, one can distinguish between quasi-martensitic and martensitic transformations. Quasi-martensitic transformations are characterized by comparable lattice-distortive and vibrational displacements. In the case of martensitic transformations, the lattice-distortive displacements are large enough to dominate the kinetics and the morphology of transformation and high elastic strain energies are involved.

The martensitic transformation is thus the lattice-distortive transformation of deviatoric character, where displacements of atoms are much bigger when compared to lattice vibrations. It belongs to the group of the first order phase transformations in the solid state, which means that the parent and the product phases can coexist during the process. The diffusionless character of the transformation implies the possibility of transition even at very low temperatures and the growth of product phase is characterized by the speeds close to that of sound in metal (1100 m/s in steels). The transformation consists in the alteration of the distance between neighbouring atoms and it manifests itself as a change of crystallographic structure from face-centred-cubic γ parent phase to body-centred-cubic α' product phase.

The mechanism of $\gamma \rightarrow \alpha'$ transformation in terms of crystallography was first explained by Bain as a homogeneous deformation of the lattice. A unit cell of austenite can be described both as the face-centred-cubic cell with axes [a_1,a_2,a_3] (*Fig. 1.5 a*) as well as the body-centred-tetragonal cell with axes [b_1,b_2,b_3] (*Fig. 1.5 b*). By contraction of the parent lattice along b_3 axis and simultaneous expansions along b_1 and b_2 axes one gets the body-centred-cubic martensitic lattice (*Fig. 1.5 c*) and this type of deformation is called the Bain strain.

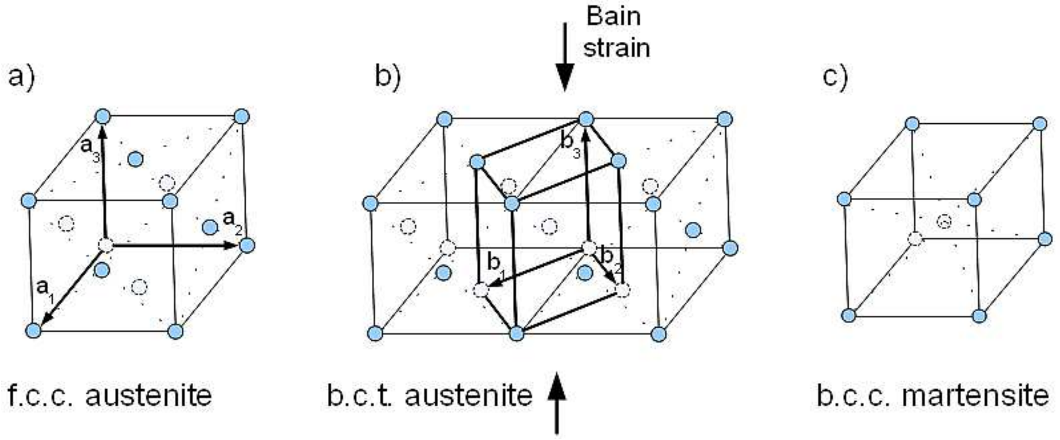

Figure 1.5: Martensitic transformation as a result of Bain strain.

Austenite can be geometrically represented as a sphere which, as a result of the Bain strain, is transformed into an ellipsoid (*Fig. 1.6 a, b*). After the transformation there are only two lines that are undistorted, however they are rotated with respect to their initial positions (*wx* to *w'x'* and *yz* to *y'z'* in *Fig. 1.6 b*). The necessary condition for the martensitic transformation is that at least one line stays invariant after the transformation, which is clearly not fulfilled in the case of applying only the Bain strain. However, if the Bain strain is combined with the rigid body rotation, it is possible to obtain an invariant line (*yz* is coincident with *y'z'* in *Fig. 1.6 c*). The above theory is consistent with experiments, that show the spatial orientation of crystals changed after the transformation.

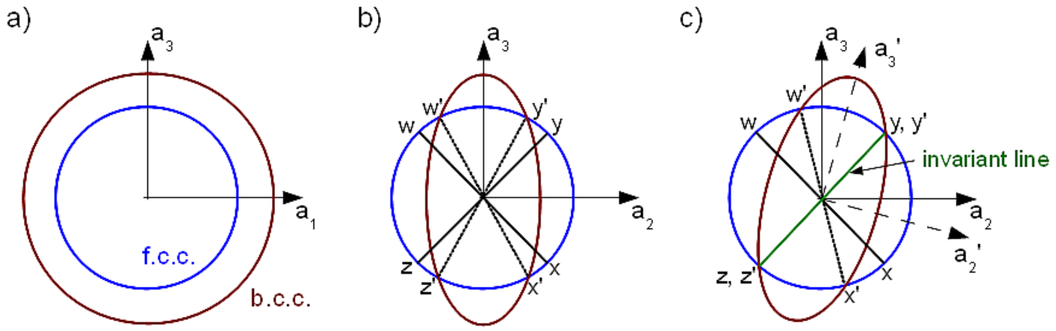

Figure 1.6: Geometric representation of f.c.c.-to-b.c.c. phase transformation.

Martensite, a product of the martensitic transformation, was first observed in quenched steels and as hard constituent had an important technological meaning. Nowadays, many others materials such as pure metals, metal alloys, ceramics, minerals, superconductors, solidified gases or polymers are known as structures which can undergo the martensitic transformation. Martensite is formed in the shape of plates or lenses. The interface between martensite and the surrounding parent phase is coherent. The chemical composition of martensite is identical to that of parent austenite but the properties differ.

In the case of spontaneous martensitic transformation, the driving force depends only on temperature. When the austenite is cooled, it begins to change into martensite. The temperature at which the transition starts is called the martensite start temperature M_s, whereas the temperature at which all austenite is transformed into martensite is called the martensite finish temperature M_f . The spontaneous transformation is reversible. When martensite is heated, austenite forms starting from the temperature A_s and the transformation finishes at the temperature A_f. Temperatures M_s and A_s as well as M_f and A_f usually do not correspond to each other resulting in transformation hysteresis loop (*Fig. 1.7*).

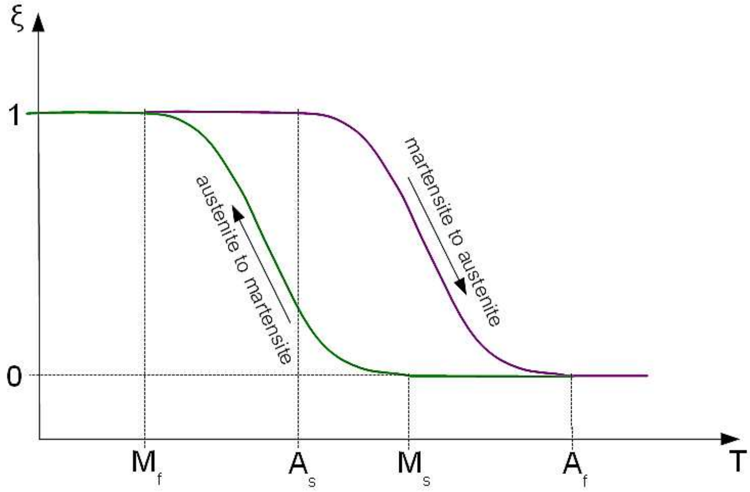

Figure 1.7: Hysteresis of martensitic transformation.

The applied stress or the plastic strain influence the free energy change, which acts as the driving force and can cause the phase transformation even above the martensite start temperature M_s. The deformation-induced martensitic transformation can be related to the TRIP (transformation-induced plasticity) effect resulting in the uniform, unrecoverable, macroscopic strain, which occurs in some high-strength metastable austenitic steels.

The conditions under which the mechanically-induced phase transformation takes place are shown in the form of temperature-stress diagram in *Fig. 1.8* [14]. Up to the temperature M_s^σ, the martensite nucleation can be induced solely by elastic stress and is known as the stress-assisted transformation. The mechanism of stress-assisted martensitic transformation was described in detail by e.g. Stupkiewicz and Patryk [15]. Plastic yielding below this temperature under applied stress is initiated by the martensitic transformation and the volume fraction of martensite depends linearly on the strain. Above the temperature M_s^σ the plastic flow occurs before martensite can be induced by stress and it precedes the nucleation of martensite. The relationship between the strain and the volume fraction of martensite becomes non-linear because the strain is related to both plastic deformation of austenite and transformation plasticity. The highest temperature at which martensite nucleation can be mechanically induced is called the M_d temperature [16].

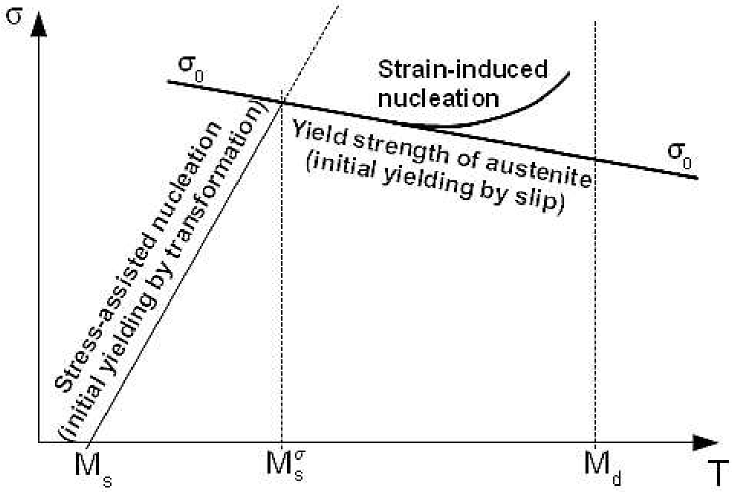

Figure 1.8: Stress-assisted and strain-induced regimes for mechanically- induced transformation.

1.4. Functionally graded materials

Since the beginning of human civilization people have been constantly trying to improve properties of materials in order to better adapt them to different needs. Alloy technology, which allows to obtain partial or complete solid solution of one or more elements in a a metallic matrix, has been developed for ages. Starting from bronzes – alloys consisting mostly of copper, through steels consisting primarily of iron, to nowadays sophisticated alloys with various composition carefully designed in scientific laboratories, different types of alloys have been developed in such a way that their properties could best suit to their application.

Composite materials are another example of engineered materials, known and improved since ancient civilizations. Composites consist of two or more materials which are referred as matrix and reinforcement depending on their role. The constituents have significantly different physical or chemical properties and remain separate and distinct on a macroscopic level within the finished structure. The matrix material surrounds and supports the reinforcement materials by maintaining their relative positions, whereas the reinforcements impart their special mechanical and physical properties to enhance the matrix properties.

The next step in material science was introduction of functionally graded material (FGM) concept in 1984 by Japanese scientists for a space plane project. The principle idea was to create a composite with heat-resistant ceramics on the high-temperature side and metals with high thermal conductivity on the low-temperature side with a gradual composition from one component to the other (*Fig. 1.9*) [17].

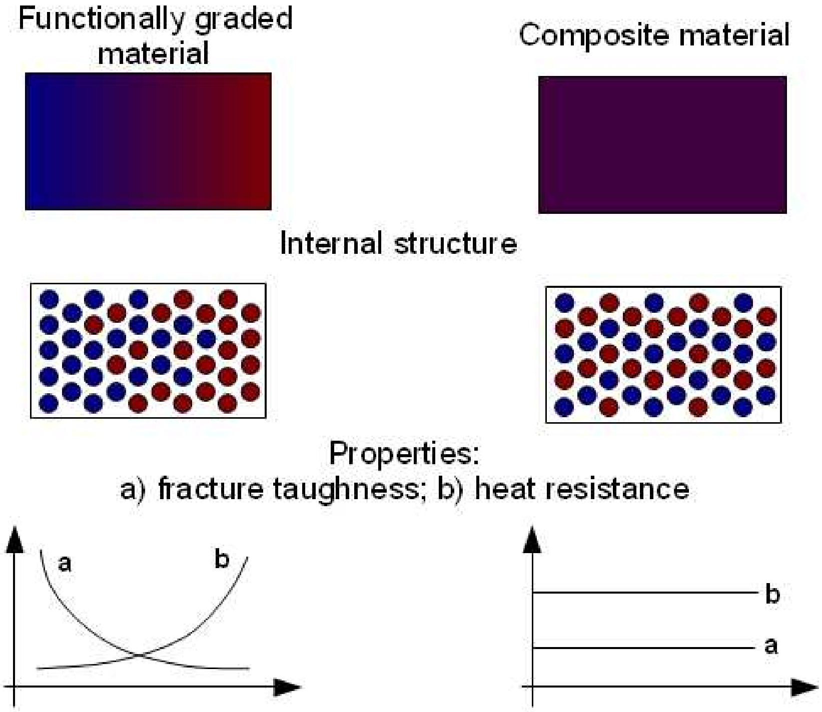

Figure 1.9: Concept of functionally graded materials

Currently, functionally graded materials belong to the family of modern engineering materials, that are characterized by gradually evolving micro-structure, composition, phase distribution, porosity, etc. They are designed to obtain optimal spatial variation of properties, adapted to the specific application. FGMs join advantages of composites and materials with surface layers as well as eliminate such problems like material discontinuity and associated high stresses and initiation of cracks and damage at the boundaries between two constituents or two layers.

There exists variety of fabrication methods of FGMs ranging from steel hardening to recently developed processes involving plasma or lasers. Among them the most known are: powder metallurgy (PM), physical vapour deposition (PVD), chemical vapour deposition (CVD), plasma spraying, self-propagating high-temperature synthesis (SHS), galvanoforming, eutectic reactions, diffusion. The majority of the presented fabrication methods are expensive and difficult in mass production. Thus, the use of functionally graded materials is still limited to structures where reliability rather than cost is the key issue. The processing of FGMs which is commonly available, relatively easy to realize, with good reproducibility is needed [18].

Research in this domain is continuously carried on because potential practical applications of functionally graded materials are significant. Due to combination of incompatible functions, FGMs are of special interest in the industry dealing with structures working at extreme conditions. For example thermal barriers capable of withstanding huge temperature gradients used in nuclear reactors, engine components, turbine blades, aircraft components, etc. are developed. Materials for industrial tools, requiring both wear resistance and toughness can be produced as FGMs. The biological and medical applications are also promising: biological compatibility, corrosion resistance and excellent hardness in artificial bones, joints and teeth can be achieved by using functionally graded materials. The concept of FGMs could be also successfully used in optics, optoelectronics, energy conversion systems, telecommunication and many other novel applications.

2. CONSTITUTIVE MODELLING OF STRAIN-INDUCED MARTENSITIC TRANSFORMATION

2.1. Literature review

- **Constitutive description of inhomogeneous elastic-plastic materials**

A theoretical basis of constitutive modelling of materials containing inclusions was developed by Eshelby [19], who presented the solution of the transformation and the inhomogeneity problems. The author investigated stress and strain fields related to ellipsoidal inclusions dispersed in infinite homogeneous isotropic elastic medium. The obtained results are of fundamental meaning for all theories regarding modelling of two-phase continuum.

Homogenization schemes and numerical algorithms for two-phase elastic-plastic materials were studied by Doghri and Ouaar [20]. The tangent operators: elastic-plastic (or ‘‘continuum’’) versus algorithmic (or ‘‘consistent’’) as well as anisotropic versus isotropic, were considered. The comparison of the stiffnesses of various tangent operators has been performed. Both Mori–Tanaka and double inclusion homogenization schemes were used together with two plasticity models: classical J_2 plasticity and Chaboche model with non-linear kinematic and isotropic hardening. The improved version of the formulation and tests with non-spherical inclusions were presented by Doghri and Friebel [21]. Mean-field homogenization of multiphase elastic-plastic materials reinforced with non-spherical and non-uniformly distributed inclusions was analysed further by Doghri and Tinel [22].

The effective mechanical response of elastic-plastic matrix reinforced with homogeneously distributed elastic ellipsoids was investigated by means of computational micromechanics and homogenization methods by Pierard et al. [23]. The authors performed both finite element simulation of the representative volume element of microstructure and non-linear composite by means of linearisation of the local behaviour through the use of the tangent or the secant stiffness tensors of the phases. The finite element results were used as benchmarks to estimate the accuracy of the prediction based on the homogenization methods for composites. The authors concluded that the best approximations of the effective properties with respect to the reference numerical results were provided by the incremental and the second-order secant methods, while the classical or first-order secant approach overestimated the composite flow stress.

- **Materials showing plastic strain-induced martensitic transformation**

The first attempt to explain transformation induced plasticity effect resulting from the phase transformation was made by Greenwood and Johnson [24]. The authors developed a phenomenological description of the stress-strain relation taking into account the applied stress, TRIP strain and the volume change during phase transformation.

The first description of kinetics of the plastic strain-induced martensitic transformation was introduced by Olson and Cohen [25]. They assumed that the strain-induced nucleation of martensitic embryos appears on the shear-band intersections and the increasing number of shear-band intersections depends on the plastic strain in the austenite. Volume fraction of martensite ξ was described as an exponential function in the following form:

$$\xi = 1 - \exp\{-\beta[1 - \exp(-\alpha\epsilon)]^n\} \tag{2.1}$$

The model consists of three parameters: α represents the rate of shear-band formation, β is proportional to the probability that the intersection will produce an embryo and n is a fixed exponent which allows to fit numerically the obtained curve to the experimental data. Comparison of analytically-derived sigmoidal curves and experimental results showed reasonably good agreement.

The constitutive modelling of steels undergoing the plastic strain-induced martensitic transformation started from the model of Narutani, Olson and Cohen [26], which aimed at estimating the plastic flow of steels including the phase transformation. The model comprised a static-hardening effect due to the presence of two phases in the material and the influence of dynamic softening caused by the martensitic transformation, which was treated as deformation mechanism. A strain-corrected rule of mixture was implemented in order to predict behaviour of two-phase material. Afterwards, Stringfellow, Parks and Olson [27] developed a more complex model for nonthermoelastic alloys which included the hardening effect of the martensite platelets as well as softening effect of the transformation itself, presented as the transformation strain. A self consistent method was used to describe the stress-strain relation. They also extended the Olson-Cohen model of transformation kinetics by indicating that under isothermal conditions, the volume fraction of martensite is not only the function of plastic strain but also the local stress state.

The model of Stringfellow et al. was generalised by Tomita and Iwamoto [28] in order to account for the experimentally observed temperature and strain rate sensitivities of the strain-induced martensitic transformation. It was noticed that the number of shear-band intersections increases together with the strain rate and this dependence was included into the relation describing phase transformation kinetics. The constitutive equations for the stress rate in two-phase composite material was established by introducing the plastic strain rate, composed of the sum of the plastic strain rate introduced by slip deformation and by the transformation. This model was later completed by Iwamoto, Tsuta and Tomita [29], who introduced deformation-mode-dependent transformation kinetics based on the traction and compression experimental results. The authors observed that the volume fraction of martensite for compression is higher than that for tension in the initial stage of the deformation, and then the relation is reversed in the high-strain region, what is also observed in the deformation mode dependence of the stress-strain relation.

Another constitutive model was proposed by Fischer et al. [30]. The authors developed a constitutive description of transformation-induced plasticity on the basis of the Gibbs free energy combined with the yield condition and the transformation condition. Applying this, they were able to obtain coupling of the plasticity and the phase transformation in the derived flow rule for the plastic strain rate and the transformation kinetics.

Micromechanical modelling of transformation induced plasticity in steels by means of local tangent approach was presented by Diani, Sabar and Berveiller [31]. The transformation kinetics was based on the local Bain strain rate of martensite variants and their volume fractions. The model involved complex coupling between plasticity caused by the thermomechanical loading and from the internal stresses due to the incompatible transformation strain. The model led to formulation of simple equations describing incompressible isotropic two-phase material.

The model predicting the amount of α' - martensite created during the strain-induced phase transformation under multiaxial thermomechemical loading of TRIP steels was presented by Diani and Parks [32]. They adapted the Olson-Cohen shear-band concept to a mesoscopic scale in order to define the kinetics of the deformation mechanism within the grain and build polycrystalline numerical model to simulate different strain states.

Levitas, Idesman and Olson [33] proposed a model based on the mesoscopic continuum thermodynamics theory and the solution of the corresponding boundary-value problem, which aimed at describing the experimental results related to the nucleation at the shear-bands intersections. The authors used multiplicative decomposition of the total deformation gradient into small elastic, finite plastic and transformation parts. The generalised Prandtl-Reuss equations were extended to the case of large strains and phase transformation. A revised theory of the martensitic transformation in elastic-plastic polycrystalline materials together with the orientation effect was developed by Fischer et al. [34].

Cherkaoui, Berveiller and Sabar [35] derived constitutive equations for an austenitic single crystal undergoing transformation induced plasticity, from which the overall behaviour of polycrystalline TRIP steels can be deduced using classical scale transition method. As a next step, the new approach to constitutive modelling was proposed by Cherkaoui, Berveiller and Lemoine [36]. Based on the micromechanical analysis of martensitic transformation, they considered formation of macrodomains with moving boundaries together with conditions for the nucleation and growth of martensitic platelets in he case of both homogeneous and heterogeneous plastic strain. It was assumed that the stress and the strain fields were continuous in each phase but undergo discontinuities across moving boundaries and Eshelby description of ellipsoidal inclusions was applied. The Helmholtz free energy was used as a potential in order to describe the thermodynamic state of two-phase material. Coupling between plasticity and martensitic phase transformation at the grain level was considered and the constitutive equations of an austenitic single crystal were derived, from which the overall behaviour of TRIP steels was deduced by using the self-consistent algorithm.

A new approach to kinetics of strain-induced martensitic transformation and constitutive equations of steels undergoing the phase transformation, which takes into account the dependence on the austenitic grain size, was proposed by Iwamoto and Tsuta [37]. The proposed constitutive equations were implemented in the finite element software and the deformation behaviour of a cylinder made of 304 austenitic stainless steel has been simulated under different environmental temperatures with various austenitic grain sizes. The dependence of the mechanical properties on the austenitic grain size was discussed.

Tomita and Iwamoto [38] proposed a constitutive model that includes the effect of temperature, strain rate and applied stress in modelling of strain-induced martensitic transformation. The authors implemented the set of constitutive equations of material undergoing martensitic transformation to finite element code which was used to simulate deformation behaviour including tension, compression and shear in 304 stainless steel under different environmental temperatures (from 77 to 353 K). Computation of the cyclic deformation response of steel bars with ringed notches was additionally performed.

Another numerical microstructure-based model describing the strain-induced martensitic transformation in metastable austenitic steel was presented by Han et al. [39]. The computational model was based on the assumption that the martensitic transformation kinetics was modelled as a nucleation-controlled phenomenon by a function of the interaction energy between externally applied stress state and lattice deformation and the increase of nucleation site in the austenite due to the plastic deformation was represented by the increase of the shear-band intersection. A self-consistent model was implemented in iterative program based on the radial return method to predict the deformation behaviour under various loads. The results obtained were compared with the experimental data of the uniaxial tension and simple shear.

Dan et al. [40] developed a constitutive model of the transformation-induced plasticity accompanying the strain-induced martensitic transformation in TRIP steels. Nucleation sites in the austenite due to the plastic deformation were modelled as the increase of the shear band intersection and the probability of nucleation was derived taking into account stress state, plastic strain and strain rate, which influence the temperature increment. Anisotropic yield function was used and a mixed hardening law with four phases was developed instead of the mixed hardening law with two phases. The constitutive model was implemented in the finite element software and the comparison between the experimental data and the simulations was carried out. Involving the effect of temperature increase allowed to obtain better results in the case of modelling the transformation-induced plasticity than by using the models with constant temperature.

Fatigue behaviour of austenitic stainless steels in view of plastic strain-induced martensitic transformation was first investigated by Baudry and Pineau [41]. The authors identified the volume fraction of martensite by using magnetic measurements and X-ray techniques. They introduced the concept of critical plastic strain amplitude, below which the material does not undergo the phase transformation. Properties of 316L and 316LN austenitic stainless steels during cyclic loading at 300 K and 77 K were investigated by Vogt et al. [42]. The authors pointed out the enhancing role of nitrogen content in the fatigue resistance. At room temperature slight hardening followed by softening is observed in both steels. At 77 K behaviour of both materials is characterised by hardening and quasi-saturation for smaller strain amplitudes but in the case of higher strain amplitudes 316L shows significant hardening whereas in 316LN the initial hardening is present followed by softening and again hardening. The difference in low-cycle fatigue behaviour at cryogenic temperatures results from the $\gamma \rightarrow \alpha'$ transformation and different volume fractions of martensite in both steels. Botshekan et al. [43], [44] performed monotonic and cyclic tests of 316LN stainless steel at 300 K and 77 K, taking into account the influence of the martensitic transformation under high plastic straining on the stress-strain relationship and the fatigue life. The α' – martensite volume fraction was measured during tests. No martensite was detected at room temperatures but at cryogenic temperatures partial martensitic transformation was observed when cyclic loading of high strain amplitude was applied. A characteristic feature of the material at cryogenic temperatures is higher tensile elongation in the monotonic test and secondary hardening in the fatigue test. These effects were explained in terms of martensite presence, which makes crack nucleation and growth more difficult. Suzuki et al. [45] investigated the fatigue properties of 304L and 316L stainless steels at cryogenic (4 K and 77 K) and room temperatures with special focus on the mechanical strength and the magnetic properties. They conducted both tensile and fatigue tests and for both types of test the magnetic permeability of the steels was measured. The authors aimed at investigating the critical strain above which the plastic strain-induced phase transformation starts. The stress and the strain limitations were considered in view of design of superconducting magnets, where increasing permeability of material due to the phase transformation is undesirable.

The linearised law describing kinetics of the $\gamma \rightarrow \alpha'$ phase transformation in metastable austenitic stainless steels, adapted especially to low temperature applications, was presented by Garion and Skoczeń [46]. Next, Garion, Skoczeń and Sgobba [47] developed a constitutive model of the plastic strain-induced martensitic transformation on the basis of the linearised kinetics law, mixed hardening rule and Mori-Tanaka homogenisation. They also carried out experiments on 316L stainless steel at room and at cryogenic temperatures in order to identify the necessary parameters. Based on this, the method of creation of functionally graded structural members by straining them at low temperatures and initiating the phase transformation was proposed by Skoczeń [48], presenting as an example torsion of circular rods. This idea was further developed by Sitko, Skoczeń and Wróblewski [49], who proposed bending of rectangular beams as a method of obtaining structures with spatial variation of properties.

The two-phase model of plastic hardening of materials undergoing the strain-induced phase transformation was presented by Mróz and Ziętek [50]. The authors formulated constitutive equations introducing the yield surface, the limit back stress surface and the transformation surface. It was assumed that the back stress is affected by the volume fraction of martensite. The numerical simulations of uniaxial cyclic loads were carried out and showed good agreement with experimental data.

Lee et al. [51] carried out uniaxial tension tests of 304 and 316 steels at cryogenic temperatures. The authors proposed a new constitutive description of austenitic stainless steels based on the modified Bodner plasticity model that includes three kinds of nonlinearities: discontinuities at yielding, phase transformation and damage. Results of the tests were used to investigate inelastic behaviour of the materials and identify proper parameters of the constitutive model. Finite element model was built and numerical results were cross-checked with the experimental data.

Lee, Kim and Han [52] formulated a crystal plasticity model incorporating the mechanically induced martensitic transformation in metastable austenitic steel. The kinetics of martensite transformation was based on the consideration of nucleation-controlled phenomenon and nucleation probability was a function of the interaction energy between externally applied stress and lattice deformation. The finite element analyses were carried out considering the effect of volume change by the Bain deformation and the lattice-invariant shear during the martensitic transformation by modifying effectively the evolution of plastic deformation gradient in the conventional rate-dependent crystal plasticity. Comparison between the finite element results and the experimental data under simple loading conditions was carried out in order to validate the model and good agreement with the measurements for the stress–strain response, transformed martensitic volume fractions and the influence of strain rate on the deformation was obtained.

The literature review shows that many attempts have been made to correctly describe the strain-induced martensitic transformation and related TRIP effects. Both the kinetics of the transformation and the constitutive equations describing material behaviour are constantly developed by using different formulations (thermodynamic potentials, micromechanical approach, effective properties, etc.). The application of numerical methods, especially finite element method, offers the opportunity to implement even more complex constitutive models, simulate the mechanical behaviour of materials and cross-check the results with the experimental data in order to validate the models. Application of the constitutive modelling to design of functionally graded materials obtained via the plastic strain-induced martensitic transformation is a novel idea which will be developed in the present Thesis.

2.2. Aim and scope of the Thesis

The main objective of the Thesis consists in further development of methods of creating functionally graded materials by the strain-induced martensitic transformation at cryogenic temperatures. Appropriate straining of structural members at low temperatures leads to creation of materials with spatial variation of properties thanks to the phase transformation. The gradient of material properties results from the amount of martensitic inclusions created in the austenite matrix. Mechanical properties of martensite in steels differ from the properties of austenite: the austenite already flows plastically when undergoing the phase transformation whereas the new-created martensitic platelets are still in the elastic state. This two-phase structure containing hard martensitic inclusions dispersed in a soft austenitic matrix improves the effective properties of material. What is more important, the inclusions form obstacles for motion of dislocations, what affects the strengthening of steel.

One can design the properties of structural member by programming proper loading conditions and by considering the internal forces distribution and the corresponding stress and strain fields. For example, a component with radially varying mechanical properties can be obtained by applying torque at cryogenic temperatures to a stainless steel rod of circular cross-section. As a results, one creates a structure where the elastic-plastic austenitic core is surrounded by the hardened, two-phase layer consisting of austenitic matrix with martensitic inclusions. Similarly, bending of a beam at cryogenic temperatures leads to creation of structural member of gradually varying mechanical properties with respect to the neutral axis, where external layers of the beam have two-phase structure.

In the Thesis, the fully analytical models corresponding to 1D cases are presented, based on extended version of the constitutive model of two-phase continuum with evolution of proportion between the phases, developed by Garion, Skoczeń and Sgobba [47], and kinetics of the $\gamma \rightarrow \alpha'$ phase transformation proposed by Garion and Skoczeń [46]. In particular, the following cases are elaborated:

- tension/compression of rods in order to evaluate parameters of the constitutive model and correlate the model with experimental results,
- torsion of circular rods aimed at obtaining radially evolving mechanical properties,
- bending of prismatic beams aimed at obtaining layered structures with evolving mechanical properties,
- cyclic and combined loadings applied to structural members in order to investigate the influence of the $\gamma \rightarrow \alpha'$ phase transformation on adaptation and inadaptation mechanisms.

The analytical models are cross-checked with the numerical model implemented in the finite element software (ANSYS). The numerical tests are carried out in order to compare the results obtained by both analytical and numerical calculations. Next, the numerical simulations of more complex structures are shown, such as analysis of the thin-walled shells (bellows expansion joints) working at cryogenic temperatures.

2.3. Kinetics of the strain-induced $\gamma \rightarrow \alpha'$ phase transformation

In consequence of the strain-induced phase transformation of TRIP steels, martensite platelets dispersed in the austenitic matrix are formed. It has been observed that the martensite embryos are created on the intersection of shear-bands. In a natural way, the volume fraction of martensite ξ depends on the temperature due to the relation with chemical energy. However, in the case of strain-induced transformation, also the plastic deformation as well as the stress field influence the transformation driving force and regulate the amount of new-created martensite.

Transformation curves, illustrating the volume fraction of martensite as a function of temperature, are usually sigmoidally shaped. For transformations proceeding at the temperatures close to room temperature, they have rather flat characteristics and slowly reach the saturation level (*Fig. 2.1 a*). At cryogenic temperatures the thermodynamic driving force at the transformation is higher and therefore the phase transformation process has more dynamic course. The whole process can be divided into three stages (*Fig. 2.1 b*):

- Phase I: very low rate of phase transformation combined with nucleation of martensite embryos
- Phase II: reaching the threshold value of plastic strain ε_ξ^p, followed by rapid growth of α'-phase content with a constant transformation rate
- Phase III: reaching the second threshold strain value ε_L^p, where the phase transformation slows down and the volume fraction of martensite approaches asymptotically the saturation level ξ_L.

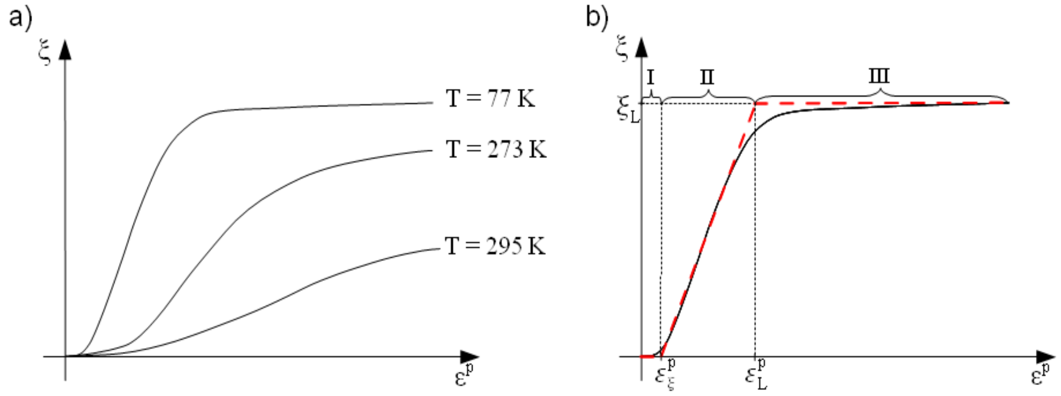

Figure 2.1: Volume fraction of martensite as a function of plastic strain: temperature dependence (a) and linearised model (b).

This three-stage description of phase transformation kinetics, characteristic of cryogenic temperatures, can be approximated by the linearised law proposed by Garion and Skoczeń [46], where only phase II is taken into account as an active process. The rate of volume fraction of martensite is expressed as:

$$\dot{\xi}=A(T,\dot{\underline{\underline{\epsilon}}}^p,\dot{\underline{\underline{\sigma}}})\,\dot{p}\,H(\epsilon^p-\epsilon^p_\xi,\xi_L-\xi) \tag{2.2}$$

where A is a parameter determining the slope of the curve in phase II of the process, $\dot{p}$ is the accumulated plastic strain rate and H is the double-argument Heavyside step function.

2.4. Constitutive model of material with γ→α' phase transformation

Formulation of the constitutive model of a material subjected to the plastic strain induced phase transformation is based on multiscale considerations. On the one hand, it takes into account micromechanical phenomena such as interactions of dislocations with martensitic inclusions or influence of hard inclusions on a soft matrix (the Eshelby approach [19] used in the homogenisation). On the other hand, the model is defined on the mesoscopic level by means of a representative volume element (RVE), where all material properties are treated as uniform and their equivalent values are obtained via homogenisation process. Size of the RVE should be large in comparison with the microstructure, containing sufficient amount of inhomogeneities, but small enough to justify using the local approach (*Fig. 2.2*). Consequently, the RVE is considered as such a portion of material over which the stresses and the strains are assumed uniform, therefore the mechanical behaviour of material can be described in terms of continuum mechanics.

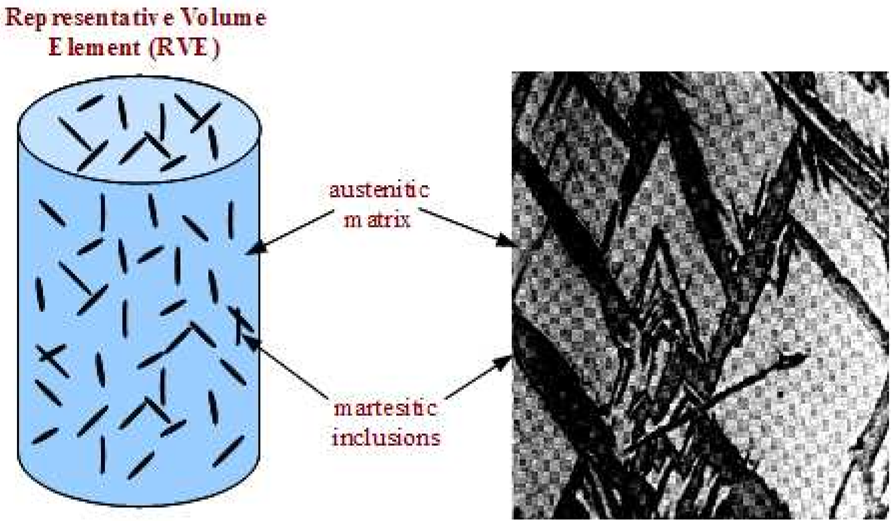

Figure 2.2: Representative Volume Element.

The general constitutive law of material subjected to the plastic strain field $\underline{\epsilon}^{p}$, the thermal strain field $\underline{\epsilon}^{th}$ and the Bain strain $\underline{\epsilon}^{bs}$, assuming that all strains can be considered small, is given in the following form:

$$\underline{\sigma} = \underline{\underline{\underline{\underline{E}}}} : (\underline{\epsilon} - \underline{\epsilon}^{p} - \underline{\epsilon}^{th} - \xi \underline{\epsilon}^{bs}) \tag{2.3}$$

The Bain strain $\underline{\epsilon}^{bs}$ represents here the relative volume change Δv due to the phase transformation:

$$\underline{\underline{\epsilon}}^{bs}=\frac{1}{3}\Delta v\,\underline{\underline{I}};\quad \Delta v=\frac{V_m-V_a}{V_a} \tag{2.4}$$

where V_m and V_a are the volumes of martensite and austenite, respectively, and $\underline{\underline{I}}$ is the second rank identity tensor.

The stiffness tensor $\underline{\underline{\underline{\underline{E}}}}$ can be expressed as a sum of the spherical operator $\underline{\underline{\underline{\underline{J}}}}$, representing the hydrostatic part of elastic energy and the deviatoric operator $\underline{\underline{\underline{\underline{K}}}}$, that represents the shear state:

$$\underline{\underline{\underline{\underline{E}}}}=3\mathrm{k}\,\underline{\underline{\underline{\underline{J}}}}+2\mu\,\underline{\underline{\underline{\underline{K}}}} \tag{2.5}$$

where:

$$\underline{\underline{\underline{\underline{J}}}}=\frac{1}{3}\underline{\underline{I}}\otimes\underline{\underline{I}}\,;\quad \underline{\underline{\underline{\underline{K}}}}=\underline{\underline{\underline{\underline{I}}}}-\underline{\underline{\underline{\underline{J}}}} \tag{2.6}$$

and $\underline{\underline{\underline{\underline{I}}}}$ is the fourth rank identity tensor, whereas μ and k are the elastic shear and bulk moduli, respectively. The moduli are expressed below by using Young's modulus E and Poisson's ratio ν, in the following way:

$$\mu=\frac{E}{2(1+\nu)}\,;\quad k=\frac{E}{3(1-2\nu)} \tag{2.7}$$

The yield surface f is defined by means of the second invariant J_2 of the stress tensor:

$$f(\underline{\underline{\sigma}},\underline{\underline{X}},R)=J_2(\underline{\underline{\sigma}}-\underline{\underline{X}})-\sigma_0-R \tag{2.8}$$

$$J_2(\underline{\underline{\sigma}}-\underline{\underline{X}})=\sqrt{\frac{3}{2}(\underline{\underline{s}}-\underline{\underline{X}}):(\underline{\underline{s}}-\underline{\underline{X}})} \tag{2.9}$$

where $\underline{\underline{X}}$ stands for the back stress, R is the isotropic hardening parameter, $\underline{\underline{s}}$ is the deviatoric stress and σ_0 denotes the yield stress.

It is assumed that the plastic strain increment defined for a material that undergoes phase transformation can be described by means of the associated flow rule, where the yield surface f is understood as the plastic potential:

$$d\epsilon^p=\frac{\partial f}{\partial\underline{\underline{\sigma}}}d\lambda \tag{2.10}$$

Here, λ is the Lagrange multiplier and can be calculated by using the consistency condition:

$$\dot{f}(\underline{\underline{\sigma}},\underline{\underline{X}},R)=0 \tag{2.11}$$

The model of plastic hardening consists of the kinematic hardening component, represented by the position of the centre of yield surface in the form of 2nd rank tensor $\underline{\underline{X}}$, and the isotropic hardening component, described by a scalar parameter R. The phase transformation influences significantly both hardening parameters:

$$d\underline{\underline{X}} = d\underline{\underline{X}}_a + d\underline{\underline{X}}_{a+m} = \frac{2}{3} C_X(\xi)\, d\underline{\underline{\epsilon}}^p \tag{2.12}$$

$$dR = C_R(\xi)\, dp \tag{2.13}$$

where C_X and C_R are the kinematic and the isotropic hardening moduli, respectively. Both of them are functions of the volume fraction of martensite and the total kinematic hardening is represented as a sum of the back stress $\underline{\underline{X}}_a$, corresponding to the motion of dislocations in the austenite, and the back stress $\underline{\underline{X}}_{a+m}$ resulting from the homogenised two-phase material (austenite and martensite).

In the case of plastic behaviour of pure austenite, the linear kinematic hardening law can be used:

$$d\underline{\underline{X}}_{a0} = \frac{2}{3} C_0\, d\underline{\underline{\epsilon}}^p \tag{2.14}$$

where C_0 is the linear hardening modulus. However, in the presence of evolving martensitic inclusions the hardening law can not be considered linear. Interactions between dislocations and martensitic platelets cause additional hardening of the material due to the fact that inclusions act as barriers for moving dislocations and the whole process becomes nonlinear. The hardening modulus C_0 is thus replaced by the modulus $C(\xi)$ that depends on the martensite content and can be expressed as:

$$C(\xi) = C_0\, \phi(\xi) \quad \text{for} \quad 0 \leqslant \xi \leqslant \xi_L \quad \text{and} \quad \phi(0) = 1 \tag{2.15}$$

2.4.1. Micromechanics

When crossing an inclusion of the average size *d*, much smaller than the average distance between inclusions (*d << l*), a dislocation has to develop the shear stress τ_p required for the passage and leaves behind a closed loop around each inclusion (Orowan mechanism, *Fig. 2.3*).

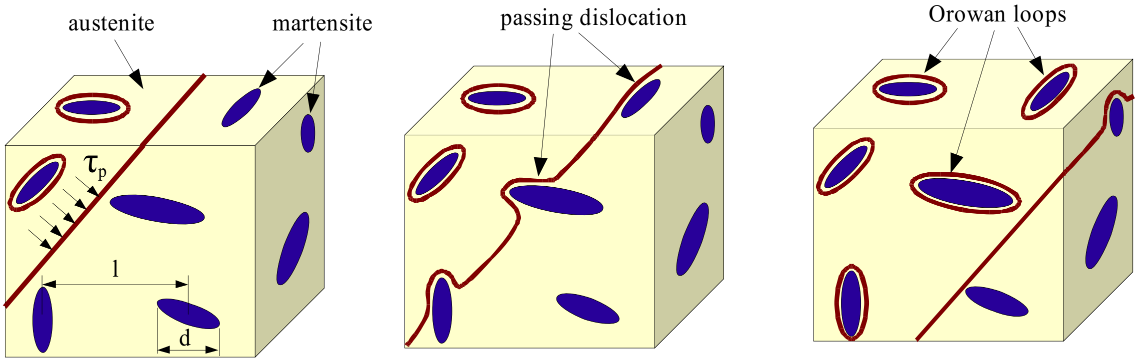

Figure 2.3: RVE with passing dislocation and the mechanism of Orowan loops.

On the basis of the micromechanial analysis, the general formula for the shear stress τ_p is given as a relation between the shear modulus μ, the length of the Burgers vector b and the mean distance between inclusions l:

$$\tau_p = \mu \frac{b}{l} \tag{2.16}$$

Assuming that the inclusions are distributed uniformly in the material, the total volume of the considered RVE is expressed as product of the volume of elementary cell (*Fig. 2.4*) and the number n^3 of inclusions in the RVE:

$$V = n^3 (l+d)^3 \tag{2.17}$$

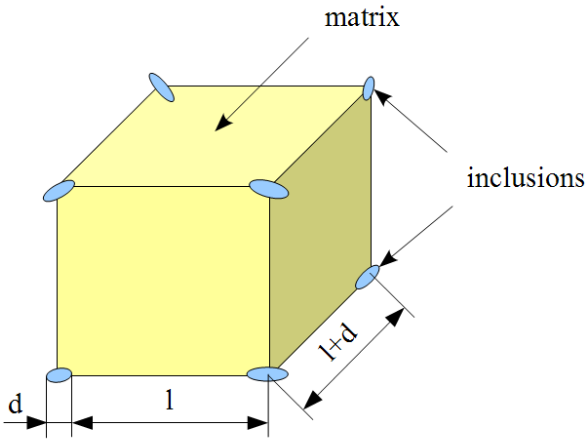

Figure 2.4: Unit cell containing inclusions.

Since the size of inclusions is small when compared to the distance between them, *Eq. 2.17* can be simplified:

$$V = n^3 l^3 \tag{2.18}$$

The total volume that is occupied by martensitic inclusions is calculated as the volume of single inclusion V_i multiplied by the number of inclusions n^3. For the sake of simplicity, it is assumed that the inclusions have spherical shape:

$$V_\xi = n^3 V_i = n^3 \frac{\pi d^3}{6} \tag{2.19}$$

Thus, the volume fraction of martensite reads:

$$\xi = \frac{V_\xi}{V} = \frac{\pi}{6} \left(\frac{d}{l} \right)^3 \tag{2.20}$$

The above equation defines the distance between the martensitic inclusions as a function of the size of inclusions and the volume fraction of martensite:

$$\frac{1}{l} = \frac{1}{d} \sqrt[3]{\frac{6\xi}{\pi}} \tag{2.21}$$

Substituting this relation to *Eq. 2.16*, one obtains the shear stress τ_p needed for a dislocation to pass across the inclusion, as a function of the volume fraction of martensite:

$$\tau_p = \frac{\mu b}{d}\sqrt[3]{\frac{6\xi}{\pi}} \tag{2.22}$$

The volume fraction of martensite can be expressed as a sum of the initial volume fraction of inclusions ξ_0 and the increment of inclusions caused by the phase transformation $\Delta\xi$:

$$\xi = \xi_0 + \Delta\xi \tag{2.23}$$

In view of *Eq. 2.23*, the shear stress is equal to:

$$\tau_p = \frac{\mu b}{d}\sqrt[3]{\frac{6}{\pi}\xi_0}\left(1+\frac{\Delta\xi}{\xi_0}\right)^{\frac{1}{3}} \tag{2.24}$$

By expanding the expression in brackets into the Tylor series, one arrives at:

$$\left(1+\frac{\Delta\xi}{\xi_0}\right)^{\frac{1}{3}} \approx 1+\frac{1}{3}\frac{\Delta\xi}{\xi_0}+\ldots \tag{2.25}$$

Neglecting the higher order terms of the series, the final expression for the shear stress in the case of two-phase material becomes approximately linear as a function of the volume fraction of martensite [48] and is equal to:

$$\tau_p = \frac{\mu b}{d}\left(\frac{6\xi_0}{\pi}\right)^{1/3}\left(1+\frac{\xi-\xi_0}{3\xi_0}\right) \tag{2.26}$$

In consequence, the function φ(ξ), that relates the linear hardening modulus to the hardening modulus resulting from the Orowan mechanism, can be expressed in the linear form:

$$\phi(\xi) = 1 + h\xi \tag{2.27}$$

where *h* is a material dependent parameter.

The back stress increment can be thus decomposed into the term responsible for the hardening of pure austenite ($d\underline{\underline{X}}_{a0}$) and the term corresponding to additional hardening due to the presence of martensitic inclusions ($d\underline{\underline{X}}_{a\xi}$):

$$d\underline{\underline{X}}_a = d\underline{\underline{X}}_{a0} + d\underline{\underline{X}}_{a\xi} = \frac{2}{3}C_0\phi(\xi)\,d\underline{\underline{\epsilon}}^p = \frac{2}{3}C_0\,d\underline{\underline{\epsilon}}^p + \frac{2}{3}C_0 h\xi\,d\underline{\underline{\epsilon}}^p \tag{2.28}$$

2.4.2. Tangent stiffness of martensite and austenite

The constitutive relation between the stress and the strain fields in martensite is obtained under the assumption that martensite remains elastic while the material is being loaded and can be expressed as:

$$\Delta \underline{\underline{\sigma}}_m = \underline{\underline{\underline{\underline{E}}}}_m : \Delta \underline{\underline{\epsilon}} \tag{2.29}$$

The stiffness modulus $\underline{\underline{\underline{\underline{E}}}}_m$ does not change during the loading process and is reflected by:

$$\underline{\underline{\underline{\underline{E}}}}_m = 3\mathrm{k}_m \underline{\underline{\underline{\underline{J}}}} + 2\mu_m \underline{\underline{\underline{\underline{K}}}} \tag{2.30}$$

$$\mu_m = \frac{E}{2(1+\nu_m)}\ ;\quad k_m = \frac{E}{3(1-2\nu_m)} \tag{2.31}$$

where k_m and μ_m are the bulk and the shear moduli of martensite (in the elastic state), respectively, and ν_m is the Poisson's ratio of martensite.

For the austenite, that flows already plastically in the course of the phase transformation the approach proposed by Hill [53] is applied. It consists in linearisation of the elastic-plastic constitutive equations and definition of suitable local tangent stiffness operator. The stress increment can be obtained by imposing the tangent stiffness modulus $\underline{\underline{\underline{\underline{E}}}}_{ta}$ on the strain increment and performing contraction:

$$\Delta \underline{\underline{\sigma}}_a = \underline{\underline{\underline{\underline{E}}}}_{ta} : \Delta \underline{\underline{\epsilon}} \tag{2.32}$$

The basic concept of linearisation in the constitutive modelling of elastic-plastic continuum and extraction of tangent stiffness operator is shown in *Fig. 2.5*.

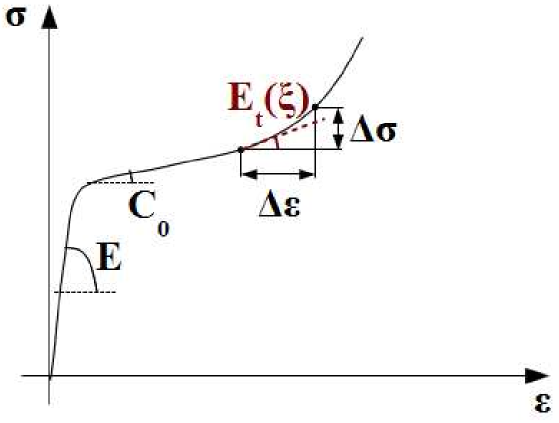

Figure 2.5: Basic idea of the incremental solution by means of tangent operator.

In its general form, the elastic-plastic tangent stiffness tensor $\underline{\underline{\underline{\underline{E}}}}_{ta}$ becomes an anisotropic operator expressed by means of tangent bulk modulus k_{ta} and tangent shear μ_{ta} modulus:

$$\underline{\underline{\underline{\underline{E}}}}_{ta}=3\mathrm{k}_{ta}\underline{\underline{\underline{\underline{J}}}}+2\,\mu_{ta}\left(\underline{\underline{\underline{\underline{K}}}}-\frac{\underline{\underline{n}}\otimes\underline{\underline{n}}}{1+\dfrac{C}{3\,\mu}}\right) \tag{2.33}$$

where $\underline{\underline{n}}$ denotes unit vector normal to the yield surface:

$$\underline{\underline{n}}=\sqrt{\frac{3}{2}}\,\frac{\underline{\underline{s}}-\underline{\underline{X}}}{J_2(\underline{\underline{s}}-\underline{\underline{X}})} \tag{2.34}$$

However, in many cases it is more convenient to apply the elastic-plastic tangent stiffness operator reduced to isotropic form without loosing the precision of computations. The operation of “stripping down” the tangent stiffness operator is performed by projection of the complete anisotropic operator into the space of isotropic operators. It is worth pointing out, that from the numerical point of view it is beneficial for the correct convergence of the solution process.

As a result of the projection to the space of isotropic operators good predictions of the effective properties are obtained. This formulation was studied in detail by Doghri and Ouaar [20] as well as Doghri and Friebel [21]. The isotropic form of the elastic-plastic operator is built in the form similar to the elastic stiffness tensor, which leads to the following expression:

$$\underline{\underline{\underline{\underline{E}}}}_{ta}=3\mathrm{k}_{ta}\underline{\underline{\underline{\underline{J}}}}+2\,\mu_{ta}\underline{\underline{\underline{\underline{K}}}} \tag{2.35}$$

where:

$$\mu_{ta}=\frac{E_t(\xi)}{2(1+\nu_a)}\ ;\ \ k_{ta}=\frac{E_t(\xi)}{3(1-2\,\nu_a)}\ ;\ \ E_t(\xi)=\frac{EC(\xi)}{E+C(\xi)} \tag{2.36}$$

It is worth pointing out, that here an original formulation involving tangent stiffness modulus E_t has been used. This modulus can be easily extracted – for comparison – from a uniform stress-strain curve obtained by means of unidirectional tension/compression test performed at cryogenic temperatures.

In the case of γ→α' phase transformation, the tangent modulus E_t is a function of the volume fraction of martensite ξ and evolves continuously during the phase transformation process, influencing both the bulk and the shear modulus. By substituting tangent modulus into the formulae for shear and bulk modulus one obtains:

$$\begin{aligned}\mu_{ta}&=\frac{E}{2(1+\nu_a)}\,\frac{C(\xi)}{E+C(\xi)}=\frac{E}{2(1+\nu_a)}\,\psi(\xi)\\ k_{ta}&=\frac{E}{3(1-2\,\nu_a)}\,\frac{C(\xi)}{E+C(\xi)}=\frac{E}{3(1-2\,\nu_a)}\,\psi(\xi)\end{aligned} \tag{2.37}$$

It is easy to observe that the constituents of the elastic tangent stiffness tensor are scaled by a function $\psi(\xi)$, that depends on the volume fraction of martensite (*Eq. 2.37*). The Hill incremental approach [53] allows us to update the value of the tangent stiffness operator at each step of the solution, taking into account the influence of martensitic inclusions on the overall behaviour of the material.

2.4.3. Homogenisation algorithm

The majority of engineering materials have heterogeneous structure when considering the microscopic level, and mathematical models that reflect in a proper way all the relations between individual constituents would make the analysis too complicated. Therefore, various methods of homogenisation have been developed. They all aim at replacing real material containing discrete inhomogeneities by equivalent continuum, characterised by continuous structure and effective, averaged properties (*Fig. 2.6*).

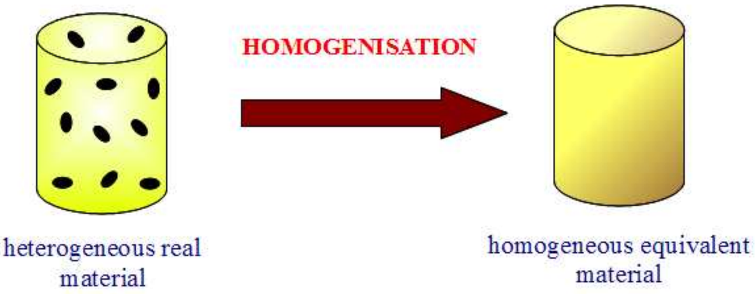

Figure 2.6: The idea of homogenisation.

The simplest methods of homogenisation are Voigt and Reuss schemes based on the rule of mixture. The Voigt method assumes that the strain field is homogeneous and determines the effective stiffness modulus by averaging the stresses, what finally leads to linear approximation:

$$\underline{\underline{\underline{\underline{E}}}}_{eff}=\sum_{i=1}^{n} f_i \underline{\underline{\underline{\underline{E}}}}_i \tag{2.38}$$

On the contrary, the Reuss method allows to calculate the effective stiffness modulus by averaging the strains and assuming the uniform stress field:

$$\underline{\underline{\underline{\underline{E}}}}_{eff}^{-1}=\sum_{i=1}^{n} f_i \underline{\underline{\underline{\underline{E}}}}_i^{-1} \tag{2.39}$$

Both Voigt and Reuss approximations define in general the upper and the lower bounds for the effective properties of heterogeneous material [54]. Another method of estimating the bounds of equivalent properties of materials was proposed by Hashin and Shtrikman and is based on the variational methods applied to nonhomogeneous linear elasticity [55]. Commonly used homogenisation schemes are also the self-consistent methods that define the effective properties of the embedding material with inclusions, introduced by Hershey [56] and Kröner [57].

The simplest methods, like these by Voigt and Reuss, do not take into account the effects of interactions between the inclusions and the matrix that influence the effective properties, especially when the differences in the elastic properties of constituents are significant. Taking into account the Eshelby's solution [19] for a single ellipsoidal inclusion embedded in an infinite homogeneous body subjected to a uniform transformation strain, it is possible to compute the stresses and the strains within the inclusion surrounded by the elastic matrix. This approach has been adopted a basis of many homogenisation methods, such as the Mori-Tanaka method. The Mori-Tanaka homogenisation scheme is an effective field theory based on calculating the average internal stress [58]. The effective stiffness modulus results from the following formula:

$$\left(\underline{\underline{\underline{\underline{E}}}}_{MT}+\underline{\underline{\underline{\underline{E}}}}^{Hill}\right)^{-1}=\sum_{i=a,m} f_i\left(\underline{\underline{\underline{\underline{E}}}}_i+\underline{\underline{\underline{\underline{E}}}}^{Hill}\right)^{-1} \tag{2.40}$$

where $\underline{\underline{\underline{\underline{E}}}}^{Hill}$ denotes here the Hill influence tensor and f_i is the volume fraction of a given constituent in the material (here: *a* – austenite, *m* – martensite).

Typical shapes of martensitic inclusions are plates or a laths. Therefore, when modelling materials with α'-phase, the assumption of ellipsoidal inclusions that are dispersed uniformly in the material is justified and enables us to use the Eshelby solution. The linearised stress-strain relationship in the material undergoing the phase transformation and consisting of a soft matrix and hard inclusions is based on the effective tangent stiffness operator $\underline{\underline{\underline{\underline{E}}}}_{eff}$:

$$\Delta\underline{\underline{\sigma}}_{a+m}=\underline{\underline{\underline{\underline{E}}}}_{eff}:\Delta\underline{\underline{\epsilon}} \tag{2.41}$$

where the effective stiffness tensor is obtained via the Mori-Tanaka homogenisation and can be decomposed into the bulk and shear terms:

$$\underline{\underline{\underline{\underline{E}}}}_{eff}=\underline{\underline{\underline{\underline{E}}}}_{MT}=3\mathrm{k}_{MT}\underline{\underline{\underline{\underline{J}}}}+2\mu_{MT}\underline{\underline{\underline{\underline{K}}}} \tag{2.42}$$

where the relations between the moduli are as follows:

$$\begin{gathered}
3k_{MT}+3k^*=\left[\frac{1-\xi}{3\left(k_{ta}+k^*\right)}+\frac{\xi}{3\left(k_m+k^*\right)}\right]^{-1}\\
2\mu_{MT}+2\mu^*=\left[\frac{1-\xi}{2\left(\mu_{ta}+\mu^*\right)}+\frac{\xi}{2\left(\mu_m+\mu^*\right)}\right]^{-1}\\
k^*=\frac{4}{3}\mu_{ta}\;;\;\;2\mu^*=\frac{\mu_{ta}(9k_{ta}+8\mu_{ta})}{3(k_{ta}+2\mu_{ta})}
\end{gathered} \tag{2.43}$$

The total increment of stress in the material can be decomposed into the stress increment for pure austenite (before the phase transition) and the surplus stress increment resulting from the phase transformation and formation of heterogeneous structure:

$$\Delta\underline{\underline{\sigma}}=\Delta\underline{\underline{\sigma}}_a+\Delta\underline{\underline{\sigma}}_{a+m}=\underline{\underline{\underline{\underline{E}}}}_{ta}:\Delta\underline{\underline{\epsilon}}+\left(\underline{\underline{\underline{\underline{E}}}}_{MT}-\underline{\underline{\underline{\underline{E}}}}_{ta}\right):\Delta\underline{\underline{\epsilon}} \tag{2.44}$$

The term desribing the influence of two-phase structure on the stress increment, together with the assumption that the strain increment is mainly due to the plastic strains, can be evaluated as:

$$\Delta\underline{\underline{\sigma}}_{a+m}=2(\mu_{MT}-\mu_{ta})\Delta\underline{\underline{\epsilon}}^p=C_{a+m}\Delta\underline{\underline{\epsilon}}^p \tag{2.45}$$

where μ_{MT} is the shear modulus obtained via the Mori-Tanaka homogenisation process and C_{a+m} represents the hardening modulus for the two-phase material.

If pure kinematic hardening is taken into account only, the formula describing backstress increment in two-phase material is expressed in the following way:

$$\Delta \underline{\underline{X}}_{a+m} = \frac{2}{3} C_{a+m} \Delta \underline{\underline{\epsilon}}^{p} \tag{2.46}$$

which can also be written in the incremental form as:

$$d \underline{\underline{X}}_{a+m} = \frac{2}{3} C_{a+m} d \underline{\underline{\epsilon}}^{p} \tag{2.47}$$

In the case of pure isotropic hardening, evolution of the hardening parameter looks as follows:

$$\Delta R = \Delta R_{a+m} = \left\| \Delta \underline{\underline{\sigma}}_{a+m} \right\| = \sqrt{\Delta \underline{\underline{\sigma}}_{a+m} : \Delta \underline{\underline{\sigma}}_{a+m}} = 2\left(\mu_{MT} - \mu_{ta}\right) \Delta p \tag{2.48}$$

where the accumulated plastic strain increment is computed as:

$$\Delta p = \sqrt{\frac{2}{3} \Delta \underline{\underline{\epsilon}}^{p} : \Delta \underline{\underline{\epsilon}}^{p}} \tag{2.49}$$

The incremental form of isotropic hardening parameter can be written as:

$$d R = d R_{a+m} = \left\| \Delta \underline{\underline{\sigma}}_{a+m} \right\| = 2\left(\mu_{MT} - \mu_{ta}\right) dp = C_{a+m} dp \tag{2.50}$$

Usually both the kinematic and the isotropic hardening is observed in the materials, however one of them can be dominant. Thus, the Bauschinger parameter β has been introduced with the parametrization developed by Życzkowski [59]:

$$\beta = \frac{\sigma' + \sigma'^{-}}{2\left(\sigma' - \sigma_0\right)}; \quad 0 \leqslant \beta \leqslant 1 \tag{2.51}$$

where σ' represents the stress level at which the unloading process starts and σ'^{-} is the stress level at the reverse active process (*Fig. 2.7*). This parameter allows us to determine the ratio between isotropic hardening (no Bauschinger effect, $\beta = 0$) and kinematic hardening (ideal Bauschinger effect, $\beta = 1$) and can be determined experimentally in uniaxial tension – compression tests.

Finally, the hardening parameters in the mixed hardening model are expressed as:

$$d \underline{\underline{X}} = \frac{2}{3} \beta C_{a+m} d \underline{\underline{\epsilon}}^{p} \tag{2.52}$$

$$d R = \left(1 - \beta\right) C_{a+m} dp \tag{2.53}$$

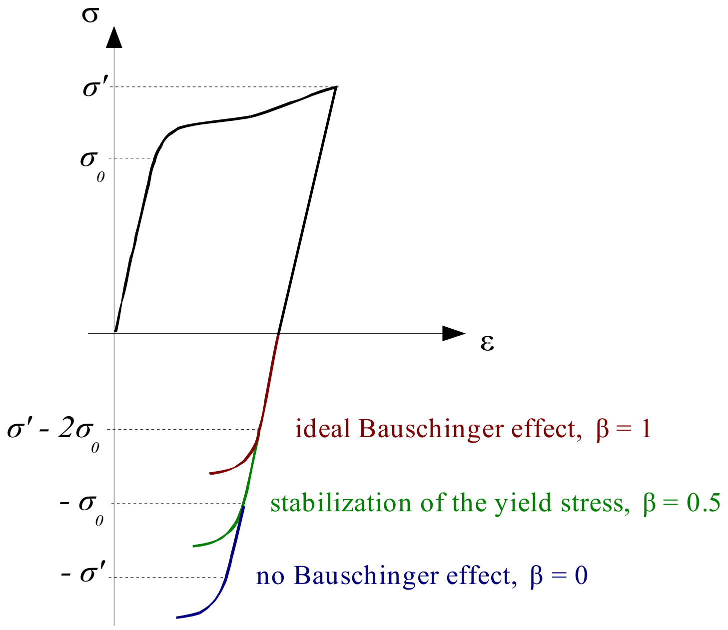

Figure 2.7: Bauschinger effect and parameter β.

2.5. Numerical application in ANSYS

Finite element method (FEM) is a powerful tool that enables us to find approximate solutions of boundary problems described by means of partial differential equations. The main idea of the FEM consists in replacing local forms of equations by global, variational forms. Thus, instead of solving differential equations, the problem is reduced to set of linear equations, which can be easily and efficiently solved by using numerical algorithms.

Nowadays, there exist many commercial programs based on the finite element method, that help to solve various engineering problems generated by the structural analysis, electromagnetics, fluid mechanics and others, both linear and non-linear, steady-state and transient. Among them, one of the most popular is ANSYS.

Thanks to its open architecture, ANSYS offers the possibility of modifying or extending software packages by providing access to the set of Fortran functions and routines, called User Programmable Features (UPFs), which can be adjusted depending on users' needs [60]. The UPFs enable us to create new elements, change specifications of existing elements, create materials with custom properties, modify constitutive laws (plasticity, creep, damage, etc.) or prepare procedures for other calculations. Using these procedures requires relinking ANSYS, which results in a custom version of the software.

In order to take into account the influence of martensitic inclusions on hardening of the material, the USERPL procedure is used. The procedure allows users to write their own plasticity laws. In this procedure, the material data has to be defined by user-defined data-table (`TB,USER` command), which is an indication in the custom version that the program should use USERPL procedure when computing stresses and strains. The list of elements that support USERPL procedure is given in *Table 2.1* [61].

The program enters the procedure within every load step when computing the stress-strain relationship in each element. First of all, for the current strain state, the volume fraction of martensite ξ is determined and based on this the moduli C_X and C_R as well as all homogenisation parameters are calculated. Then, the backstress $\underline{\underline{X}}$ and the trial stress $\underline{\underline{\sigma}}^{tr}$ are evaluated. When the stress state is determined, one can compute the equivalent stress $(\underline{\underline{\sigma}}^{tr} - \underline{\underline{X}})_{eq}$. If the equivalent stress is smaller than $\sigma_0 + R$ the material is elastic and no plastic strain increment is computed.

Table 2.1: The elements that support user-defined plasticity laws.

Structural line	LINK1 (2D), LINK8 (3D)
Structural pipe	PIPE20, PIPE60
Structural beam	BEAM23 (2D), BEAM24 (3D)
Structural shell	SHELL43 (3D), SHELL51 (2D), SHELL93 (3D), SHELL143 (3D)
Structural solid	PLANE2 (2D), PLANE42 (2D), PLANE82 (2D), SOLID45 (3D), SOLID65 (3D), SOLID92 (3D), SOLID95 (3D)
Structural layered composite	SHELL91 (3D)
Couple-field	SOLID62 (3D)

However, as soon as the equivalent stress exceeds the yield stress, the plastic multiplier λ is determined by the local Newton-Raphson iteration procedure from the consistency condition (*Eq. 2.11*), which takes the following form:

$$\dot{f}(\underline{\underline{\sigma}}, \underline{\underline{X}}, R) = \frac{\partial f}{\partial \underline{\underline{\sigma}}} : \dot{\underline{\underline{\sigma}}} + \frac{\partial f}{\partial \underline{\underline{X}}} : \dot{\underline{\underline{X}}} + \frac{\partial f}{\partial R} \dot{R} = 0 \tag{2.54}$$

By substituting expressions related to the constitutive law (*Eq. 2.3*) and the evolution of hardening parameters (*Eqs 2.12* and *2.13)*, the consistency conditions is derived as:

$$\frac{\partial f}{\partial \underline{\underline{\sigma}}} : \underline{\underline{\underline{\underline{E}}}} : \left(\dot{\underline{\underline{\epsilon}}} - \dot{\underline{\underline{\epsilon}}}^{p} - \dot{\xi} \underline{\underline{\epsilon}}^{bs} \right) + C_X(\xi) \frac{\partial f}{\partial \underline{\underline{X}}} : \dot{\underline{\underline{\epsilon}}}^{p} + C_R(\xi) \frac{\partial f}{\partial R} \dot{p} = 0 \tag{2.55}$$

where the derivatives of the yield function are equal to:

$$\frac{\partial f}{\partial \underline{\underline{\sigma}}} = \frac{3}{2\sigma_{eq}} \left(\underline{\underline{s}} - \underline{\underline{X}} \right) \ , \quad \frac{\partial f}{\partial \underline{\underline{X}}} = -\frac{\partial f}{\partial \underline{\underline{\sigma}}} \ , \quad \frac{\partial f}{\partial \underline{\underline{\sigma}}} : \frac{\partial f}{\partial \underline{\underline{\sigma}}} = \frac{3}{2} \ , \quad \frac{\partial f}{\partial R} = -1 \tag{2.56}$$

Thus, the consistency condition takes the form:

$$\frac{\partial f}{\partial \underline{\underline{\sigma}}} : \underline{\underline{\underline{\underline{E}}}} : \dot{\underline{\underline{\epsilon}}} - \left[\frac{\partial f}{\partial \underline{\underline{\sigma}}} : \underline{\underline{\underline{\underline{E}}}} : \left(\frac{\partial f}{\partial \underline{\underline{\sigma}}} + A \underline{\underline{\epsilon}}^{bs} \right) + \frac{3}{2} C_X(\xi) + C_R(\xi) \right] \dot{\lambda} = 0 \tag{2.57}$$

The plastic multiplier λ is computed as:

$$\dot{\lambda}=\frac{1}{H(\xi)}\frac{\partial f}{\partial \underline{\underline{\sigma}}}:\underline{\underline{\underline{\underline{E}}}}:\dot{\underline{\underline{\epsilon}}} \tag{2.58}$$

where:

$$H(\xi)=\frac{\partial f}{\partial \underline{\underline{\sigma}}}:\underline{\underline{\underline{\underline{E}}}}:\left(\frac{\partial f}{\partial \underline{\underline{\sigma}}}+A\underline{\underline{\epsilon}}^{bs}\right)+\frac{3}{2}C_X(\xi)+C_R(\xi) \tag{2.59}$$

The increment of plastic strain is evaluated according to the associated flow rule (*Eq. 2.10*). Then, the current plastic strain is updated and the elastic strain is computed. Finally, based on the constitutive law, the stress is evaluated [62].

In view of the above equations, the general constitutive law may be written in the incremental form as:

$$\dot{\underline{\underline{\sigma}}}=\underline{\underline{\underline{\underline{E}}}}:(\dot{\underline{\underline{\epsilon}}}-\dot{\underline{\underline{\epsilon}}}^{p}-\dot{\xi}\underline{\underline{\epsilon}}^{bs})=\underline{\underline{\underline{\underline{E}}}}:\dot{\underline{\underline{\epsilon}}}-\underline{\underline{\underline{\underline{E}}}}:\left(\frac{\partial f}{\partial \underline{\underline{\sigma}}}+A\underline{\underline{\epsilon}}^{bs}\right)\dot{\lambda} \tag{2.60}$$

By substituting the plastic multiplier, one obtains:

$$\dot{\underline{\underline{\sigma}}}=\underline{\underline{\underline{\underline{E}}}}:\dot{\underline{\underline{\epsilon}}}-\frac{1}{H(\xi)}\left(\underline{\underline{\underline{\underline{E}}}}:\frac{\partial f}{\partial \underline{\underline{\sigma}}}\right)\frac{\partial f}{\partial \underline{\underline{\sigma}}}:\underline{\underline{\underline{\underline{E}}}}:\dot{\underline{\underline{\epsilon}}}-\frac{A}{H(\xi)}\left(\underline{\underline{\underline{\underline{E}}}}:\underline{\underline{\epsilon}}^{bs}\right)\frac{\partial f}{\partial \underline{\underline{\sigma}}}:\underline{\underline{\underline{\underline{E}}}}:\dot{\underline{\underline{\epsilon}}} \tag{2.61}$$

The tangent stiffness tensor is derived from the above equation in the following form:

$$\underline{\underline{\underline{\underline{E}}}}_t=\underline{\underline{\underline{\underline{E}}}}-\frac{1}{H(\xi)}\left(\underline{\underline{\underline{\underline{E}}}}:\frac{\partial f}{\partial \underline{\underline{\sigma}}}\right)\otimes\left(\frac{\partial f}{\partial \underline{\underline{\sigma}}}:\underline{\underline{\underline{\underline{E}}}}\right)-\frac{A}{H(\xi)}\left(\underline{\underline{\underline{\underline{E}}}}:\underline{\underline{\epsilon}}^{bs}\right)\otimes\left(\frac{\partial f}{\partial \underline{\underline{\sigma}}}:\underline{\underline{\underline{\underline{E}}}}\right) \tag{2.62}$$

The algorithm of this procedure is shown in the form of flowchart in *Fig. 2.8.*

Application of this numerical procedure integrated in ANSYS offers almost unlimited possibilities of computing mechanical behaviour of complex structures undergoing phase transformations. What is more, it provides also a method of optimising materials with respect to martensite content, which is of great importance in the case of design of all structures working at cryogenic temperatures.

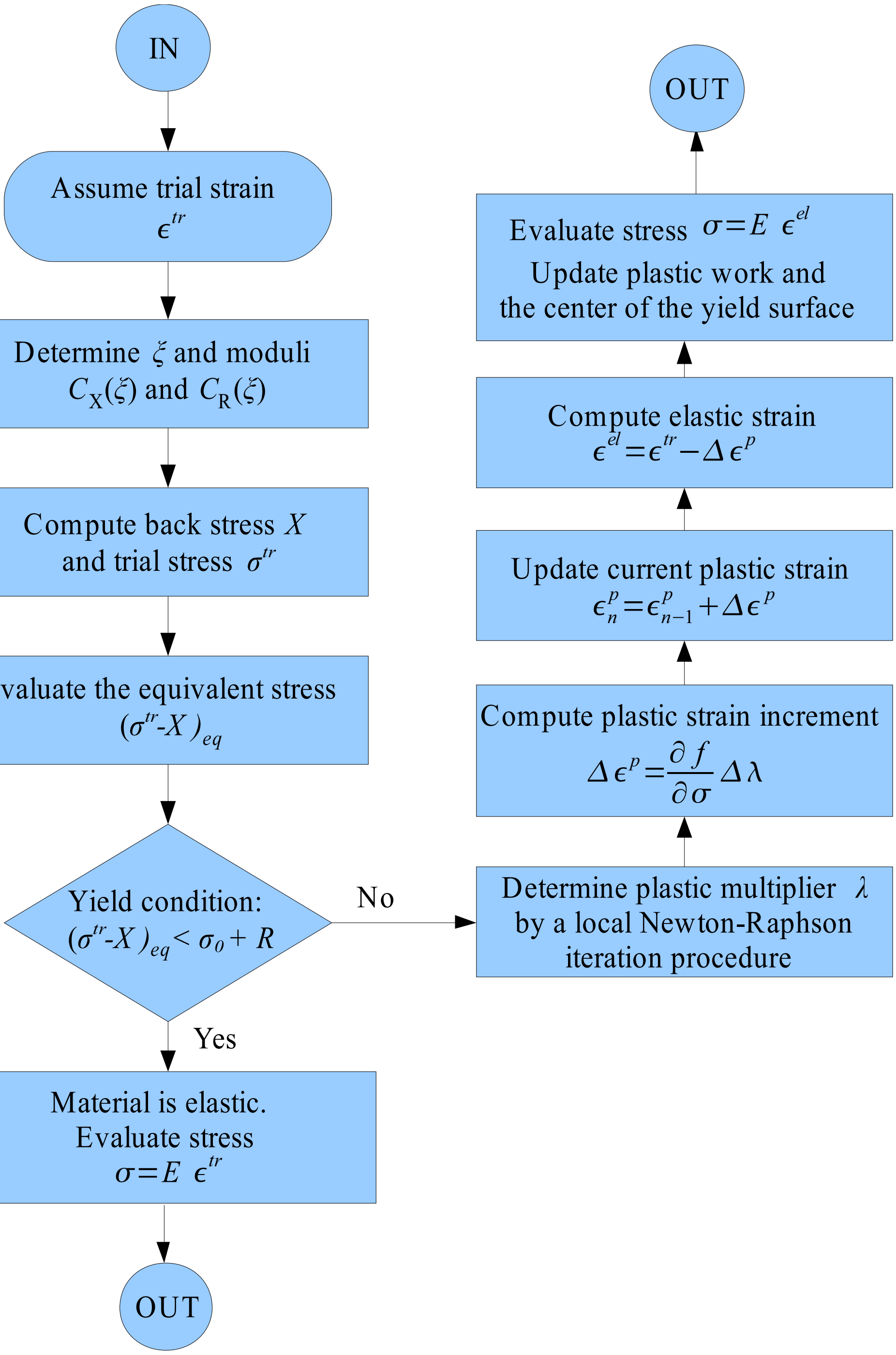

Figure 2.8: Flowchart presenting USERPL subroutine.

3. TENSION AND COMPRESSION OF RODS

3.1. Experimental results and evaluation of parameters

Tension or compression of rods does not lead to creation of functionally graded structural member (FGSM) because the distribution of stresses and strains resulting from such type of loads is homogeneous in the cross-section and along the structure. However, these uniaxial cases are analysed here in order to identify the material parameters of the constitutive model and cross-check the numerical results with experimental data.

All parameters of the constitutive model are evaluated based on the experimental data obtained in monotonic tension and cyclic tension-compression tests. It is rather difficult to find in the literature the experimental data for austenitic stainless steels loaded in cryogenic conditions because this type of tests requires specialised equipment working at extremely low temperatures and providing constant or programmed temperature during the tests.

The model requires essentially 10 material parameters to be defined. Young's modulus E, Poisson's ratio ν, yield stress σ_0 and hardening modulus C_0 can be directly identified from the stress-strain curve obtained in the tensile test (*Fig. 3.11*). Parameter β defining the proportion between the isotropic and the kinematic hardening is estimated based on the cyclic tests. Parameter h is a free parameter and is adjusted in such a way that the numerically obtained stress-strain relationship fits best to the experimental data.

The parameters referring to the kinetics of martensitic transformation: such as the threshold value of accumulated plastic strain p_ξ at which the phase transformation starts, the parameter A determining slope of the linearised part of transformation curve as well as saturation level of the transformation ξ_L, are evaluated based on the measurements of magnetic response of the material (*Fig. 3.11*). The magnetic properties of individual phases (paramagnetic γ austenite and ferromagnetic α' martensite) are used to estimate the amount of martensite in the material. The magnetic permeability of steel changes as a function of the content of ferromagnetic martensite and can be measured by using a magnetometer. Then, the measured permeability level can be directly converted to the volume fraction of martensite.

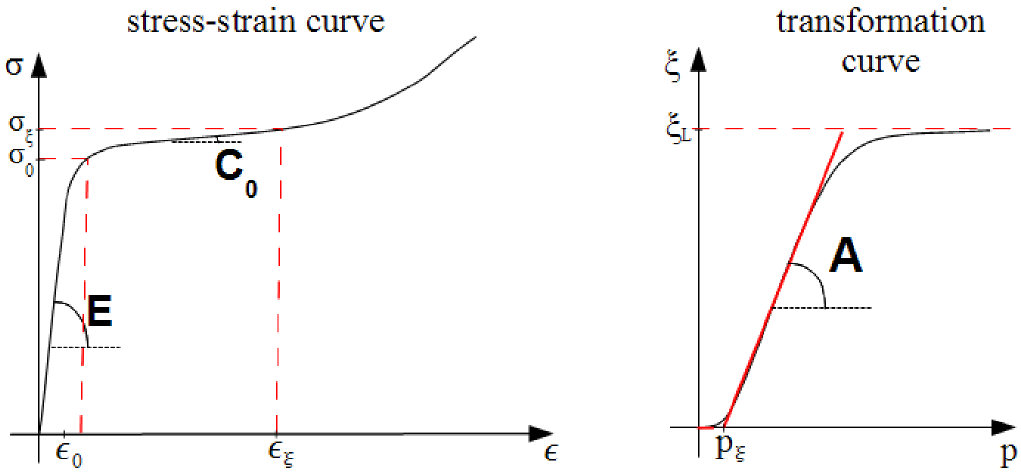

Figure 3.1: Experimental curves and main parameters of the model.

Mechanical properties of 316L stainless steel at 77K, with special consideration of phase transformation, were investigated by Garion et al. [63]. Two samples of cross sections *0.15mm* x *3mm* and *0.25mm* x *3mm*, respectively, were tested in liquid nitrogen. The chemical composition of steel for both specimens was identified and the results are given in *Table 3.1*. The kinematically controlled tensile tests were performed by using a universal electromechanical testing machine with a special cryostat installed. In order to identify the threshold strain at which the phase transformation begins, the volume fraction of martensite was estimated for different strain levels: 0.05, 0.1, 0.2, 0.3 and 0.4. The magnetic measurements were carried out by removing the sample from the cryogen as soon as the required deformation was obtained and measuring the permeability at room temperature. Resulting stress-strain curve and the volume fraction of martensite as a function of strain are shown in *Fig. 3.2*. The authors performed also similar tests of 316L stainless steel in liquid helium temperature (4.2K).

Table 3.1: Chemical composition of AISI 316L samples (wt %).

316L sample	**C**	**Cr**	**Ni**	**Mn**	**Mo**	**N**	**P**	**S**	**Si**	**Fe**
0.15mm x *3mm*	0.027	17.99	10.29	1.56	2.03	0.0075	0.022	0.0009	0.596	Bal.
0.25mm x *3mm*	0.029	17.91	11.03	0.87	1.97	0.0074	0.025	0.0022	0.492	Bal.

The properties of 304L stainless steel were defined on the basis of tests performed by Morris et al. [64]. The chemical composition of samples is presented in *Table 3.2*.

The stress-strain curve and the volume fraction of martensite as a function of strain obtained from experiments are shown in *Fig. 3.2*.

Table 3.2: Chemical composition of AISI 304L steel (wt %).

	C	**Cr**	**Ni**	**Mn**	**Mo**	**N**	**P**	**S**	**Si**	**Fe**
304L	0.019	18.9	8.29	1.84	0.43	0.087	0.024	0.015	0.033	Bal.

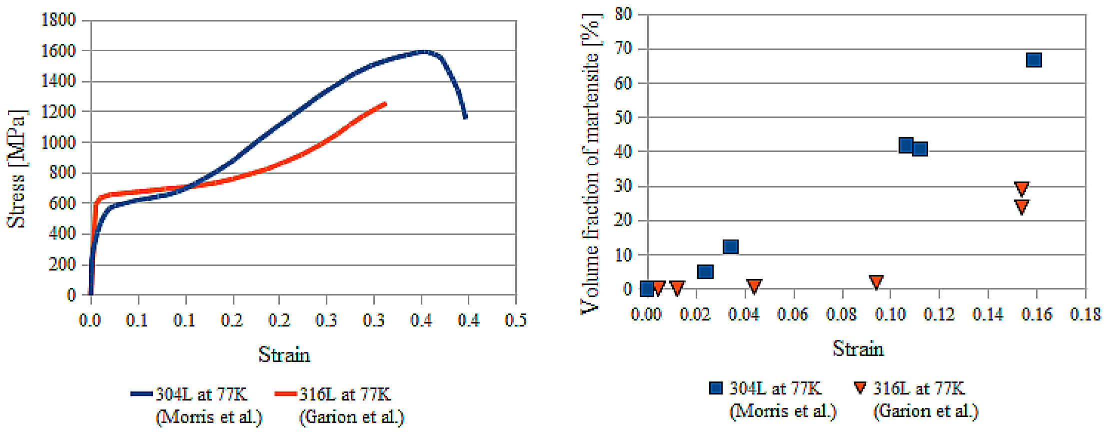

Figure 3.2: Experimental curves according to [64] for 304L steel and [63] for 316L steel.

The set of material parameters identified on the basis of tensile tests and magnetic measurements for 304L and 316L is given in *Table 3.3*. These parameters are used in all calculations presented in the Thesis unless otherwise stated.

Table 3.3: Parameters of constitutive model for 316L (based on Garion et al. [63]) and 304L (based on Morris et al. [64]) stainless steels at 77 K.

Steel	**E [GPa]**	**ν**	**σ_0 [MPa]**	**C_0 [MPa]**	**h**	**A**	**p_ξ**	**ξ_L**	**Δv**
304L	190	0.3	580	750	1.9	4.23	0.004	0.3	0.05
316L	206	0.3	645	720	0.7	4.3714	0.0886	0.9	0.05

It should be pointed out that the saturation level of the phase transformation ξ_L may change significantly depending on the chemical composition of steel. Due to the fact that homogenisation algorithm models the two-phase structure assuming that the martensitic inclusions are dispersed in the austenitic matrix, therefore austenite is the dominant constituent of material. The maximum saturation level in all calculations should not be assumed greater than 0.5 ($\xi_L \leq 0.5$). However, in the calculations performed for 304L stainless steel the value 0.9, resulting from the tests, is used and still good agreement between numerical analyses and experimental data can be achieved. However in this case the results for the accumulated plastic strains larger than 0.12 should be analysed with additional care.

3.2. General 1D constitutive model of material with phase transformation

Based on the general constitutive law related to the material undergoing the plastic strain-induced phase transformation and presented in Chapter 2, the special case of 1D state equations is derived. In the elastic range, the linear elasticity constitutive law in one-dimensional case is applied up to the point where the plastic threshold ϵ_0, corresponding to the yield point σ_0, is reached:

$$\sigma^e = E\epsilon \quad \text{for} \quad \epsilon \leqslant \epsilon_0 \tag{3.1}$$

When the material becomes elastic-plastic, but before the phase transformation starts, the linear hardening takes place, which can be described as:

$$\sigma_1^p = \sigma_0 + C_0(\epsilon - \epsilon_0) \quad \text{for} \quad \epsilon_0 \leqslant \epsilon \leqslant \epsilon_\xi \tag{3.2}$$

where σ_0 stands for the yield stress, C_0 is the hardening modulus and ϵ_ξ denotes the phase transformation threshold.

As soon as the γ→α' transformation starts, the influence of martensitic inclusions must be included in the constitutive model. Because the relationship between stress and strain in no longer linear, the incremental formulation of the constitutive equations is used (Hill's concept [53]), which takes into account linear hardening, interaction of inclusions and dislocations as well as homogenization procedure:

$$d\sigma_2^p = d\sigma_{lin} + d\sigma_{int} + d\sigma_{MT} = C_0 d\epsilon + C_0 h\xi d\epsilon + C_{a+m} d\epsilon \quad \text{for} \quad \epsilon \geqslant \epsilon_\xi \tag{3.3}$$

Here C_{a+m} represents the tangent stiffness modulus due to homogenization for the two-phase material composed of martensite and austenite.

The volume fraction of martensite is obtained from the kinetic law of phase transformation. Assuming that the parameter A is constant, which is justified for the isothermal processes, one obtains linear relationship describing the volume fraction of martensite as a function of the current strain $\tilde{\epsilon}$ (*Fig. 3.3*):

$$\xi(\epsilon) = \int_{\epsilon_\xi}^{\tilde{\epsilon}} A\, d\epsilon = A(\tilde{\epsilon} - \epsilon_\xi) \tag{3.4}$$

The tangent stiffness modulus C_{a+m}, resulting from Mori-Tanaka homogenisation scheme, can be expressed as:

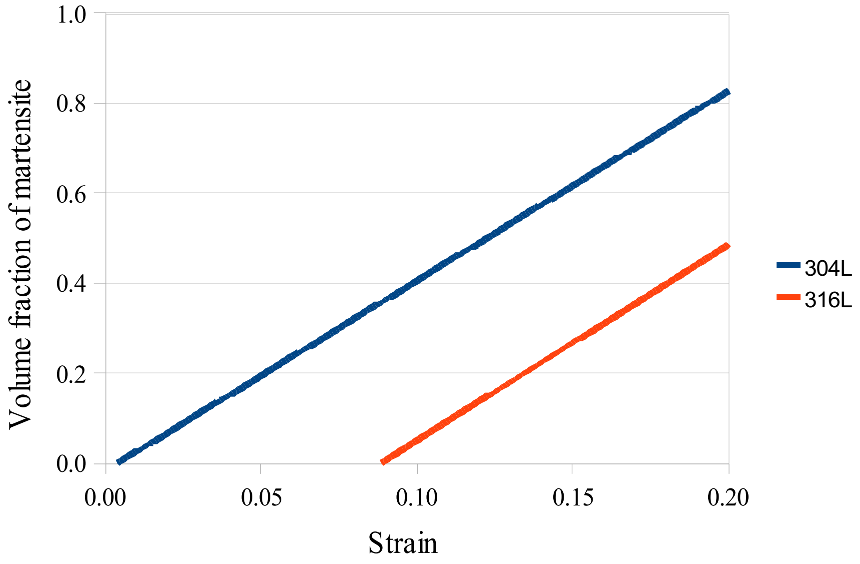

Figure 3.3: Volume fraction of martensite as a function of strain.

$$C_{a+m}(\xi)=2(\mu_{MT}-\mu_{ta})=\left[\frac{1-\xi}{2(\mu_{ta}+\mu^*)}+\frac{\xi}{2(\mu_m+\mu^*)}\right]^{-1}-2\mu^*-2\mu_{ta} \tag{3.5}$$

With the onset of phase transformation, the austenite matrix becomes plastic which implies the fact that Poisson's ratio of the austenite is equal to *0.5*. Then, the tangent bulk modulus of austenite tends to infinity $k_{ta}\rightarrow\infty$ and thus $1/k_{ta}\rightarrow 0$. Consequently, the shear modulus is equal to one third of the tangent stiffness of austenite $\mu_{ta}=E_t/3$. The above assumption leads to the tangent stiffness modulus written as:

$$C_{a+m}(\xi)=\frac{5E_t\xi(Ea-E_t)}{(1+\nu_a)[2Ea(1-\xi)+E_t(3+2\xi)]} \tag{3.6}$$

where *a* is a constant parameter expressing the relationship between the Poisson's ratio of martensite ν_m and the Poisson's ratio of austenite ν_a:

$$a=\frac{1+\nu_a}{1+\nu_m} \tag{3.7}$$

Substituting the expression for tangent modulus of austenite $E_t=\frac{EC(\xi)}{E+C(\xi)}$, *Eq. 3.6* is transformed to the following form:

$$C_{a+m}(\xi)=\frac{5E}{2(1+\nu_a)}\frac{\eta}{1+\eta}\frac{\xi}{\frac{2a(1+\eta)+3\eta}{2a(1+\eta)-2\eta}-\xi} \tag{3.8}$$

where η determines the ratio between the hardening modulus *C(ξ)* and the Young's modulus *E*:

$$\eta(\xi)=\frac{C(\xi)}{E}=\frac{C_0(1+h\xi)}{E} \tag{3.9}$$

The values of η in the defined range of plastic strains (up to 0.2) stay below 0.005 for 316L stainless steel and reach the maximum value of 0.01 for 304L stainless steel (*Fig. 3.4*). Thus, one can assume that $\eta \ll 1$ and, further, that $1+\eta \approx 1$ in this specific range. Therefore, *Eq. 3.8* simplifies to the following form:

$$C_{a+m}(\xi)=\frac{5E\eta\xi}{3(1-\xi)} \tag{3.10}$$

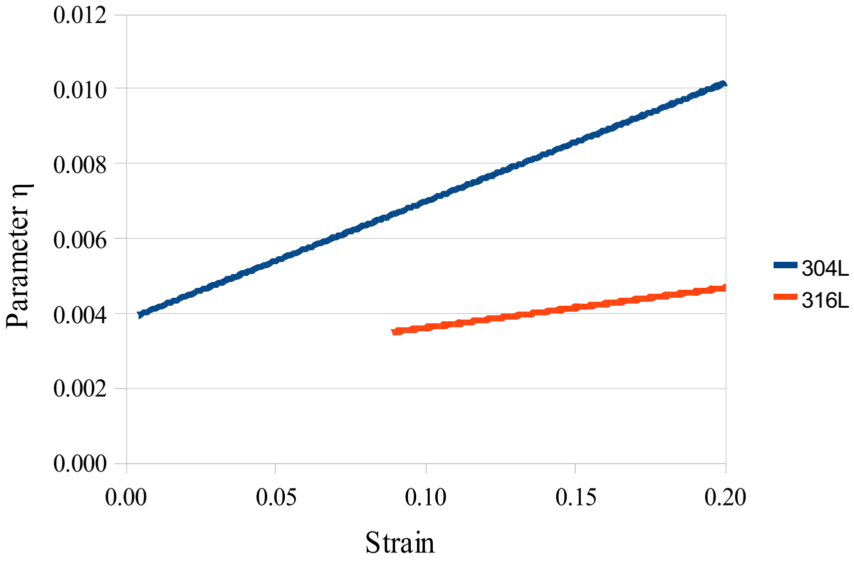

Figure 3.4: Parameter η as a function of strain.

Thanks to the simplification of the formula *3.1* and by substituting the kinetic law of phase transformation (*Eq. 3.4*) one obtains the homogenised modulus of two-phase material as a function of strain:

$$C_{a+m}(\epsilon)=\frac{5C_0A\left[1+hA(\epsilon-\epsilon_\xi)\right](\epsilon-\epsilon_\xi)}{3\left[1-A(\epsilon-\epsilon_\xi)\right]} \tag{3.11}$$

The comparison of the above simplified version of the hardening modulus and the exact value obtained from *Eq. 3.5* shows that the maximum relative error does not exceed 2.5% for 316L steel and 15% for 304L steel in the small strain range ($\epsilon \leqslant 0.2$), which is illustrated in *Fig. 3.5*.

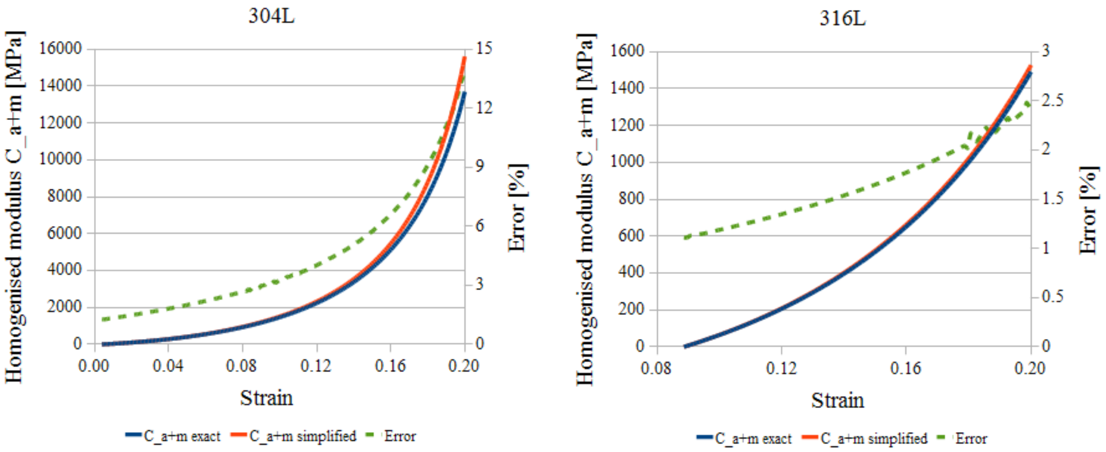

Figure 3.5: Comparison of exact and simplified C_{a+m} moduli for 304L and 316L steel.

By reordering the components of *Eq. 3.11*, one obtains the final form of homogenised tangent stiffness modulus with a quadratic function of strain in the numerator and a linear function of strain in the denominator:

$$C_{a+m}(\epsilon)=\frac{A_1\epsilon^2+A_2\epsilon+A_3}{A_4\epsilon+A_5} \tag{3.12}$$

where $A_1,\ldots,A_5$ are constant coefficients, that are introduced in order to abbreviate the notation:

$$\begin{gathered} A_1=5A^2C_0h \\ A_2=5AC_0(1-2\mathrm{hA}\,\epsilon_\xi) \\ A_3=5AC_0\epsilon_\xi(hA\epsilon_\xi-1) \\ A_4=-3\mathrm{A} \\ A_5=3(1+A\epsilon_\xi) \end{gathered} \tag{3.13}$$

The total stress value in the range of phase transformation is evaluated by integrating *Eq. 3.3* over the plastic strain:

$$\sigma_2^p=\sigma_\xi+\int_{\epsilon_\xi}^{\epsilon}C_0(1+hA(\epsilon-\epsilon_\xi))\,d\epsilon+\int_{\epsilon_\xi}^{\epsilon}C_{a+m}(\epsilon)\,d\epsilon \tag{3.14}$$

where σ_ξ is the stress level relevant to the strain ϵ_ξ, at which the phase transformation is induced.

The stress increment σ_{a+m} obtained due to the homogenisation of two-phase material is represented by integral of the homogenised modulus C_{a+m}:

$$\sigma_{a+m}=\int_{\epsilon_\xi}^{\epsilon}C_{a+m}(\epsilon)\,d\epsilon=B_1\epsilon^2+B_2\epsilon+B_3\ln(A_4\epsilon+A_5)-B_4 \tag{3.15}$$

where $B_1,\ldots,B_5$ are constant coefficients equal to:

$$
\begin{aligned}
B_1 &= \frac{A_1}{2A_4} \\
B_2 &= \frac{A_2 A_4 - A_1 A_5}{A_4^2} \\
B_3 &= \frac{A_3 A_4^2 - A_2 A_4 A_5 + A_1 A_5^2}{A_4^3} \\
B_4 &= B_1 \epsilon_\xi^2 + B_2 \epsilon_\xi + B_3 \ln(A_4 \epsilon_\xi + A_5)
\end{aligned} \tag{3.16}
$$

Finally, the direct formula for stress as a function of strain during the phase transformation is:

$$\sigma_2^p = C_0 \left[(\epsilon - \epsilon_\xi) + \frac{1}{2} h A (\epsilon - \epsilon_\xi)^2 \right] + B_1 \epsilon^2 + B_2 \epsilon + B_3 \ln(A_4 \epsilon + A_5) - B_4 \tag{3.17}$$

The calculated stress-strain distributions for 304L and 316L are shown in *Figs. 3.6* and *3.7*, respectively.

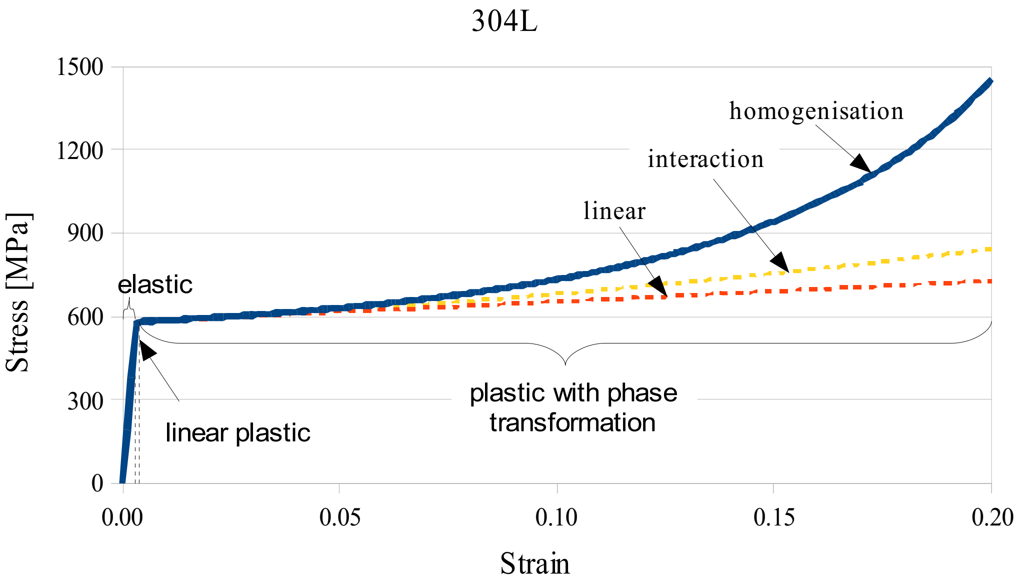

Figure 3.6: Stress vs strain for 304L stainless steel.

Due to the fact that the constitutive model accounts for the influence of phase transformation on the material hardening, there is a significant difference between the linear hardening model and the phase transformation model. In the case of 304L stainless steel, the phase transformation is initiated immediately after reaching the plastic state. Therefore, the range of plastic deformation with linear hardening is significantly reduced and strong nonlinear hardening due to the presence of martensite can be observed. For 316L stainless steel all three domains representing elastic, linear plastic and nonlinear plastic hardening ranges are well visible.

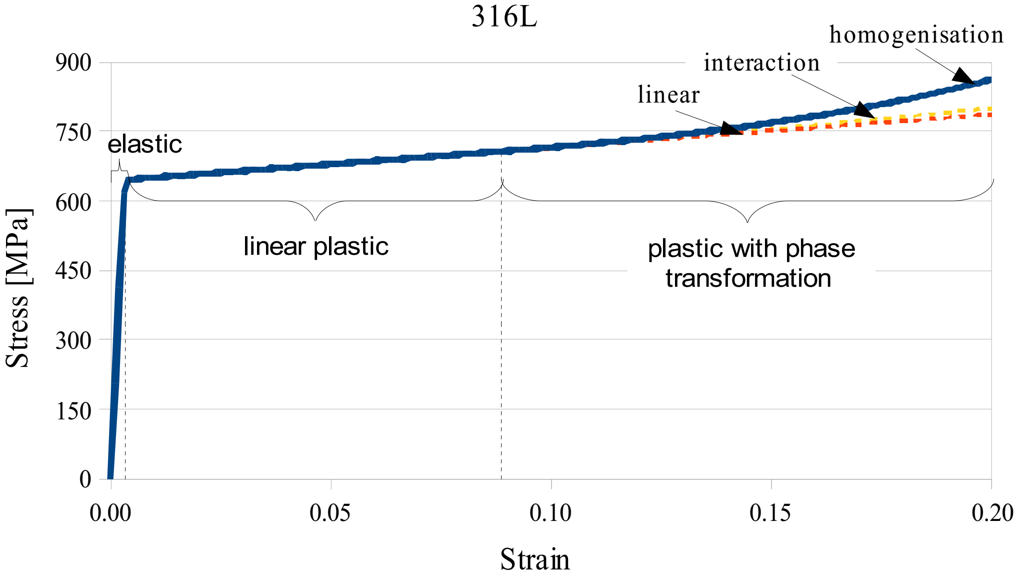

Figure 3.7: Stress vs strain for 316L stainless steel.

3.3. Finite element analysis of monotonic tension

In order to verify the finite element procedure presented in Chapter 2, monotonic tensile test in the range of phase transformation is simulated in ANSYS. Two different models of tensile bar are built in order to test the USERPL procedure (*Fig. 3.8*):

- 2D model by using PLANE42 elements. PLANE42 are 2D structural solid elements with four nodes, having two degrees of freedom at each node: displacement in the nodal *x* and *y* directions [65].
- 3D model by using SOLID45 elements. SOLID45 are 3D elements characterised by eight nodes having three degrees of freedom at each node: displacement in the nodal *x*, *y*, and *z* directions [65].

Both types of the above mentioned elements will also be used in further calculations concerning bending of beams, torsion of rods and more complex structures.

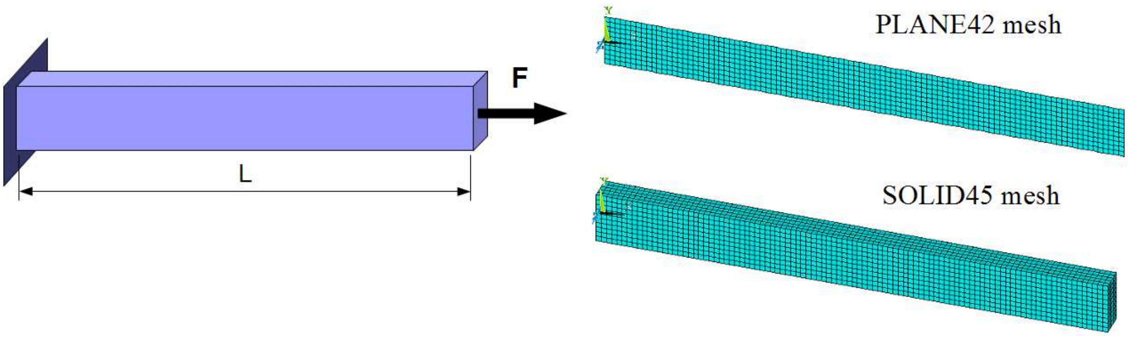

Figure 3.8: Boundary conditions and mesh for the numerical traction test.

A comparison of the results obtained by means of numerical simulations, analytical solution of 1D model and experimental data is shown in *Figs. 3.9* and *3.1*. For 316L steel excellent agreement between experiment and modelling is obtained up to the 0.2 strain level. At higher strains the results start to diverge. In the case of 304L steel the results are convergent up to 0.15 strain level. Then, the analytical solution gives overestimated values of stresses but the finite element models still converge well with

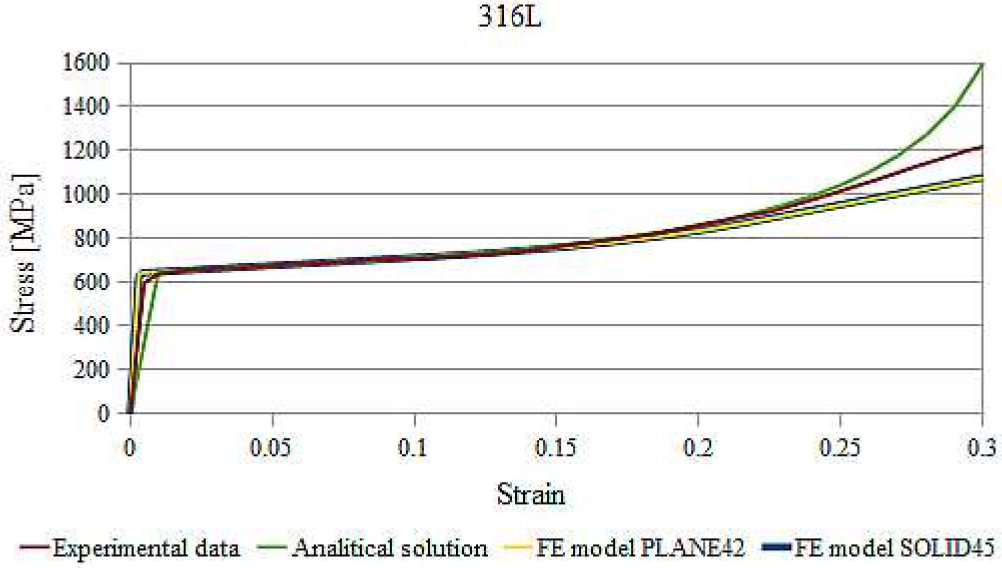

Figure 3.9: Comparison between experimental, numerical and analytical traction curves for 316L steel at 77 K.

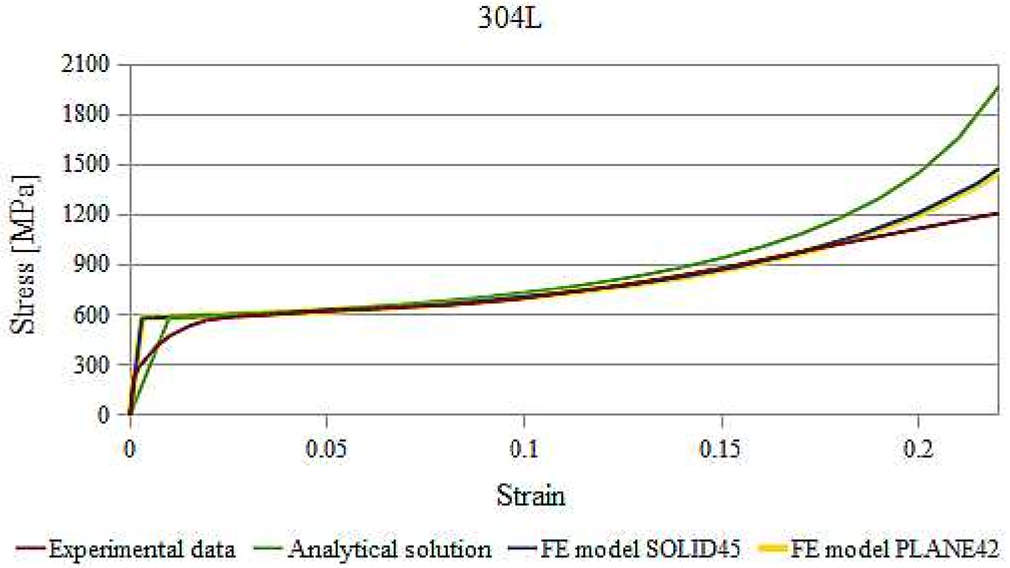

Figure 3.10: Comparison between experimental, numerical and analytical traction curves for 304L steel at 77 K.

the experimental results up to 0.2 strain. Based on these results, it is stated that the constitutive model represents correctly the behaviour of both metastable stainless steels for the strain range below 0.2 and for the temperature of liquid nitrogen (77K).

The divergence between the analytical solution and finite element results, backed by the experimental data, for 304L stainless steel can be easily explained by enhanced error of C_{a+m} modulus for the strain value above 0.15 (*Fig. 3.5*). On the other hand, the closed-form solutions obtained by means of the analytical approach have large value for practical engineering applications.

3.4. Cyclic tension/compression with phase transformation

Although the constitutive model of material undergoing γ→α' phase transformation is dedicated to monotonic loading and does not take into account the mechanisms related to fatigue and to cyclic hardening, it is used here in order to investigate the influence of martensitic transformation on the hardening of steels under cyclic loading. Moreover, the mechanisms of adaptation and inadaptation to cyclic loads are studied.

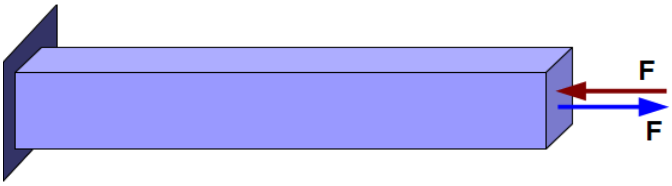

Figure 3.11: Rod subjected to cyclic tension/compression.

The 2D finite element models of rods, made of 304L stainless steels, are tested under uniaxial cyclic straining. The rods are subjected to tension and compression at cryogenic temperatures (77 K) with the strain amplitudes of 1.06%, 1.4% and 2.36%. The values of loads have been chosen on the basis of experimental data available in the literature and presented by Suzuki et al. for 304L stainless steel [45]. The experimental data presented in the articles are not sufficient to perform full identification of the parameters required by the constitutive model. Only the yield strength has been modified for the simulations according to the values given in the article: *353MPa* for 304L. The other parameters have been assumed as in *Table 3.3*.

Based on the best fit between cyclic tests and numerical analyses, the Bauschinger parameter $\beta = 0.9$ has been chosen for both steels. It implies the fact that kinematic hardening dominates over the isotropic hardening and suggests that the yield surface during cyclic loading moves in the stress space without increasing much its size. From the curves presenting evolution of the stress amplitude (*Fig. 3.12*) one can easily deduce that for bigger strain amplitudes the martensitic transformation is initiated much faster and significantly increases the stress level during loading. It shows that the martensitic phase transformation has big influence on the strain hardening. It is well known that martensitic inclusions are beneficial for the fatigue strength of materials. They are often created in the regions of the biggest local strain concentrations that are usually located at the tip of propagating crack. The presence of hard martensite stops the growth of the crack and, additionally, may also initiate the closure of short cracks [66].

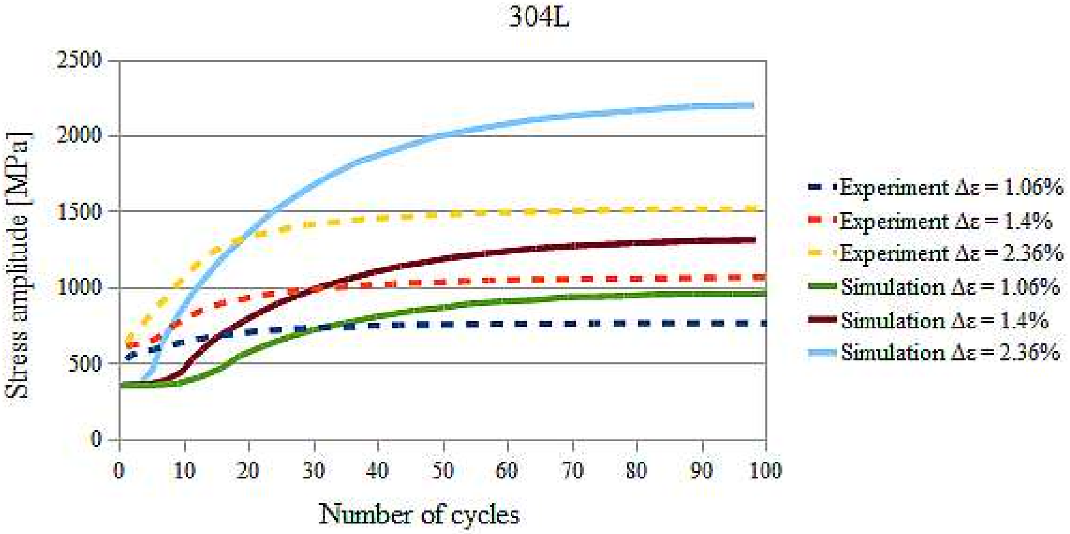

Figure 3.12: Comparison of experiments and numerical simulations for 304L steel under cyclic loading.

It should be highlighted here that the above presented results of cyclic loadings cannot be compared quantitatively to the experiments but only qualitatively due to the fact that full identification of parameters was not possible for currently available experimental data.

4. BENDING OF PRISMATIC BEAMS

4.1. Functionally graded structural members obtained by bending of beams

Bending of beams made of austenitic stainless steels at cryogenic temperatures may lead to creation of functionally graded structural members due to the plastic strain-induced phase transformation. One can initiate the transformation in external parts of cross-section by imposing kinematically controlled loading in the plastic range. Then, pre-bent structural members are composed of several layers: the elastic layer close to the neutral surface, the plastic layer located further away and the two-phase ($\gamma+\alpha'$) reinforced layer located at the top and bottom surfaces of the beam. The transition between layers is gradual and smooth, which eliminates the problem of stress concentrations between layers and possibilities of delamination. What is even more important, the strain-induced phase transformation is an irreversible process and the two-phase microstructure does not change after heating up to room temperature.

The constitutive model of materials undergoing the plastic strain-induced martensitic transformation is used in this chapter to form the set of equations describing behaviour of beams subjected to bending at cryogenic temperatures.

4.2. Elastic-plastic bending with $\gamma\rightarrow\alpha'$ phase transformation

Constitutive equations related to bending of beams in the elastic-plastic range with $\gamma\rightarrow\alpha'$ phase transformation are formulated analogically to 1D case presented in *Chapter 3*. Bending of a prismatic beam can be separated into compression in one part of the cross-section and tension in the other part and the border between these two processes is placed in the neutral plane of the beam. Thus, in the case of pure bending, one can consider only one part of the cross-section and assume that the constitutive equations for the other part are the same but with opposite sign. In the rectangular cross-section the three domains, arranged symmetrically with respect to the neutral axis, can be distinguished: elastic zone, plastic zone with linear hardening and plastic zone with phase transformation (*Fig. 4.5*).

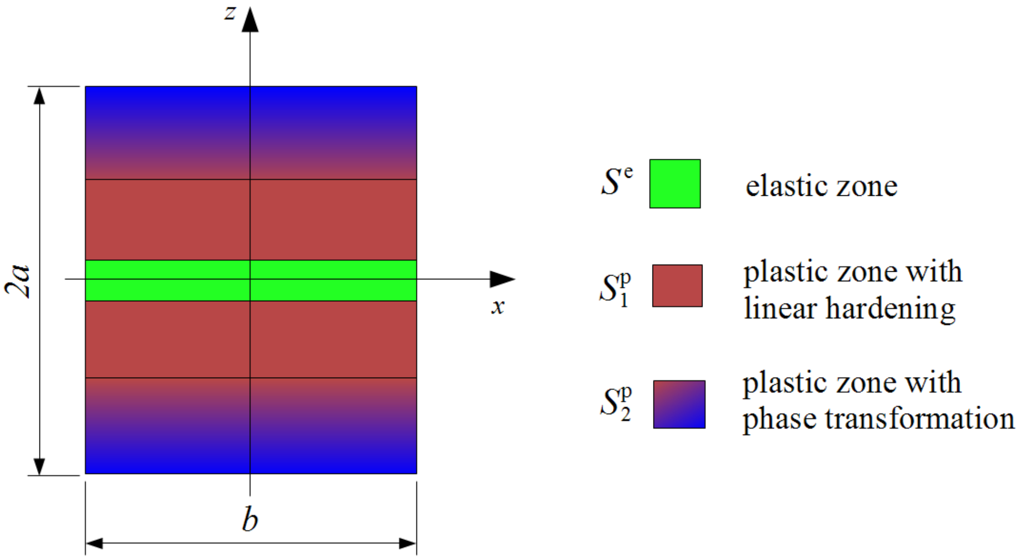

Figure 4.1: Cross-section of rectangular beam subjected to bending.

The stresses in the elastic zone, the plastic zone with linear hardening and the stress increments for plastic zone with phase transformation read:

$$\begin{gathered}\sigma^e = E\epsilon \quad \text{for} \quad \epsilon \leqslant \epsilon_0 \\ \sigma_1^p = \sigma_0 + C_0(\epsilon - \epsilon_0) \quad \text{for} \quad \epsilon_0 \leqslant \epsilon \leqslant \epsilon_\xi \\ \mathrm{d}\sigma_2^p = \mathrm{d}\sigma_{lin} + \mathrm{d}\sigma_{int} + \mathrm{d}\sigma_{a+m} = C_0\,\mathrm{d}\epsilon + C_0 h \xi\,\mathrm{d}\epsilon + C_{a+m}\,\mathrm{d}\epsilon \quad \text{for} \quad \epsilon \geqslant \epsilon_\xi\end{gathered} \tag{4.1}$$

where a direct formula for the current stress level in the phase transformation zone is obtained by integration of the incremental form of $\mathrm{d}\sigma_2^p$:

$$\sigma_2^p = \int_{\epsilon_\xi}^{\epsilon} C_0[1 + hA(\epsilon - \epsilon_\xi)]\,\mathrm{d}\epsilon + \int_{\epsilon_\xi}^{\epsilon} C_{a+m}(\epsilon)\,\mathrm{d}\epsilon \tag{4.2}$$

A simplified version of the homogenised stiffness modulus of two-phase material, derived in *Chapter 3*, is used:

$$C_{a+m}(\epsilon) = \frac{5C_0 A[1 + hA(\epsilon - \epsilon_\xi)](\epsilon - \epsilon_\xi)}{3[1 - A(\epsilon - \epsilon_\xi)]} \tag{4.3}$$

For the sake of simplicity, *Eq. 4.3* is expressed by means of constant coefficients:

$$C_{a+m} = \frac{A_1\epsilon^2 + A_2\epsilon + A_3}{A_4\epsilon + A_5} \tag{4.4}$$

where $A_1,\ldots, A_5$ are defined in the following form:

$$\begin{gathered}A_1=5A^2C_0h\\ A_2=5AC_0(1-2\mathrm{hA}\,\epsilon_\xi)\\ A_3=5AC_0\epsilon_\xi(hA\epsilon_\xi-1)\\ A_4=-3\mathrm{A}\\ A_5=3(1+A\epsilon_\xi)\end{gathered} \tag{4.5}$$

Finally the distribution of stresses as a function of strains during the phase transformation reads:

$$\sigma_2^p(\epsilon)=C_0\left[(\epsilon-\epsilon_\xi)+\frac{h}{2}A(\epsilon-\epsilon_\xi)^2\right]+B_1\epsilon^2B_2\epsilon+B_3\ln(A_4\epsilon+A_5)-B_4 \tag{4.6}$$

The value of bending moment in the beam is obtained by integrating the stresses, multiplied by the distance from the neutral axis *z*, over the cross-section area. The bending moment for the beam of rectangular cross-section of height *2a* and width *b* amounts to:

$$M=\iint\limits_A \sigma z\,dA=2b\int\limits_z \sigma z\,dz \tag{4.7}$$

In the case of elastic-plastic bending with the plastic strain-induced phase transformation, the stress is integrated over three domains, arranged symmetrically with respect to neutral axis: S^e denoting the elastic, central zone, S_1^p – the plastic zone with linear hardening and S_2^p – the plastic zone with martensitic transformation (*Fig. Error: Reference source not found*). Thus, the bending moment takes the form:

$$M=\iint\limits_{S^e}\sigma^e z\,\mathrm{d}\,S^e+\iint\limits_{S_1^p}\sigma_1^p z\,\mathrm{d}\,S_1^p+\iint\limits_{S_2^p}\sigma_2^p z\,\mathrm{d}\,S_2^p \tag{4.8}$$

A number of theories describe kinematics of bending beams. The simplest one, known as Bernoulli hypothesis, assumes that cross-sections that are plane and perpendicular to the beam axis before deformation remain plain and perpendicular to the beam axis after deformation and shear deformation of the cross-section is not considered. This theory was improved by Timoshenko by adding a term accounting for the shear deformation and the effect of rotational inertia. The Timoshenko theory is used to describe mostly short beams, where the shear influence is significant, or the so called sandwich composite beams. Another approach that has to be mentioned is the sandwich beam theory, derived initially for bending beams composed of three layers: a core which is subjected to transverse shear deformation and two facings that are subjected to stretching and bending action and deform according to the Bernoulli theory. The sandwich theory assumes that the core and facings are visibly separated from each other.

None of these theories was developed in view of kinematics of a beam with gradually changing material properties subjected to bending. The Bernoulli hypothesis of plane cross-sections is applied here due to its simplicity, which allows us to derive the analytical formulas for bending moment. It implies the fact that elongations and contractions of longitudinal fibres are proportional to the distance from the neutral axis. Accordingly, the following linear relation between the axial strain ϵ, the curvature of neutral axis κ and the current coordinate *z* is derived:

$$\epsilon = \kappa z \tag{4.9}$$

The bending moment in the elastic range is expressed as a function of curvature:

$$M^e(\kappa) = 2b\int_0^a E\epsilon z\, dz = 2b\int_0^a E\kappa z^2 dz \tag{4.10}$$

When the plastic deformation starts (before the phase transformation is activated) the bending moment is expressed by means of two terms, integrated over the elastic and the elastic-plastic zones, respectively:

$$M_1^p(\kappa) = 2b\int_0^{z_{el}(\kappa)} E\kappa z^2 dz + 2b\int_{z_{el}(\kappa)}^{a} \left[\sigma_0 + C_0(\kappa z - \epsilon_0)\right] z\, dz \tag{4.11}$$

As soon as the phase transformation starts, obtaining the value of bending moment requires integration over three zones: elastic, elastic-plastic with linear hardening and elastic-plastic with phase transformation:

$$\begin{gathered} M_2^p(\kappa) = 2b\int_0^{z_{el}(\kappa)} E\kappa z^2 dz + 2b\int_{z_{el}(\kappa)}^{z_{pl}(\kappa)} \left[\sigma_0 + C_0(\kappa z - \epsilon_0)\right] z\, dz + \\ + 2b\int_{z_{pl}(\kappa)}^{a} \left[\sigma_\xi + \sigma_{lin} + \sigma_{a+m}\right] z\, dz \end{gathered} \tag{4.12}$$

Finally, taking into account components of the bending moment for all zones, the relationship between the bending moment and curvature of bending beam is described by the equation:

$$\begin{gathered} M(\kappa) = 2\mathrm{B}\left\{\int_0^{z^e(\kappa)} E\kappa z^2 \mathrm{d}\, z + \int_{z^e(\kappa)}^{z_1^p(\kappa)} z[\sigma_0 + C_0(\kappa z - \epsilon_0)] dz\right\} + \\ + 2\mathrm{B}\left\{\int_{z_1^p(\kappa)}^{\frac{H}{2}} z\left[\sigma_\xi + C_0(\kappa z - \epsilon_\xi) + \frac{h}{2} A C_0(\kappa z - \epsilon_\xi)^2\right] \mathrm{d}\, z\right\} + \\ + 2\mathrm{B}\left\{\int_{z_1^p(\kappa)}^{\frac{H}{2}} z[B_1\kappa^2 z^2 + B_2\kappa z + B_3 \ln(A_4\kappa z + A_5) - B_4] \mathrm{d}\, z\right\} \end{gathered} \tag{4.13}$$

where $B_1,\ldots, B_5$ are constant coefficients:

$$\begin{gathered} B_1 = \frac{A_1}{2A_4} \\ B_2 = \frac{A_2 A_4 - A_1 A_5}{A_4^2} \\ B_3 = \frac{A_3 A_4^2 - A_2 A_4 A_5 + A_1 A_5^2}{A_4^3} \\ B_4 = B_1 \epsilon_\xi^2 + B_2 \epsilon_\xi + B_3 \ln(A_4 \epsilon_\xi + A_5) \end{gathered} \tag{4.14}$$

The bending moment as a function of curvature for rectangular beam with the plastic strain-induced phase transformation is shown in *Fig.4.2*.

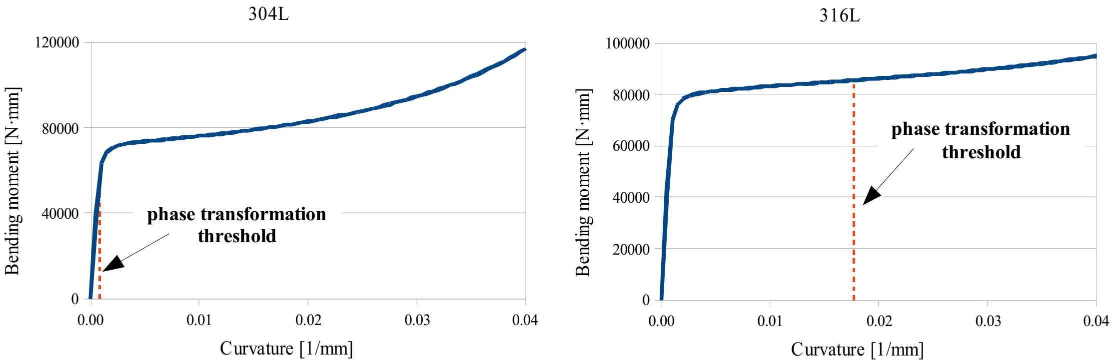

Figure 4.2: Bending moment as a function of curvature for 304L and 316L stainless steel.

The distribution of the volume fraction of martensite evolves along the height of the cross-section, creating symmetrically located layers (*Fig. 4.3*).

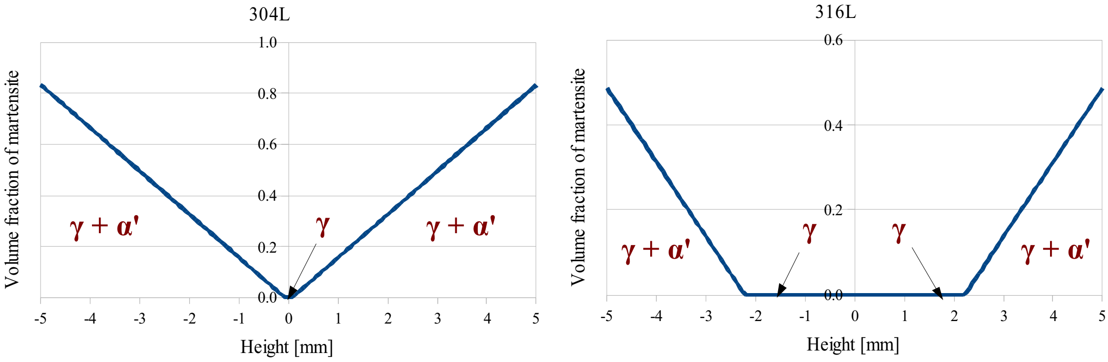

Figure 4.3: Martensite content as a function of beam height.

4.3. Numerical examples of beams with γ→α' phase transformation subjected to bending

Rectangular beams made of 316L stainless steel, subjected to bending at 77 K are considered. Numerical analyses using the USERPL procedure, that takes into account the influence of γ→α' phase transformation on the material behaviour, were prepared for two load cases:

a) cantilever beam of rectangular cross-section subjected to constant bending moment (*Fig. 4.4a*);

b) simply supported beam of rectangular cross-section loaded symmetrically with two concentrated forces (*Fig. 4.4b*).

The following dimensions are assumed: length $L = 10\ cm$, height $2a = 10\ mm$, width $b = 5\ mm$.

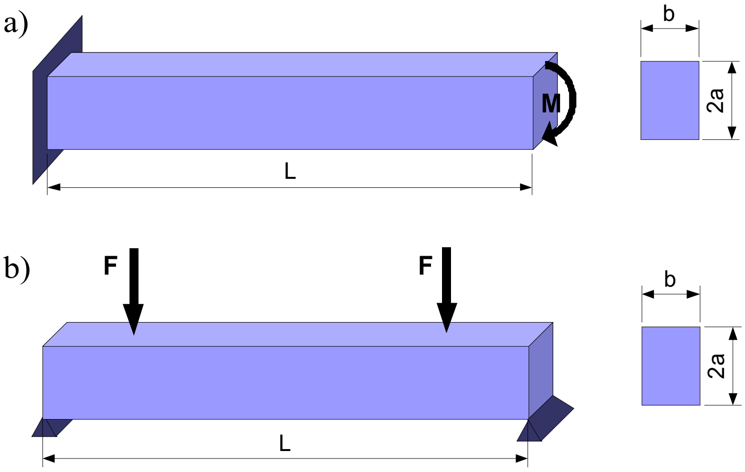

Figure 4.4: Load cases: a) constant bending moment; b) two concentrated forces.

The beams are modelled by means of PLANE42 elements. Using options available for this element, one can solve the case of beam subjected to bending assuming the plane stress state. This assumption enables us to use a relatively dense finite element mesh, which reduces the analysis run-time.

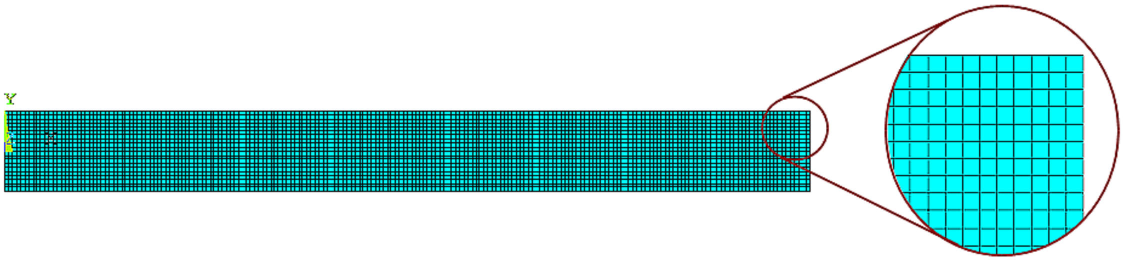

Figure 4.5: Finite element mesh of a beam subjected to bending.

Analysis of the beam subjected to bending by means of constant bending moment shows how the layers with gradually changing microstructure are located. One can also observe non-linear distribution of stresses in the cross-section which results from the hardening caused by the presence of martensite (*Fig. 4.6*).

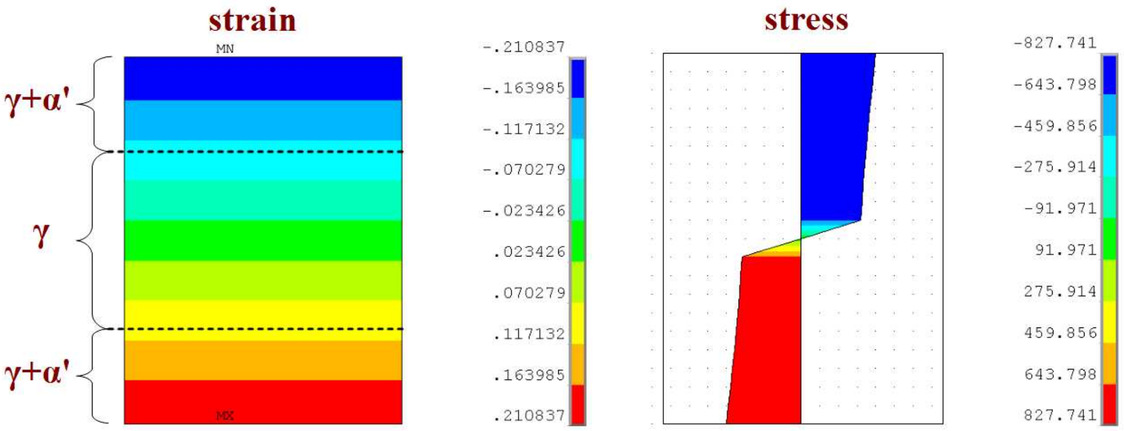

Figure 4.6: Strain and stress distributions in the cross-section of a beam.

Loading a simply supported beam with two concentrated forces leads to constant bending moment between the forces. This configuration can be easily applied in an experimental set-up in order to generate the functionally graded material structure. By cutting-off the end parts of the beam, one can obtain a beam with continuously changing properties in the cross-section, similar to a layered structure (*Fig. 4.7)*.

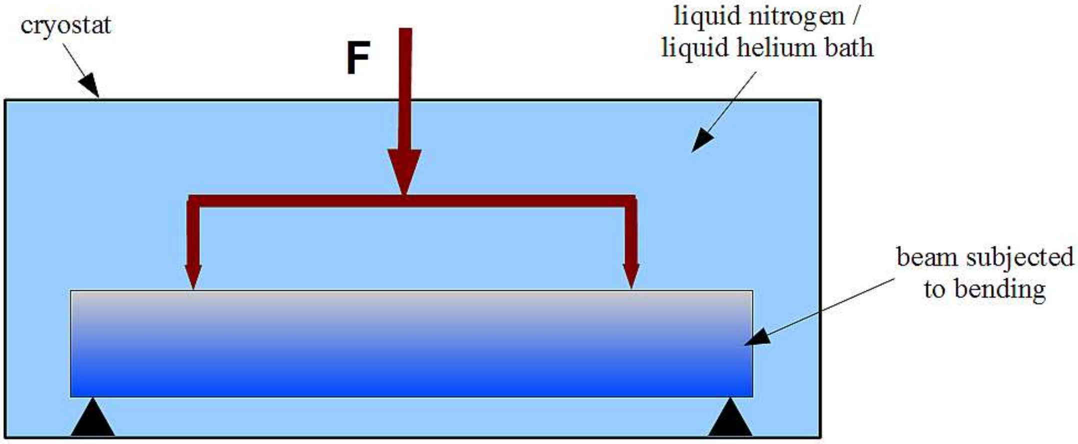

Figure 4.7: Creation of FGSM by by loading simply supported beam with two forces.

The numerical simulation of such a process is shown in *Fig. 4.8*. The presented distribution of strains is directly related to the distribution of α' phase (martensite) and represents the layered structure of the beam.

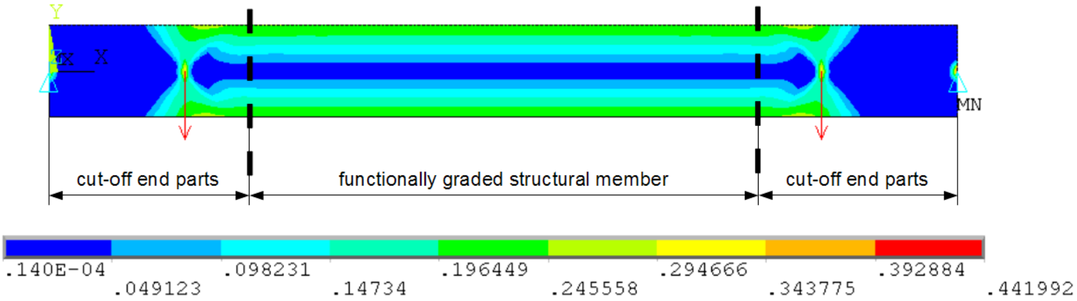

Figure 4.8: Numerical simulation of FGSM creation process.

4.4. Cyclic bending of rectangular beams

Cyclic bending of a simply supported beam subjected to two symmetrically applied forces is considered (*Fig. 4.9*). The dimensions and the finite element mesh are the same as for the monotonic bending.

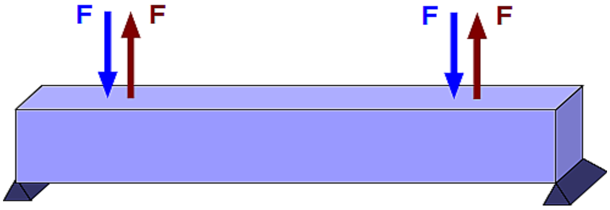

Figure 4.9: Rectangular beam subjected to cyclic loading.

The hysteresis loops for four different saturation levels of martensite in the material are shown in *Fig. 4.10*. When the phase transformation is not active, the linear hardening is present only. However, with the increasing amount of martensite in the material, its influence on the strain hardening becomes more and more visible. The size of the hysteresis loops decreases faster during cyclic loading of materials with higher martensite content. It can be interpreted by the fact, that the materials with higher content of martensite dissipate less energy (inclusions are assumed elastic).

The set of hysteresis loops for different saturation levels ξ_L of the phase transformation is shown in *Fig. 4.11*. Additionally, for the sake of comparison, the results for a material with $\xi_L = 0.9$ are presented. However, one should bear in mind that allowing for martensite content above 50% may not be correct in view of the applied homogenisation process.

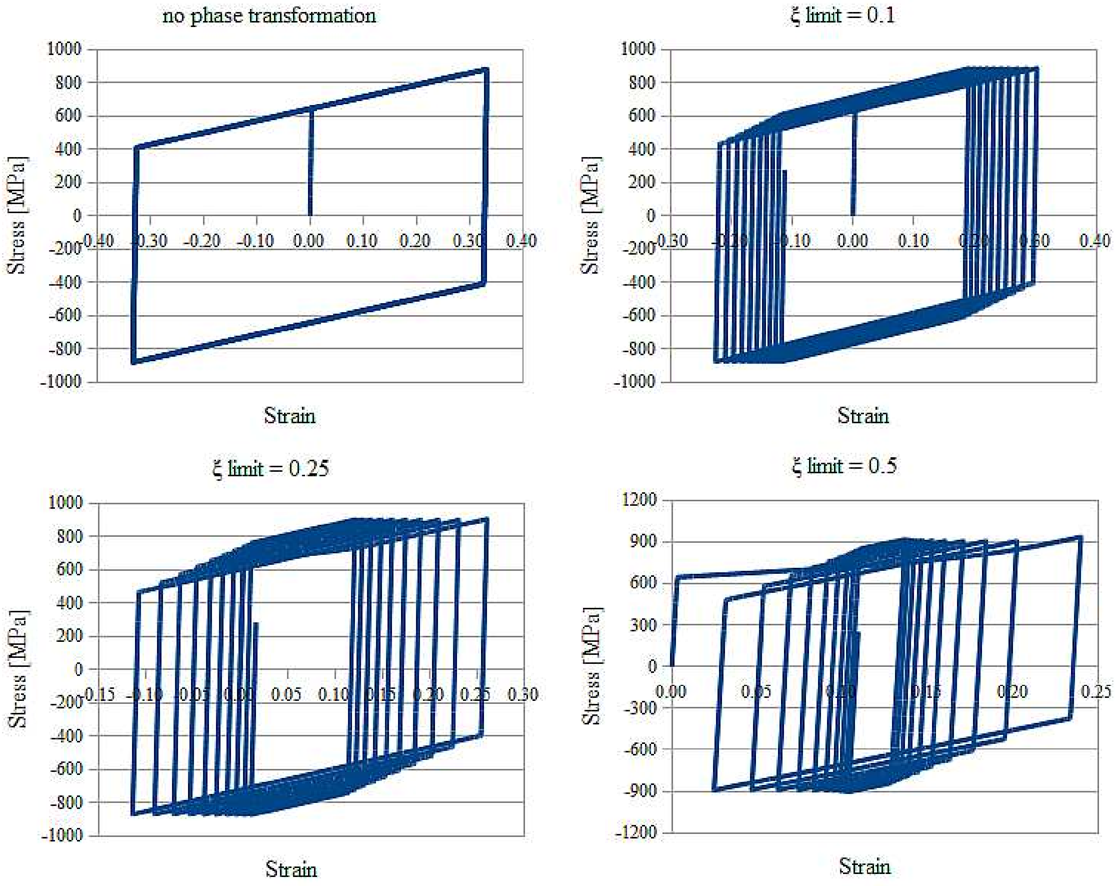

Figure 4.10: Stress - strain hysteresis loops for different phase transformation saturation levels ξ_L during cyclic bending.

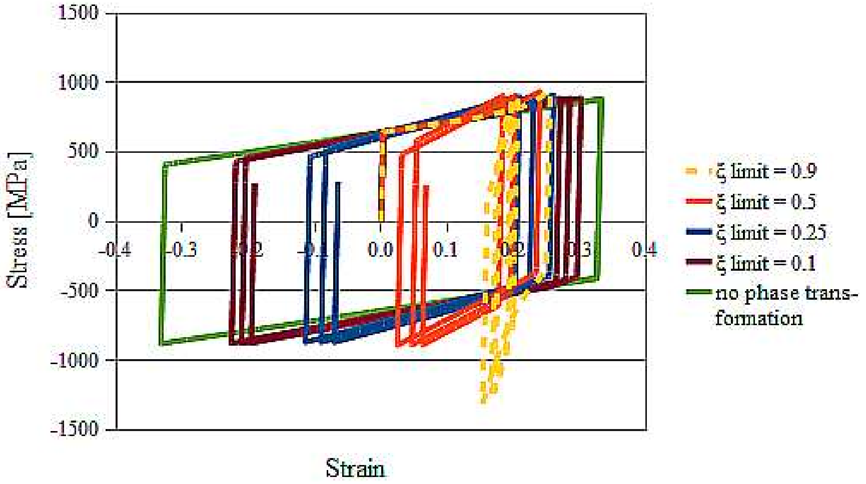

Figure 4.11: Comparison of hysteresis loops for different martensite content levels.

Analysis of the plastic strains distribution under cyclic loadings indicates that the process of alternating plasticity is accompanied by strong reduction of plastic strain amplitude in the presence of martensite (*Figs 4.12* and *4.1*). The bigger martensite content, the lower strain amplitudes are achieved for the same number of cycles.

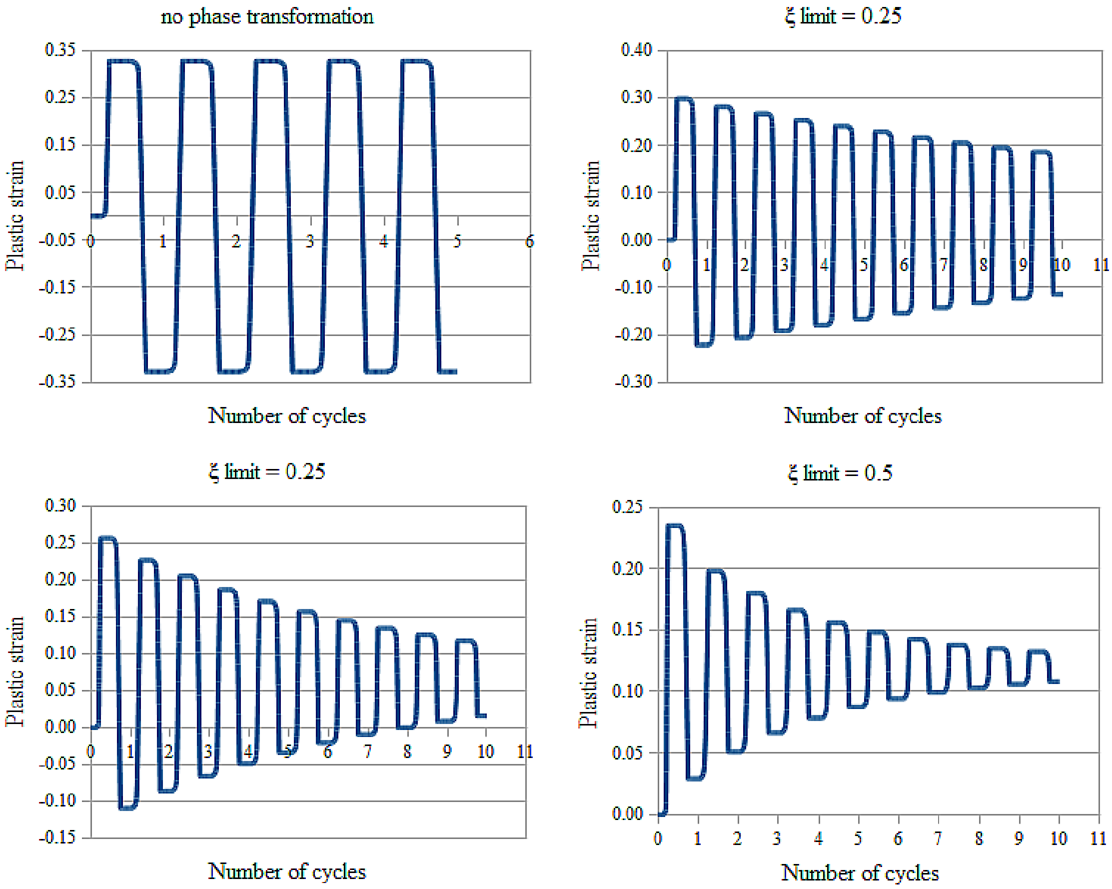

Figure 4.12: Evolution of plastic strain for different phase transformation saturation levels during cyclic bending.

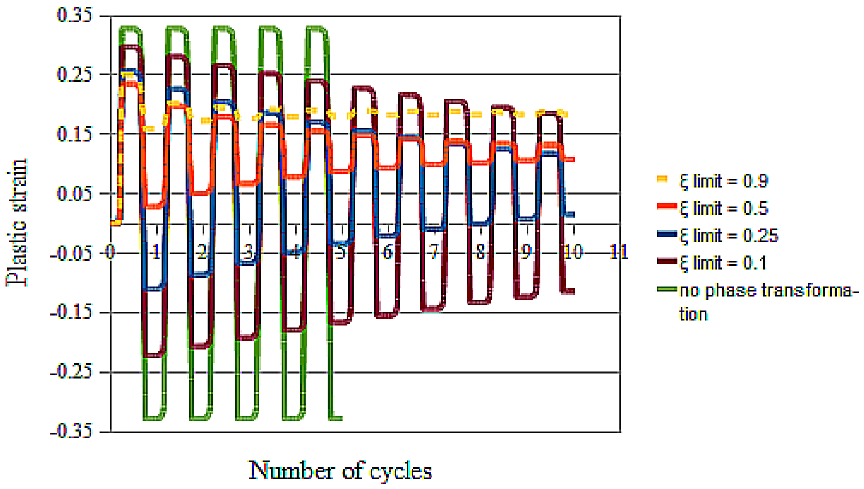

Figure 4.13: Comparison of plastic strain amplitudes for different martensite content levels.

The evolution of the accumulated plastic strain as a function of the number of cycles is shown in *Figs 4.14* and *4.15* . A material which does not undergo the phase transformation is characterised by linear increase of the accumulated plastic strain in the course of cycling. The presence of martensite manifests itself in reduction of the rate of increase of the accumulated plastic strain and the whole process takes the non-linear form.

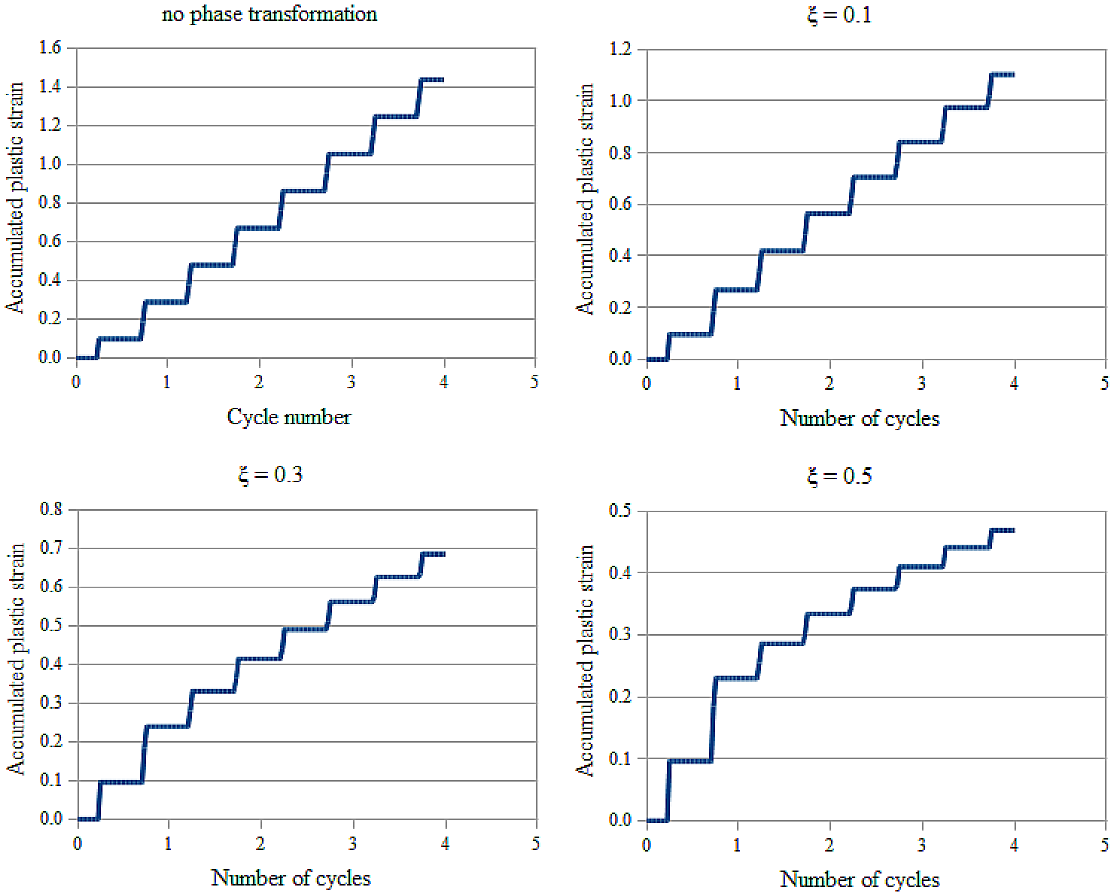

Figure 4.14: Evolution of the accumulated plastic strain for different phase transformation saturation levels during cyclic bending.

It is possible to estimate the relation between the martensite content and the accumulated plastic strain (*Fig. 4.16*). The power dependence can be observed here. The more martensite the smaller increase of the accumulated plastic strain.

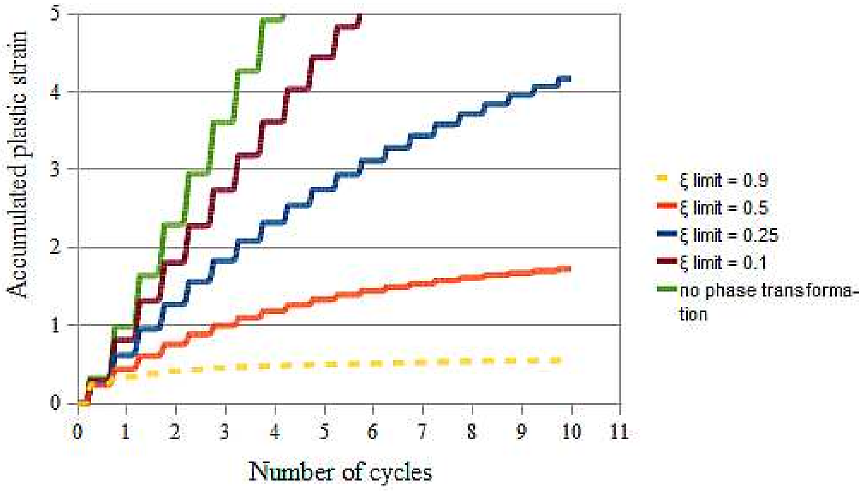

Figure 4.15: Comparison of the accumulated plastic strain distributions for different martensite content levels.

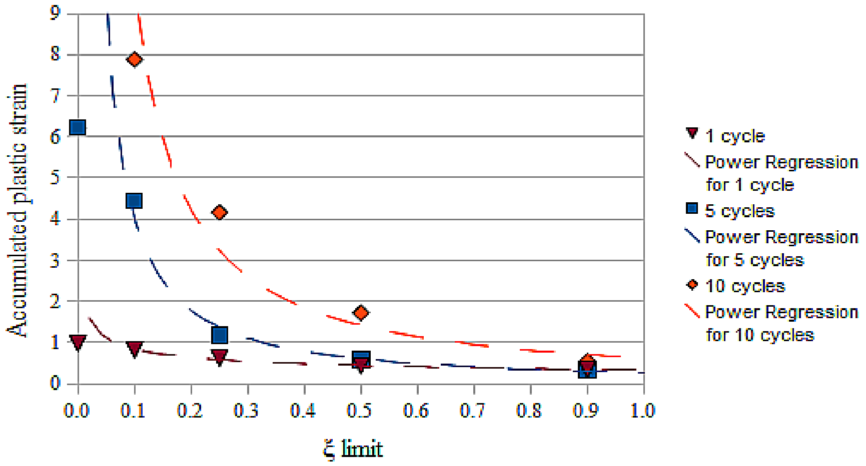

Figure 4.16: Estimated relationship between the accumulated plastic strain and the martensite content.

5. TORSION OF CIRCULAR RODS

5.1. Functionally graded structural members obtained by torsion of circular rods

Applying torque at cryogenic temperatures to circular rods made of metastable austenitic stainless steels may generate structures of radially varying mechanical properties. Based on the mechanism of plastic strain-induced phase transformation it is possible to create rods with elastic-plastic core surrounded by a hardened, two-phase layer consisting of the mixture of γ austenite and α' martensite.

The process of creating a rod with functionally graded properties can be realised by immersing the structural member in liquid helium or liquid nitrogen and twisting above the plastic strain threshold associated with the initiation of the phase transformation. Martensite created in the material during the strain-induced phase transformation is stable even after heating the structure up to room temperature due to the fact, that this transformation is irreversible.

5.2. Elastic-plastic torsion with γ→α' phase transformation

A bar of a circular cross-section, fixed at one end and twisted by a torque applied at the other extremity is analysed. In general, the torque M_t twisting a rod is equivalent to the sum of moments of internal forces with respect to the axis of the rod, which can be expressed in the form of integral over the cross-section area. In case of a rod of circular cross-section, the analytical expression for the torque in the polar coordinate system takes the form:

$$M_t = \iint_A \tau\, r\, dA = 2\pi \int_r \tau\, r^2\, dr \tag{5.1}$$

where τ is the shear stress, r is the radial coordinate and A denotes the cross-section area.

It is assumed that the shear strain γ can be expressed as a linear function of the unit angle of twist θ and radius r:

$$\gamma=\theta r \tag{5.2}$$

In the case of elastic-plastic torsion of a circular rod undergoing the martensitic phase transformation one can distinguish three zones, located concentrically with respect to the axis of the rod: S^e – elastic zone, S_1^p – plastic zone of austenitic structure without phase transformation and S_2^p – plastic zone undergoing the phase transformation and consisting of austenite and martensite (*Fig. 5.1*). The constitutive equations describing behaviour of material in these three domains are built on the basis of general model presented in *Chapter 2* and converted to the case of pure shear.

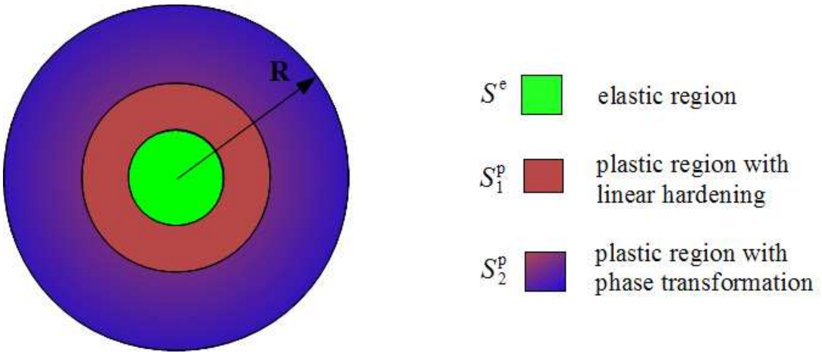

Figure 5.1: Cross-section of circular rod subjected to torsion.

In the elastic range, the shear stress is related to the shear strain according to the Hook's law:

$$\tau^e=G\gamma \quad \text{for} \quad \gamma\leqslant\gamma_0 \tag{5.3}$$

where G is the shear modulus and γ_0 represents the plastic strain threshold.

According to *Eq. 5.1*, the torque as a function of the unit angle of twist for the elastic range takes the following form:

$$M^e(\theta)=2\pi G\int_0^R \gamma r^2\,dr=2\pi G\int_0^R \theta r^3\,dr \tag{5.4}$$

As soon as the yield stress is achieved, the plastic deformations start to appear on the outer surface of the rod. The shear stress in the plastic range with linear hardening is expressed as:

$$\tau_1^p=\tau_0+C_0(\gamma-\gamma_0) \quad \text{for} \quad \gamma_0\leqslant\gamma\leqslant\gamma_\xi \tag{5.5}$$

where γ_ξ represents the phase transformation shear strain threshold.

The value of torque in the elastic-plastic region before the phase transformation starts is obtained by integrating the relevant stresses over the elastic ($0\leqslant r\leqslant r_{el}$) and the plastic ($r_{el} \leqslant r \leqslant R$) domains respectively:

$$M_1^p(\theta)=2\pi\int_0^{r_{el}(\theta)} G\,\theta r^3 dr+2\pi\int_{r_{el}(\theta)}^{R}\left[\tau_0+C_0(\theta r-\gamma_0)\right]r^2 dr \tag{5.6}$$

The stress increment in the elastic-plastic region during the phase transformation is composed of the terms related to the shear stress increments due to the linear hardening $d\tau_{lin}$, the interaction of dislocations with martensitic inclusions $d\tau_{int}$ and the homogenisation of two-phase structure $d\tau_{a+m}$:

$$d\tau_2^p=d\tau_{lin}+d\tau_{int}+d\tau_{a+m}=C_0 d\gamma+C_0 h\xi d\gamma+C_{a+m}d\gamma \tag{5.7}$$

The linearised kinetic law of the phase transformation defines the volume fraction of martensite as a function of shear strain as:

$$\xi(\gamma)=\int_{\gamma_\xi}^{\gamma} A\,d\gamma=A(\gamma-\gamma_\xi) \tag{5.8}$$

Substituting this to *Eq. 5.8* and integrating from the phase transformation shear strain threshold to the current shear strain, one obtains the stress value as:

$$\tau_2^p=\int_{\gamma_\xi}^{\gamma} C_0[1+hA(\gamma-\gamma_\xi)]\,d\gamma+\int_{\gamma_\xi}^{\gamma} C_{a+m}(\gamma)\,d\gamma \tag{5.9}$$

C_{a+m} is the simplified version of the homogenised stiffness modulus expressed as:

$$C_{a+m}=\frac{A_1\left(\frac{\gamma}{2}\right)^2+A_2\frac{\gamma}{2}+A_3}{A_4\frac{\gamma}{2}+A_5} \tag{5.10}$$

where $A_1,\ldots,A_5$ are constant coefficients defined as:

$$\begin{gathered}A_1=5A^2C_0h\\ A_2=5AC_0(1-2\mathrm{hA}\,\epsilon_\xi)\\ A_3=5AC_0\epsilon_\xi(hA\epsilon_\xi-1)\\ A_4=-3\mathrm{A}\\ A_5=3(1+A\epsilon_\xi)\end{gathered} \tag{5.11}$$

The final expression for stress in the range of phase transformation is:

$$\tau_2^p(\gamma)=C_0\left[(\gamma-\gamma_\xi)+\frac{h}{2}A(\gamma-\gamma_\xi)^2\right]+B_1\left(\frac{\gamma}{2}\right)^2 B_2\frac{\gamma}{2}+B_3\ln(A_4\frac{\gamma}{2}+A_5)-B_4 \tag{5.12}$$

where $B_1,\ldots,B_5$ are constant coefficients equal to:

$$\begin{gathered} B_1=\frac{A_1}{2A_4} \\ B_2=\frac{A_2A_4-A_1A_5}{A_4^2} \\ B_3=\frac{A_3A_4^2-A_2A_4A_5+A_1A_5^2}{A_4^3} \\ B_4=B_1\epsilon_\xi^2+B_2\epsilon_\xi+B_3\ln\left(A_4\epsilon_\xi+A_5\right) \end{gathered} \tag{5.13}$$

Calculation of the torque value in the case of plastic strain-induced phase transformation process requires integrating the stresses over the elastic zone ($0\leqslant r\leqslant r_{el}$), the elastic-plastic zone with linear hardening ($r_{el}\leqslant r\leqslant r_\xi$) and the elastic-plastic zone with the phase transformation ($r_\xi\leqslant r\leqslant R$).

$$\begin{aligned} M_2^p(\theta)=2\pi\int_0^{r_{el}(\theta)}G\theta r^3dr+2\pi\int_{r_{el}(\theta)}^{r_\xi(\theta)}\left[\tau_0+C_0(\theta r-\gamma_0)\right]r^2dr+ \\ +2\pi\int_{r_\xi(\theta)}^{R}\tau_\xi C_0\left[(\theta r-\gamma_\xi)+\frac{h}{2}A(\theta r-\gamma_\xi)^2\right]r^2dr+ \\ +2\pi\int_{r_\xi(\theta)}^{R}\left[B_1\left(\frac{\theta r}{2}\right)^2B_2\frac{\theta r}{2}+B_3\ln\left(A_4\frac{\theta r}{2}+A_5\right)-B_4\right]r^2dr \end{aligned} \tag{5.14}$$

The torque as a function of unit angle of twist with three characteristic domains is presented in *Fig. 5.2*. In the case of a bar made of 304L stainless steel the phase transformation starts almost immediately after reaching the yield point, which makes the linear hardening process relatively narrow and leads to significant non-linear hardening of material.

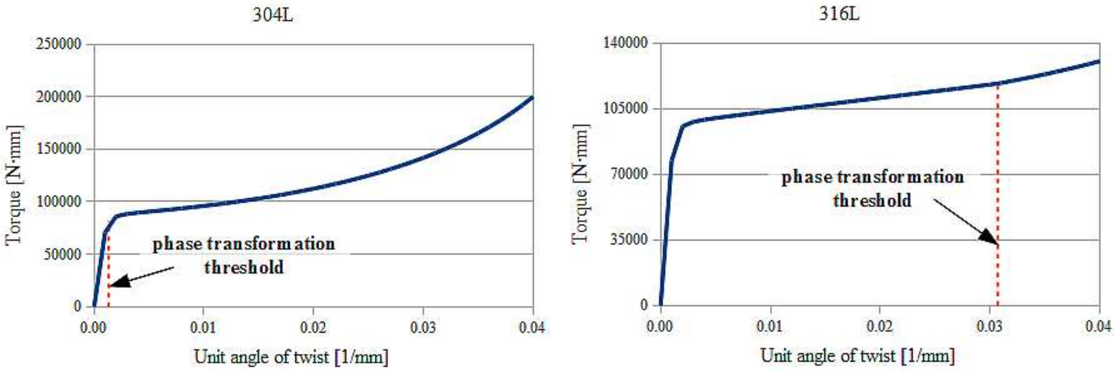

Figure 5.2: Torque as a function of unit angle of twist.

The volume fraction of martensite evolves along the radius generating the functionally graded structure and radially varying mechanical properties of the rod (*Fig. 5.3*). Martensite is created in the outer layer of the rod, what strengthens its surface with simultaneous preservation of the elastic-plastic properties of the core.

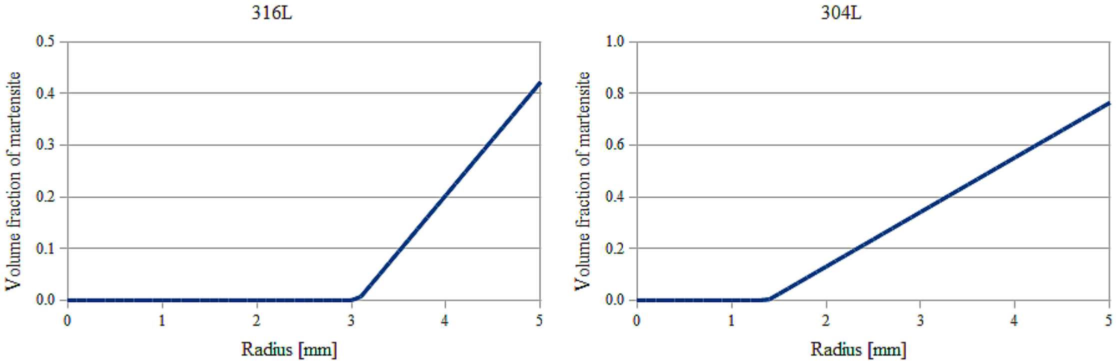

Figure 5.3: Martensite content as a function of radius.

5.3. Numerical examples of rods with γ→α' phase transformation subjected to torsion

Circular rods made of 316L stainless steel and subjected to torsion at 77 K are selected as examples for numerical analysis of structural members with functionally graded properties. The solid rod has radius $R = 5mm$ whereas the annular rod is characterised by the outer radius $R_{out} = 5mm$ and the inner radius $r = 2.5mm$. The loads are applied according to the scheme shown in *Fig. 5.4 a, b*.

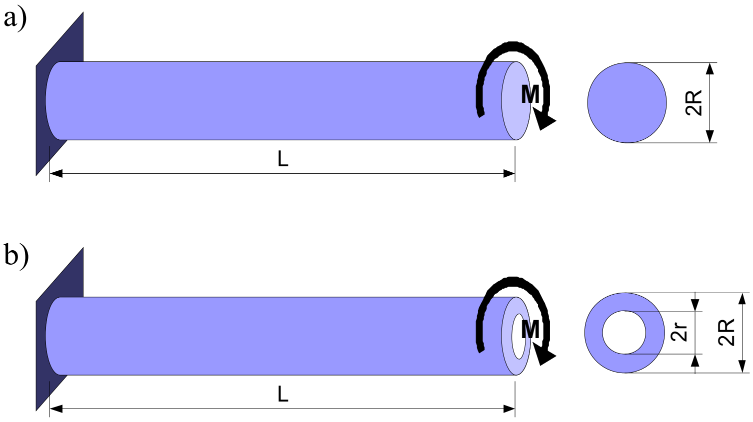

Figure 5.4: Load cases: a) torsion of a solid rod and b) torsion of a hollow rod.

The rods are modelled by means of SOLID45 elements. In order to reduce the size of the model and obtain reliable results, the finite element mesh is denser in the middle of the rod length, in the place where the results are red out (*Fig. 5.5*).

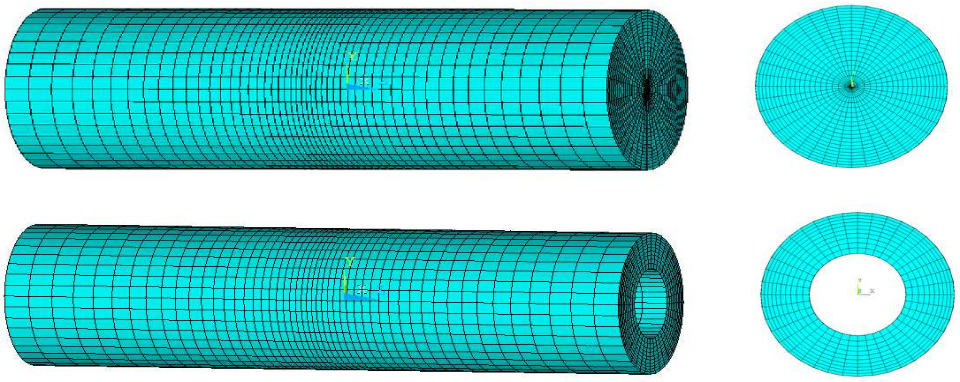

Figure 5.5: Finite element mesh in rods subjected to torsion.

The stress and the strain distributions for both cases are presented in *Figs 5.6* and *5.7*. In the central part of the solid rod one can distinguish the region without phase transformation, where only γ phase is present. The region with the phase transformation, where both γ austenite and α' martensite are present, is created on the outer surface of the rod. In the case of annular rod the whole cross-section contains martensitic inclusions, however the distribution of martensite changes gradually along the radius of the rod.

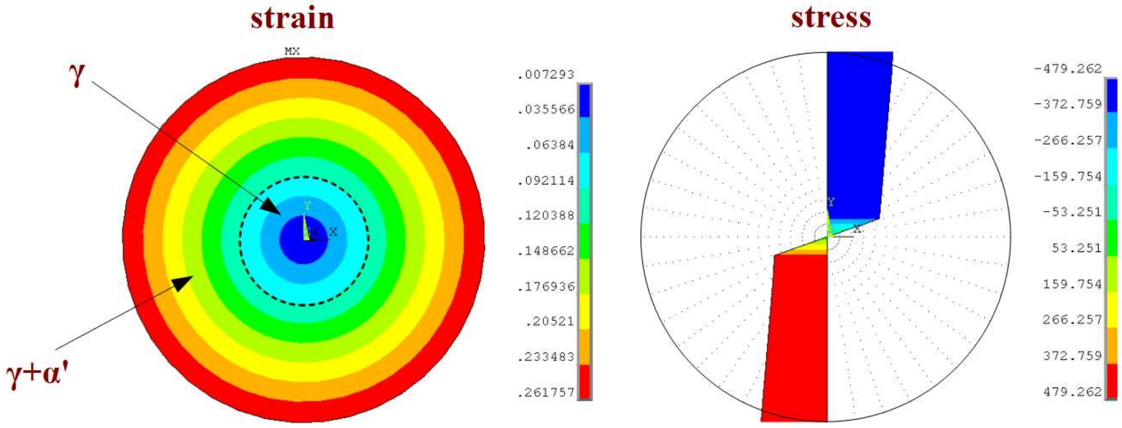

Figure 5.6: Strain and stress distributions in the cross-section of a solid rod subjected to torsion.

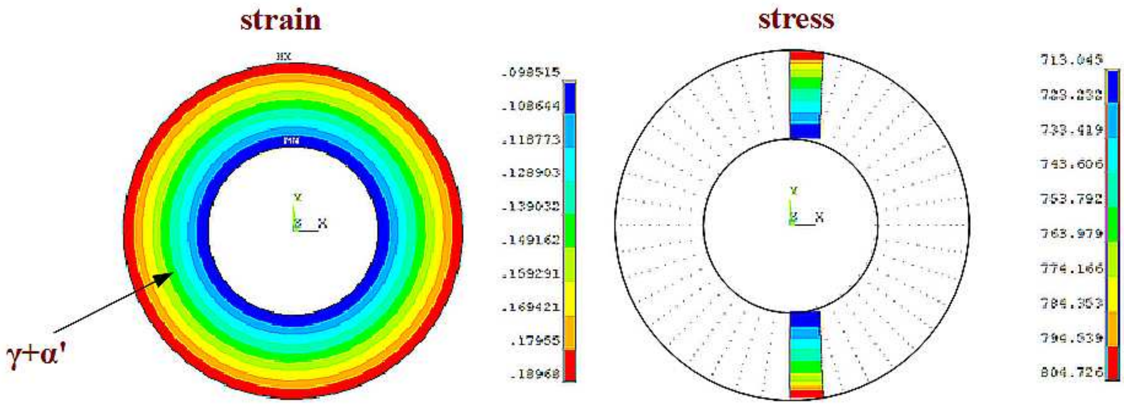

Figure 5.7: Strain and stress distributions in the cross-section of a hollow rod subjected to torsion.

5.4. Cyclic torsion of thin-walled cylinders (tubes)

A thin-walled cylinder (tube) made of 316L stainless steel is subjected to cyclic torsion at the liquid nitrogen temperature. The outer radius of the cylinder is $R = 5mm$ and the thickness $t = 0.5mm$. In order to investigate how the martensite content affects on the behaviour of the material subjected to cyclic loadings, it is assumed that the saturation level of the phase transformation may be adjusted. The finite element model has been built by using SOLID45 elements and the boundary conditions are set as shown in *Fig. 5.8*.

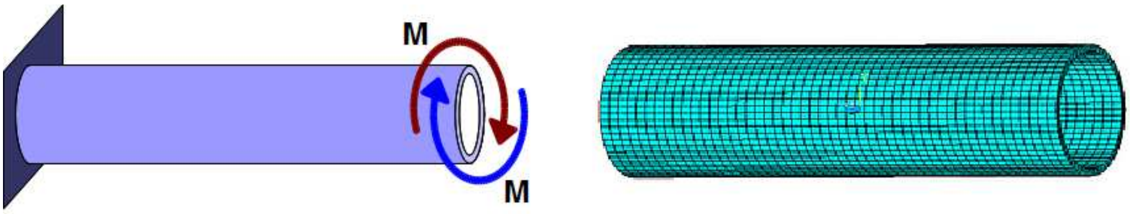

Figure 5.8: Boundary conditions and finite element mesh of thin-walled cylinder subjected to cyclic torsion.

The comparison of hysteresis loops for different saturation levels of the martensitic transformation is presented in *Figs 5.9* and *5.10*. Similarly like in the bending case, one can observe that the size of the hysteresis loops decrease with increasing amount of martensite in the material.

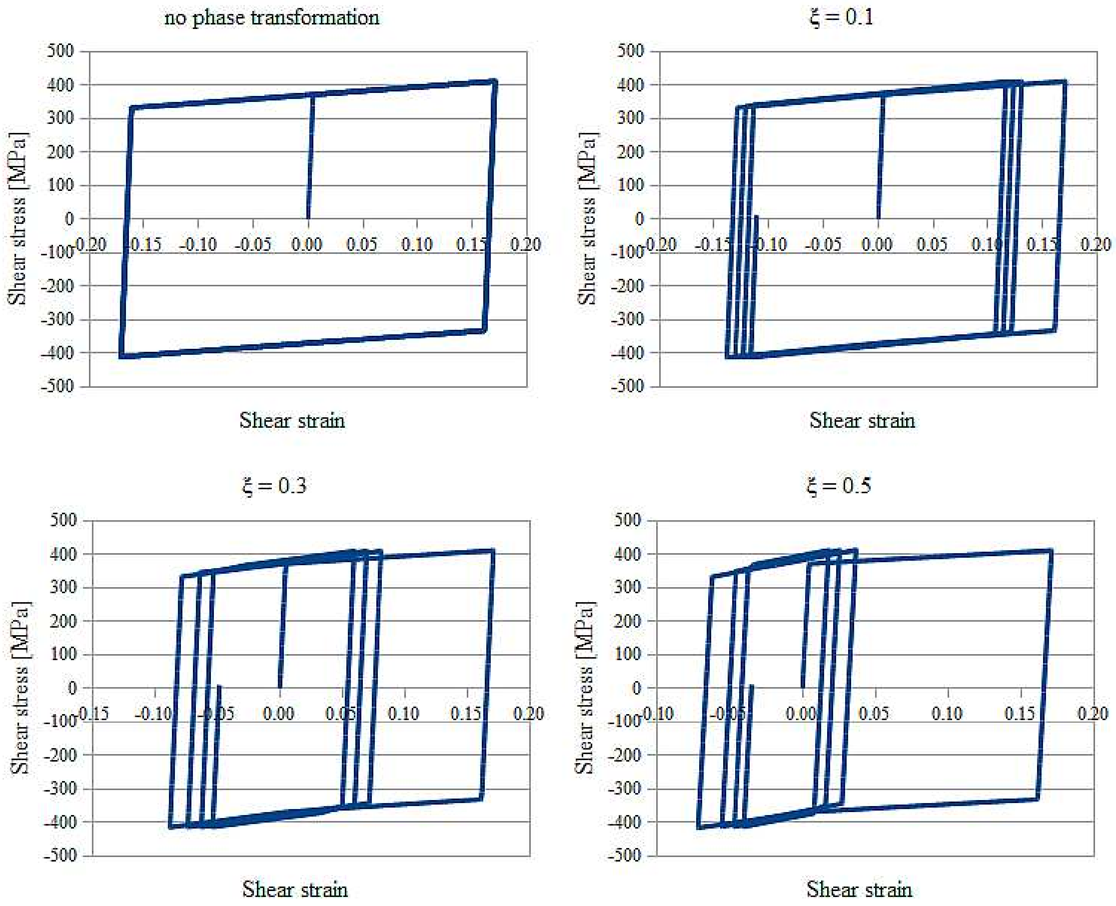

Figure 5.9: *Stress - strain hysteresis loops for different phase transformation saturation levels during cyclic torsion.*

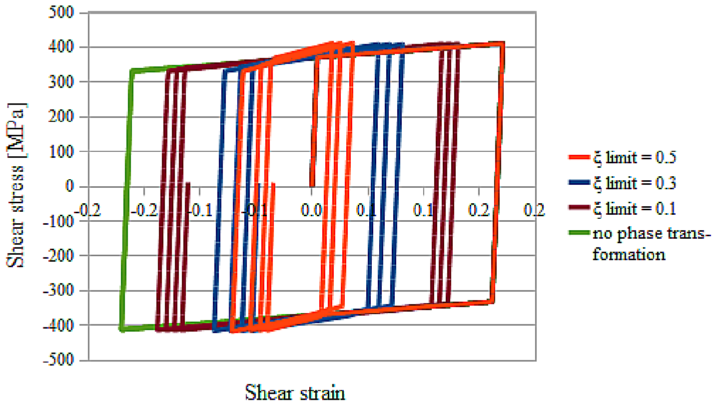

Figure 5.10: *Comparison of hysteresis loops for different phase transformation saturation levels during cyclic torsion.*

Initially, the plastic strain range reduces from cycle to cycle. However, it stabilises very quickly and remains with constant plastic strain amplitude. This effect is more visible for materials with bigger saturation level of the phase transformation (*Figs 5.11* and *5.12*).

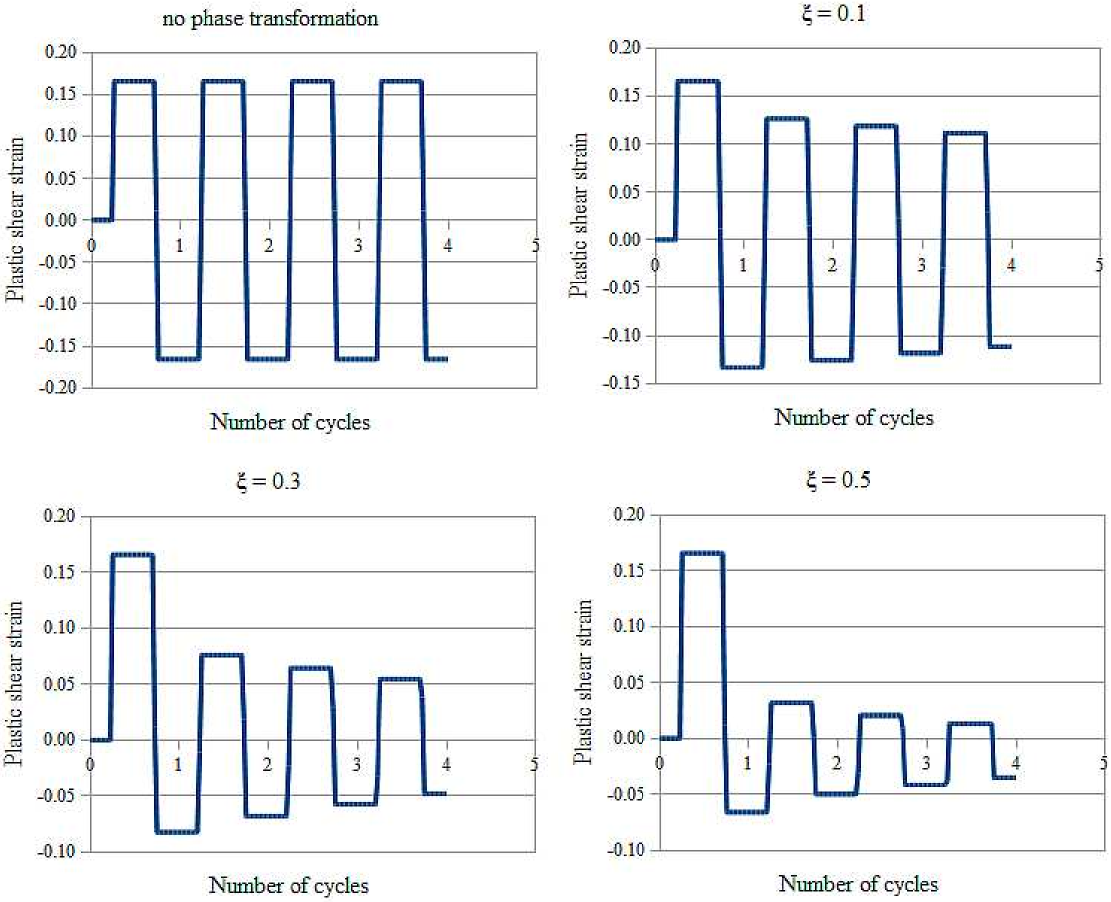

Figure 5.11: Evolution of plastic shear strain for different phase transformation saturation levels during cyclic torsion.

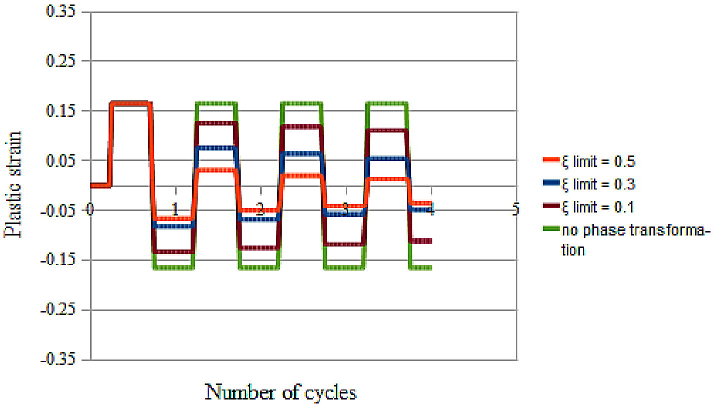

Figure 5.12: Comparison of stabilized plastic strain amplitudes for different martensite content levels.

The biggest increase of the accumulated plastic strain is observed for the materials without phase transformation (*Figs 5.13* and *5.14*). The presence of martensite reduces significantly the amount of plastic work dissipated in the material.

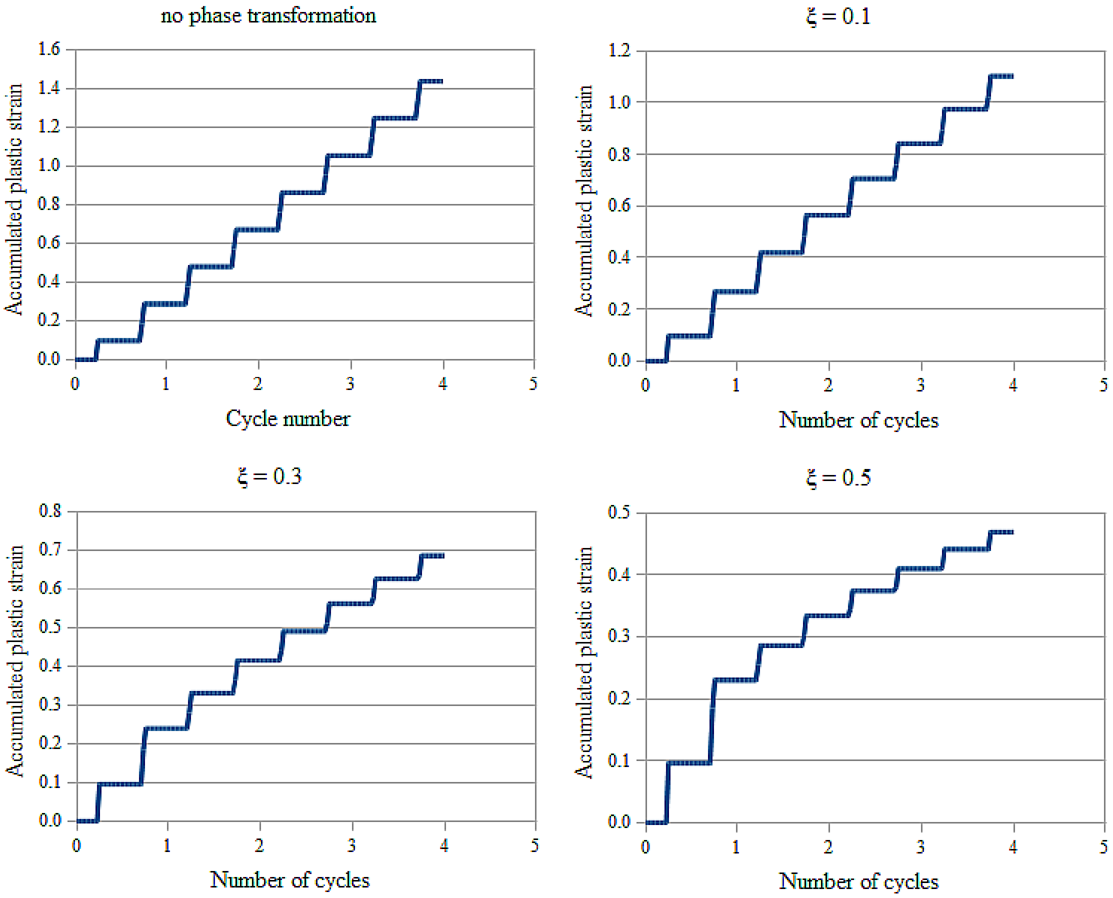

Figure 5.13: Evolution of the accumulated plastic strain for different phase transformation saturation levels during cyclic torsion.

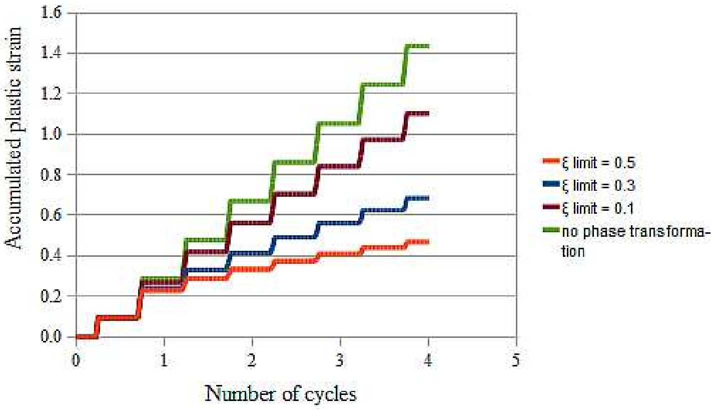

Figure 5.14: Comparison of the accumulated plastic strain for different martensite content levels.

6. FUNCTIONALLY GRADED STRUCTURAL MEMBERS SUBJECTED TO COMBINED LOADINGS

6.1. Combined loadings applied to structures undergoing phase transformation

In this chapter, the FE simulations of nonproportional loading paths applied to thin-walled cylinders undergoing the strain-induced phase transformation are carried out. Two distinct numerical analyses consisting of four loading cycles were performed:

- uniaxial tension (first cycle) combined with three cycles of oscillating torsion (cycles 2 - 4)
- torsion (first cycle) combined with three cycles of tension and compression (cycles 2 - 4)

The cylinder of length $L = 70mm$ has outer radius of $R = 5mm$ and the thickness $t = 0.5mm$. The finite element model was built by means of 3D SOLID45 elements (*Fig. 6.1*). All results are extracted from the element lying at the outer surface of the cylinder in the middle of its length in order to reduce the influence of the applied boundary conditions.

First cycle is understood here as a monotonic loading up to the assumed load level (sustained load), followed by further cycling with respect to the complementary stress component. For instance, monotonic tensile load which is followed by cyclic torsion.

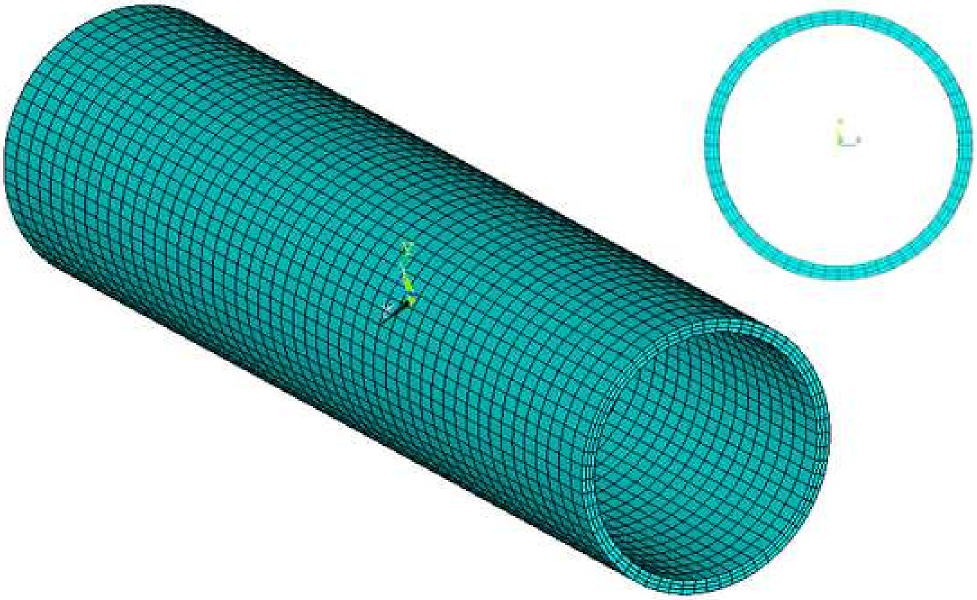

Figure 6.1: Finite element mesh of thin-walled cylinder subjected to combined load.

6.2. Case 1: tension with cyclic torsion

Thin-walled cylinder subjected to uniaxial tension and then to cyclic torsion is considered (*Fig. 6.2*).

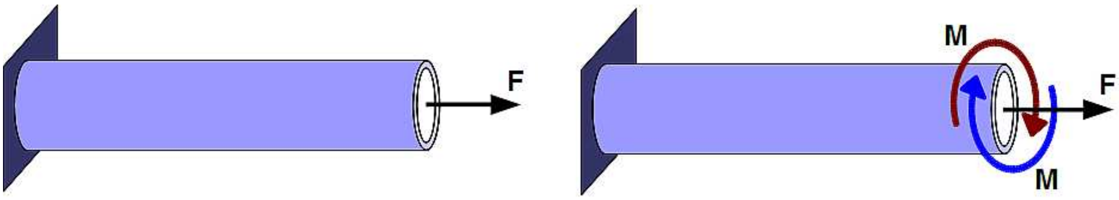

Figure 6.2: Thin-walled cylinder subjected to tension and cyclic torsion.

The load values are chosen in such a way that during tension the equivalent strain reaches the level which assures initiation of the plastic strain-induced phase transformation and, subsequently, during cyclic torsion the equivalent strains stay below the value of 0.2. The loading path in the stress space is shown in *Fig. 6.3.*

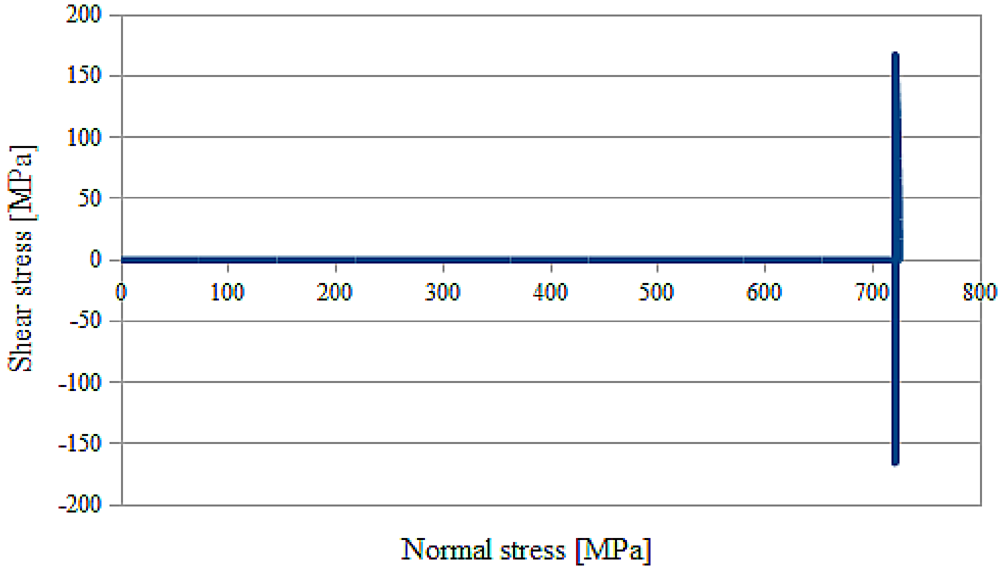

Figure 6.3: Loading trajectory in the stress space for uniaxial tension and cyclic torsion.

Distribution of the equivalent stress as a function of the equivalent strain resulting from the calculations is shown in *Fig. 6.4*. One can observe that the dissipation of energy – characteristic of cyclic loading of plastic material – is not present starting from the third cycle.

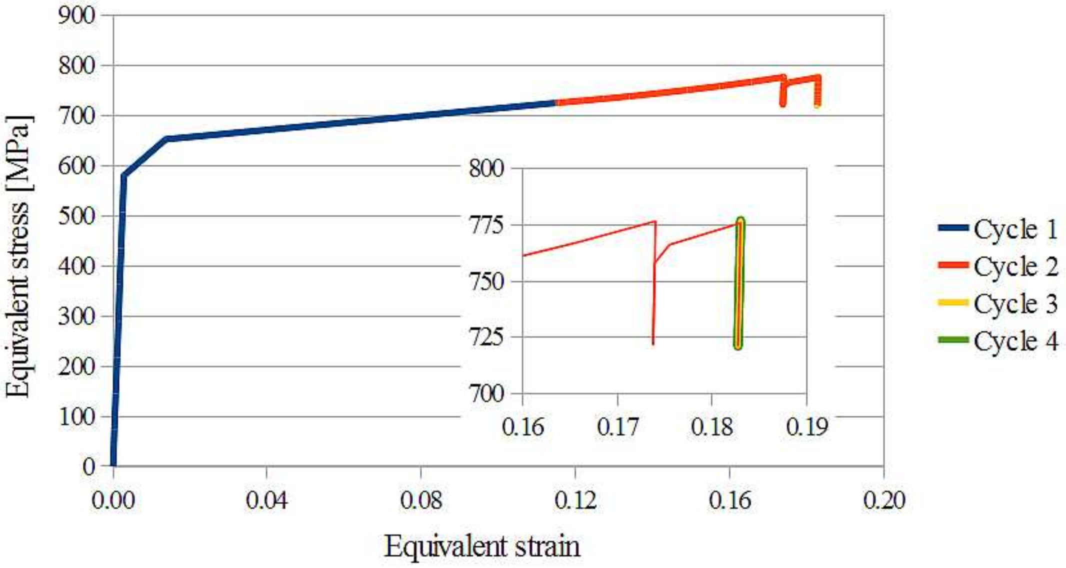

Figure 6.4: Equivalent stress versus equivalent strain for uniaxial tension and cyclic torsion.

Characteristics of individual stress components as a function of the number of cycles and the strain are shown in *Figs 6.5* and *6.6*. According to the assumed loading scenario, during the first cycle only the normal component of the stress changes up to the prescribed value and stays constant during the next part of the process. On the contrary, the shear component of the stress is activated from the second cycle when the torque is applied and oscillates with constant amplitude during the next three cycles. Only one hysteresis loop is created during the second cycle and since then the material does not dissipate energy. Such behaviour indicates clearly fast shakedown process, which is beneficial from the point of view of the fatigue life of the structure.

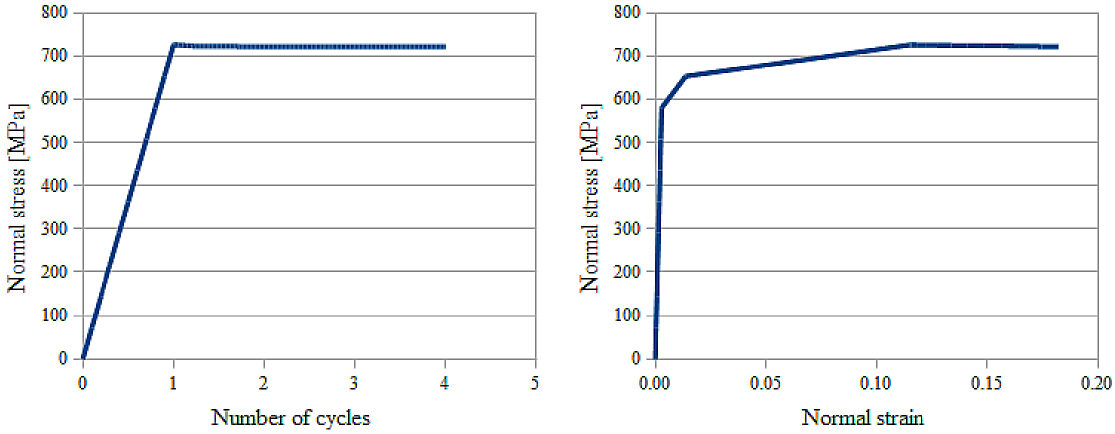

Figure 6.5: Normal stress as a function of cycle number and normal strain.

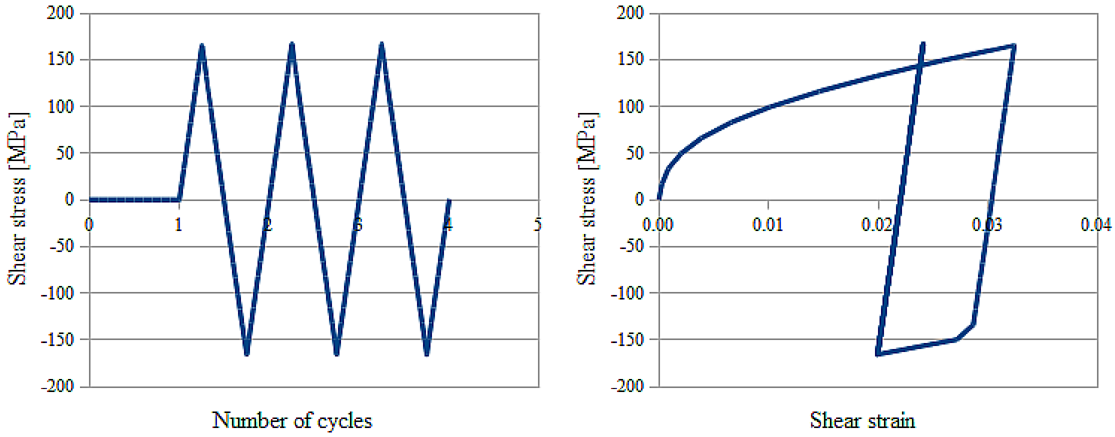

Figure 6.6: Shear stress as a function of cycle number and shear strain.

The accumulated plastic strain starts to increase during the first cycle and reaches a constant level during the second cycle (*Fig. 6.7*). It turns out that after the initial stretch and single torsion cycle the yield surface attains the maximum size which is not modified by further loading. As a result, the material shakes down and the structure starts working without further dissipation of the energy. The phase transition is initiated at the end of the tensile loading and reaches the saturation level very quickly during the first torsion cycle.

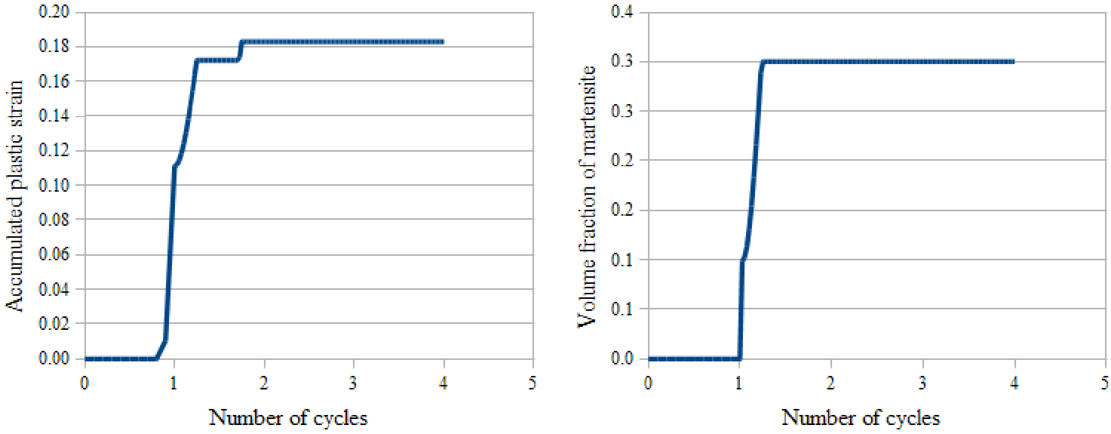

Figure 6.7: Accumulated plastic strain and volume fraction of martensite as a function of the number of cycles.

6.3. Case 2: torsion with cyclic tension

Thin-walled cylinder, initially twisted and then subjected to uniaxial cyclic tension and compression, is analysed (*Fig. 6.8*).

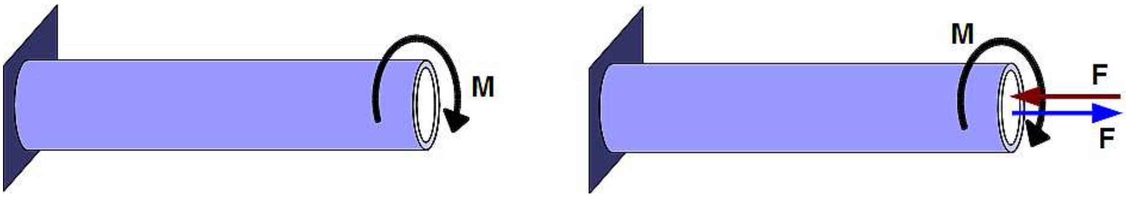

Figure 6.8: Thin-walled cylinder subjected to torsion and cyclic tension/compression.

The loading trajectory in the stress space is shown in *Fig. 6.9*. After loading up to the point when the phase transformation starts, the cylinder is subjected to tension and compression cycles in such a manner that the equivalent strain stays below 0.2.

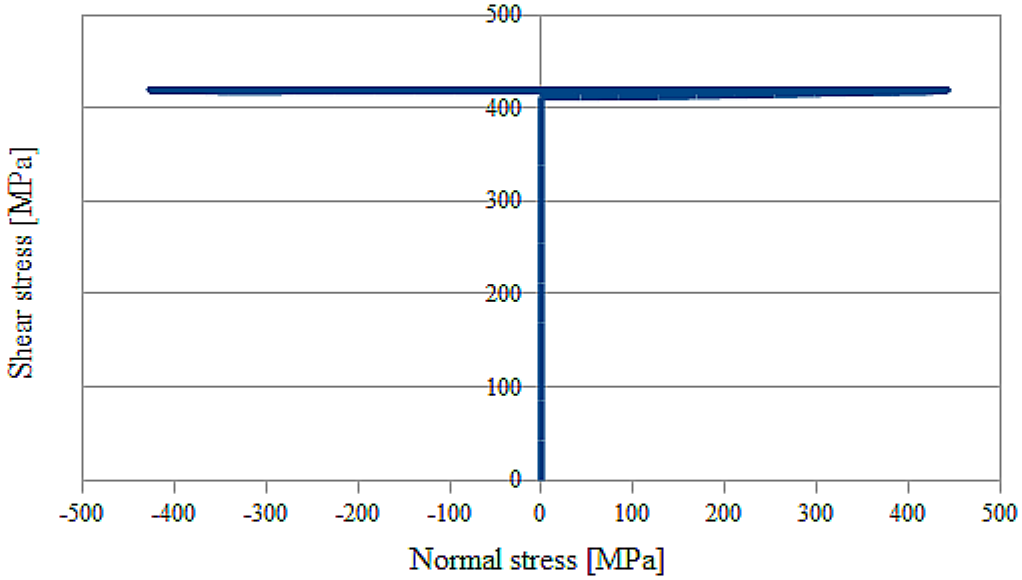

Figure 6.9: Loading trajectory in the stress space for torsion with cyclic tension and compression.

The equivalent stress as a function of the equivalent strain is shown in *Fig. 6.10*. One can observe that like in the case of uniaxial tension and cyclic torsion, the energy is not dissipated starting from the third cycle..

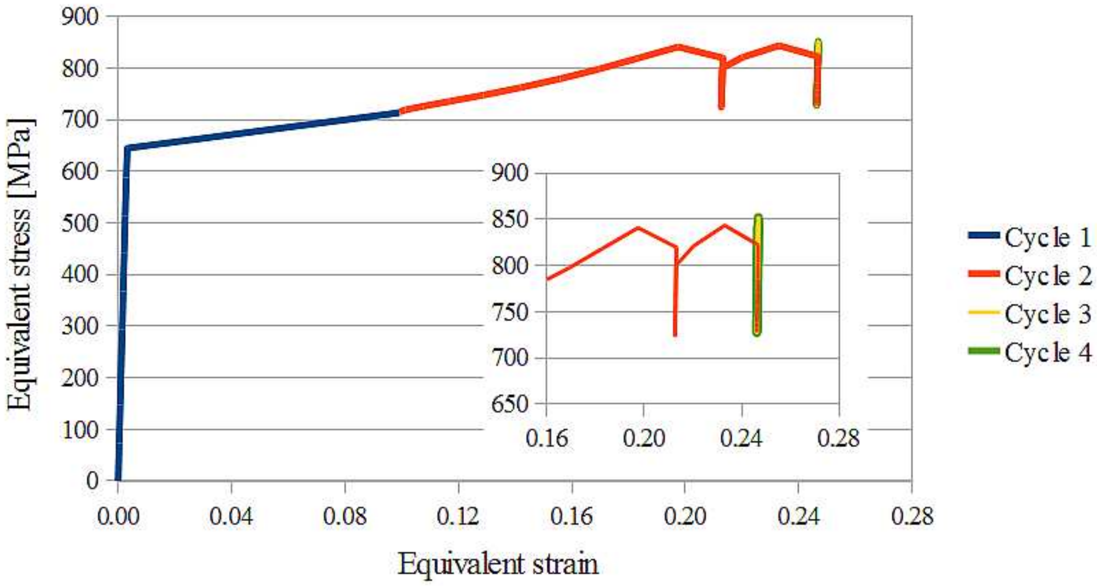

Figure 6.10: Equivalent stress versus equivalent strain for torsion and cyclic tension/compression.

Stress components as a function of the number of cycles and the strain are shown in *Figs 6.11* and *6.12*. During the first cycle the shear component of stress increases to the level which assures initiation of the plastic strain-induced transformation. The normal component of the stress is activated starting from the second cycle when the tension is applied and oscillates with constant amplitude during the next three cycles. There is only one hysteresis loop developed during the second cycle and next material stops dissipating energy.

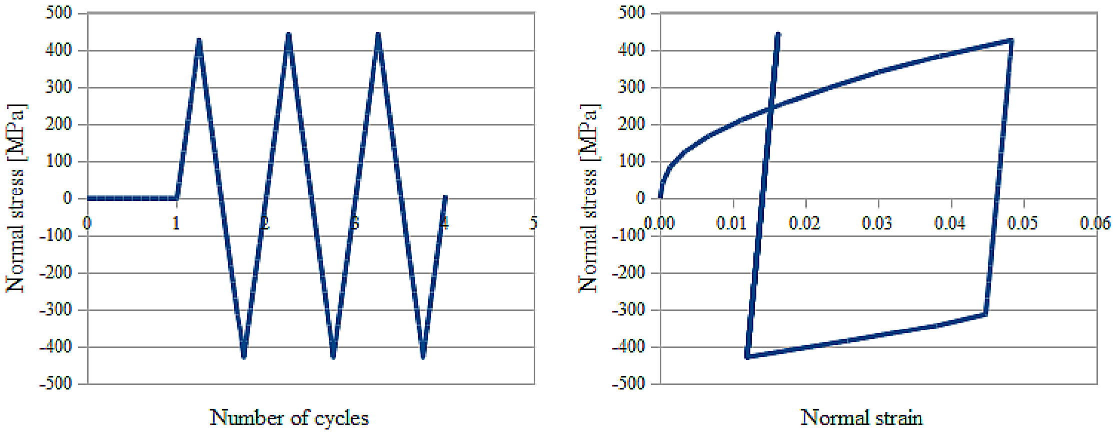

Figure 6.11: Normal stress as a function of cycle number and normal strain.

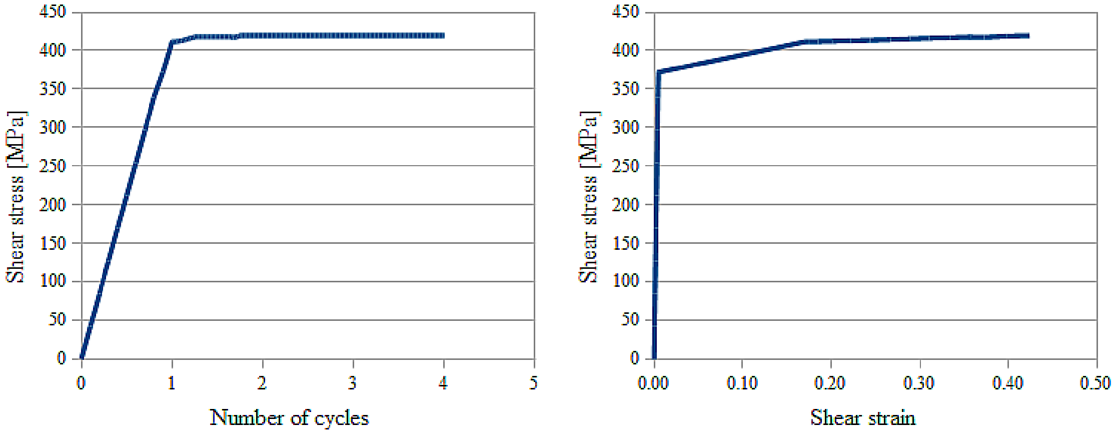

Figure 6.12: Shear stress as a function of cycle number and shear strain.

The phase transition is initiated during the first cycle of torsion and reaches the saturation level immediately after the tension process starts in the course of the second load cycle (*Fig. 6.13*). The accumulated plastic strain stops increasing during the second cycle just after the compression, which indicates the fact that the material shakes down and no further energy dissipation is observed. Such a fast shakedown process is again beneficial for the fatigue life of the structure.

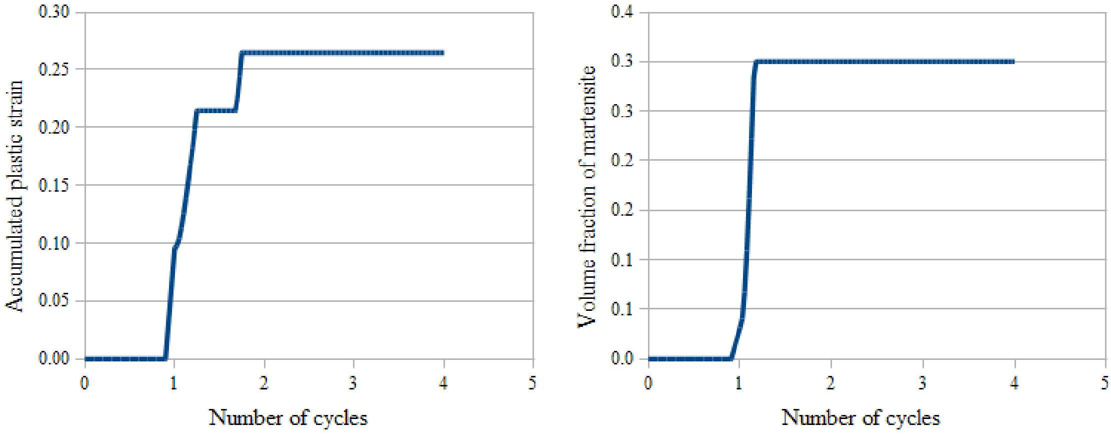

Figure 6.13: Accumulated plastic strain and volume fraction of martensite as functions of the number of cycles.

The results presented in *Figs 6.4* and *6.10* were obtained for two different values of the Bauschinger parameter: $\beta = 0.9$ and $\beta = 1.0$. As the shakedown is reached at the same moment, no matter whether the Bauschinger parameter was equal to 0.9 or 1.0, the conclusion can be drawn that the main cause of “accelerated“ shakedown in the case of analysed material is the phase transformation process. The explanation consists in the fact that the austenitic micro-structure is gradually replaced by the elastic martensite inclusions. This mechanism substantially reduces dissipation of plastic power on cycle. It is worth pointing out, that similar accelerated shakedown occurs for both combined loadings: tension with cyclic torsion (case 1) and torsion with cyclic tension (case 2). This conclusion should be regarded as important contribution to the design process of structures manufactured of metastable materials subjected to cyclic loads at cryogenic temperatures. In particular, partial phase transformation may turn out to be beneficial for the enhancement of fatigue life of structures applied at cryogenic temperatures.

7. DESIGN OF THIN-WALLED STRUCTURES UNDERGOING PHASE TRANSFORMATION

7.1. Thin-walled corrugated shells

Bellows expansion joints belong to thin-walled structures of high flexibility, commonly applied in compensation systems (*Fig. 7.1*). They are used to compensate for the relative motion of two adjacent assemblies subjected to thermal cycles or service loads. Bellows are frequently used in extreme conditions, comprising various temperature ranges and load types, which makes them a class of highly engineered structures that need to be correctly designed, manufactured and installed. Design of

Figure 7.1: Examples of bellows expansion joints (CERN).

expansion joints requires taking into account working conditions such as the piping system layout, flowing medium, pressure, temperature and possible motions. Equally important is the specification of bellows material, which must be compatible with the flowing medium, the external conditions and the operating temperatures [67].

The bellows expansion joints are crucial elements for systems working at cryogenic temperatures, where all structures contract significantly during cool-down process and the emerging displacements of components need to be compensated. Among many systems working at cryogenic temperatures and using this type of thin-walled structures the Large Hadron Collider (LHC), the superconducting particle accelerator currently in operation at CERN, is a good example.

The LHC is operated at superfluid helium temperature which implies the fact that the bellows expansion joints must work reliably in the range of temperatures from 293K to 1.9K. Compensation elements are usually placed in the interconnections between superconducting magnets where the deformations due to thermo-mechanical loads are localised (*Fig. 7.2*). Their main objective is to compensate for the thermal contraction of magnets and to provide continuity of beam vacuum chamber, all cryogenic lines and insulation vacuum.

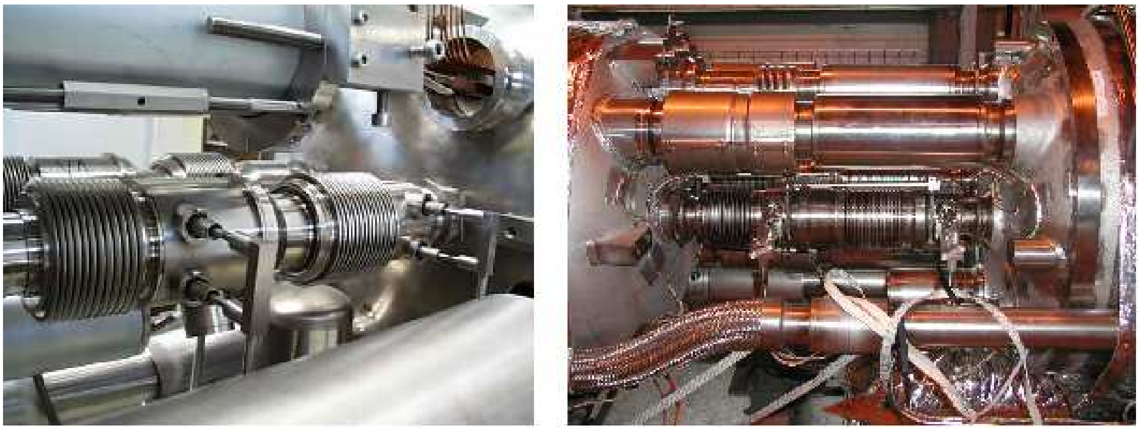

Figure 7.2: Bellows expansion joints in the LHC accelerator (CERN).

7.2. Numerical analysis of the expansion bellows

Thanks to the implementation in the finite element software of the constitutive model of a material undergoing the plastic strain-induced phase transformation, the mechanical behaviour of any structure can be easily computed and the evolution of two-phase continuum created during the transformation can be investigated. As an example, the finite element analysis of expansion bellows is presented.

The model of analysed expansions bellows is based on the geometry of components integrated in the LHC compensation system which provide continuity of the beam vacuum chambers between two adjacent dipole magnets. All geometrical parameters of the expansions joint are specified in *Table 7.1*.

Table 7.1: Basic geometrical parameters of the expansion bellows.

Material	**Thickness**	**Number of convolutions**	**Pitch**	**Inner diameter**	**Outer diameter**	**Convoluted length**
316L	0.15 mm	15	5 mm	82 mm	98 mm	80 mm

The finite element model has been built by means of 2D PLANE42 elements assuming the axial symmetry (*Fig. 7.3*). Moreover, it has been assumed that the expansion bellows is made of 316L stainless steel and is modelled for the conditions of liquid nitrogen temperature (77K). The shell is subjected to external pressure ($p = 1.3$ *bar*) and kinematically loaded according to the following program:

- asymmetric tension of *42 mm* and compression of *16 mm* in order to compare the simulations with the experimental results;
- symmetric tension and compression in the range of +/- *70 mm*, which allows us to trace the evolution of martensite in the convolutions.

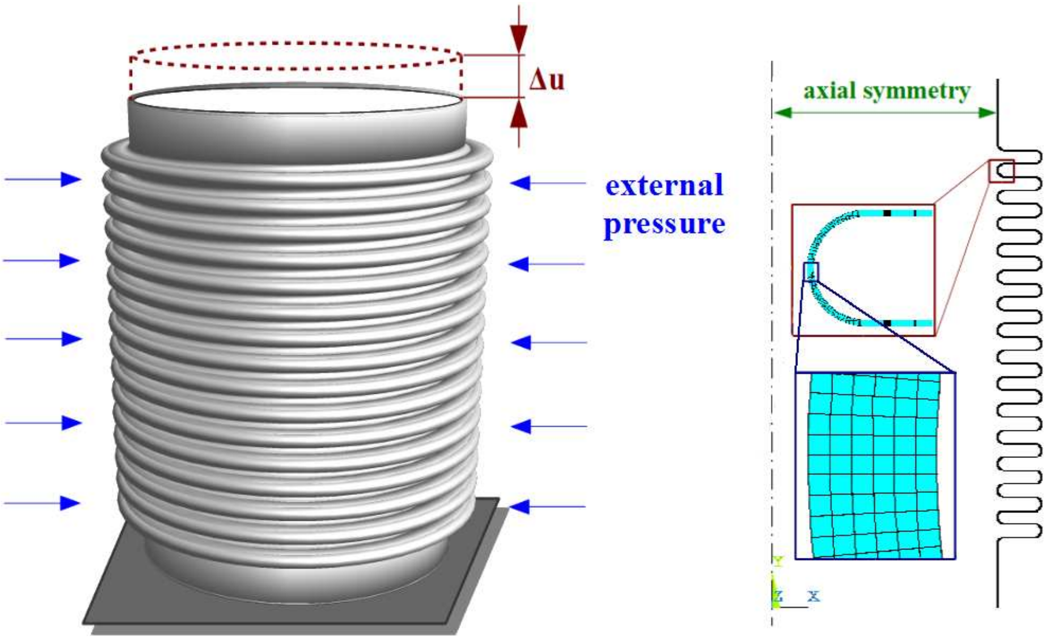

Figure 7.3: Boundary conditions and finite element mesh of expansion bellows.

The numerical and the experimental (based on [68]) results for single tension and compression of the expansion bellows are shown in *Fig. 7.4*.

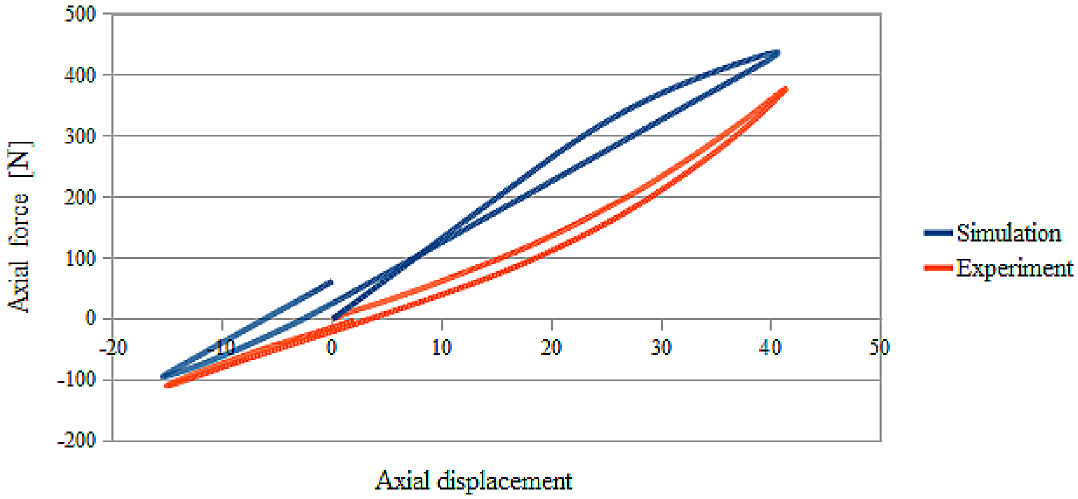

Figure 7.4: Comparison of experimental and numerically simulated cyclic force-displacement curves.

Cyclic tension and compression of the bellows within the plastic range causes slow propagation of two-phase regions in the course of loading. Sufficient plastic deformation initiates immediately the martensitic transformation which evolves at root and at crest of the convolutions. The zones containing the martensitic inclusions arise in the course of cycles gradually, providing reinforcement (hardening) in the areas subjected to the highest strains (*Fig. 7.5*).

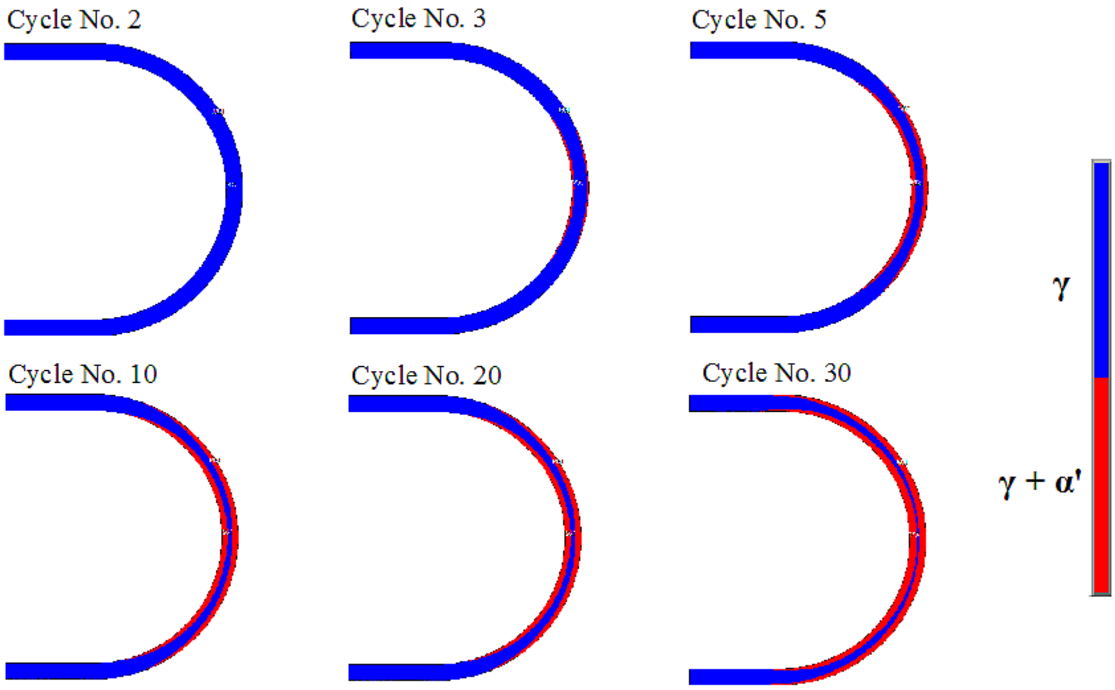

Figure 7.5: Evolution of two-phase structure in the convolutions of expansion bellows.

The quantitative evolution of the volume fraction of martensite through-thickness of the convolution is presented in *Fig. 7.6*. The amount of martensite evolves up to the assumed saturation level (here: $\xi_L = 0.3$).

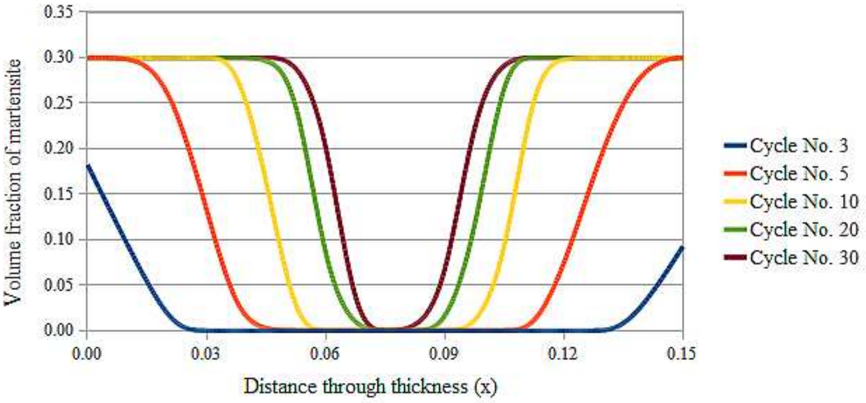

Figure 7.6: Distribution of secondary phase through-thickness of convolution.

The stress distribution in a single convolution after 30 cycles is presented in *Fig. 7.7*. One can easily notice that the highest stress intensity appears at root and at crest of the convolution – in the zones which are strengthened by the martensite.

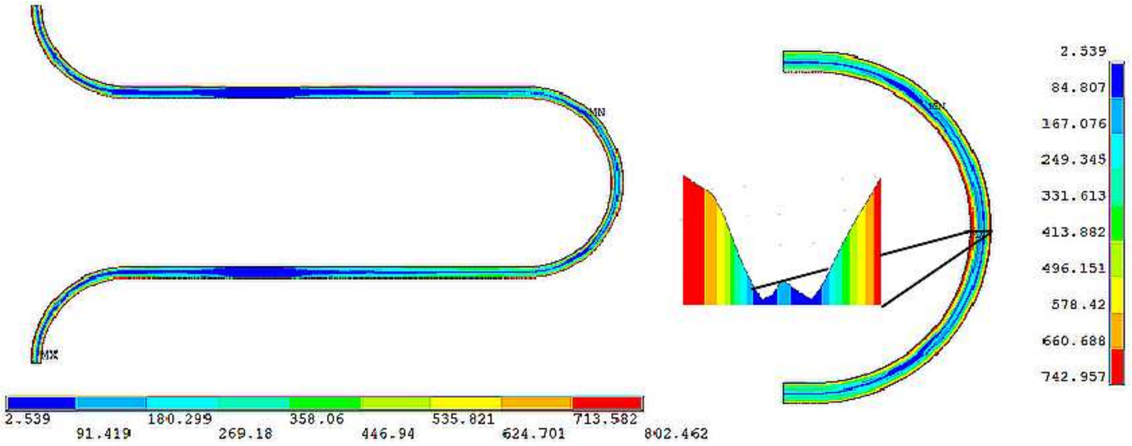

Figure 7.7: Stress distribution in expansion bellows after 30 cycles.

The distribution of the accumulated plastic strain and related distribution of the volume fraction of martensite after 30 cycles are shown in *Fig.7.8.*

The localisation of the phase transformation process coincides with so-called “skin layer” resulting from the technological process (rolling) when manufacturing fine gauge stainless steel sheets. In order to avoid premature failure of strongly hardened material (hardening due to rolling + hardening due to phase transformation) it is necessary to reduce the intensity of phase transformation down to acceptable level. On

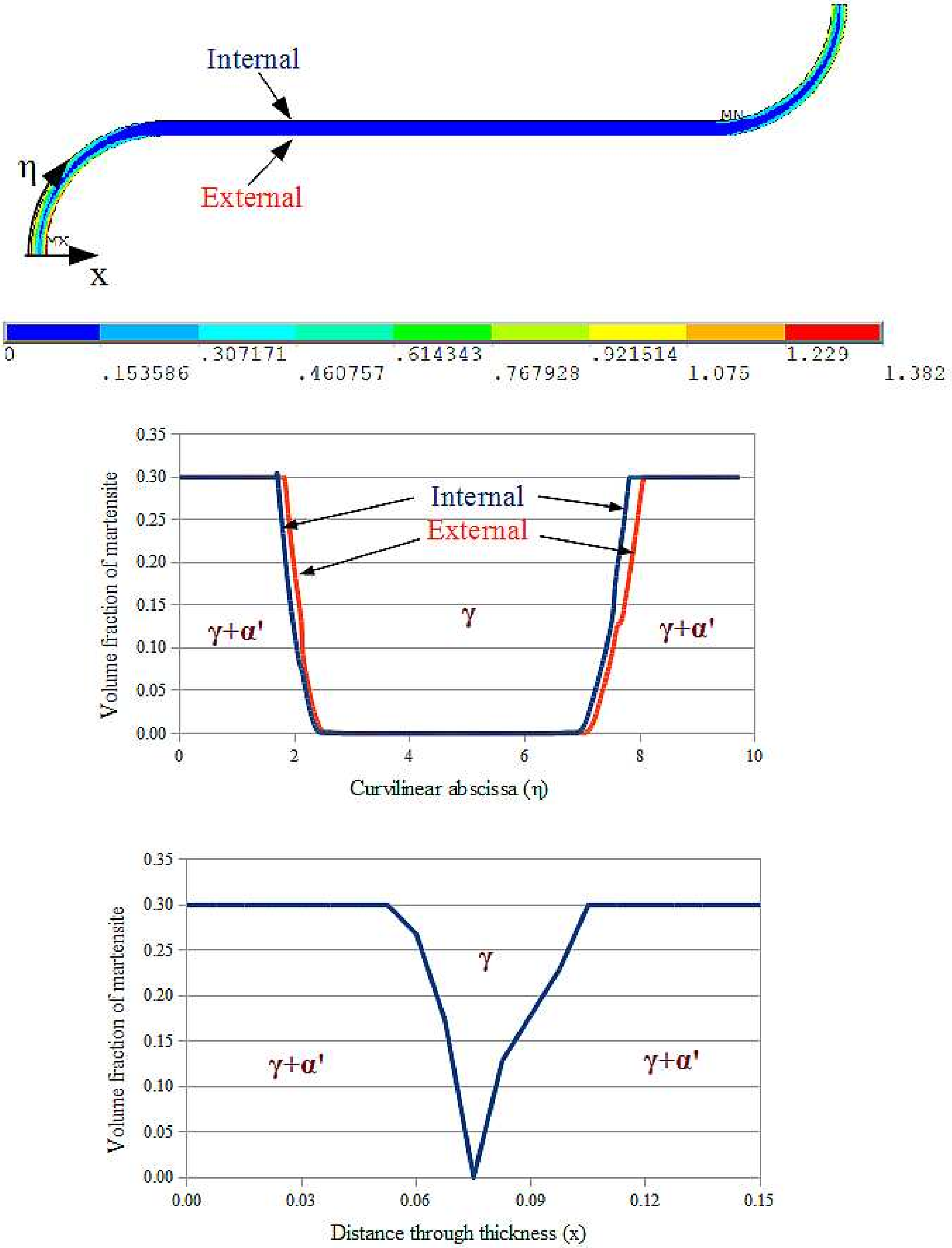

Figure 7.8: Accumulated plastic strain and volume fraction of martensite after 30 cycles.

the other hand, the existence of ellipsoidal martensitic inclusions (lenticular martensite) is beneficial for the life-time of the component because the inclusions act as macro-crack stoppers in the two-phase continuum. Therefore, a limited phase transformation is regarded as a positive contribution to enhancement of the fatigue life of thin-walled shell.

8. CONCLUSIONS

Kinematically controlled plastic strain-induced martensitic transformation may be used as a method of creating functionally graded materials with “tailored” mechanical properties. The FGM can be easily obtained within the structural members made of metastable austenitic stainless steels by loading them above the yield point and inducing the $\gamma \rightarrow \alpha'$ phase transformation. It is possible to obtain various distributions of mechanical properties, generated by two-phase micro-structure of the material, depending on the distribution of plastic strain fields as a function of the shape of structure.

In the Thesis a constitutive model of materials undergoing the plastic strain-induced phase transformation has been developed. The model is based on the linearised transformation kinetics, which is particularly relevant for the cryogenic conditions. RVE-based approach with rate independent plasticity, the Huber-Mises-Hencky yield condition, associated flow rule and mixed hardening model was used. The evolution of effective properties of material due to the evolving ratio between the parent and the secondary phase is included in the model thanks to the Mori-Tanaka homogenisation performed at each step of the non-linear analysis. The constitutive model has been implemented in the finite element software (ANSYS) by means of the external procedure USERPL, which incorporates the user defined plasticity law.

The constitutive model was used to compute analytically the 1D cases: tension/compression of rods, bending of rectangular beams and torsion of circular rods. The results of the analyses were then cross-checked with the experimental data and the FE simulations. The results obtained for circular rods subjected to torque as well as for rectangular beams subjected to bending were presented as examples of functionally graded structural members obtained via the plastic strain-induced phase transformation.

Thanks to the implementation of the constitutive model in the finite element code, the mechanical behaviour of any structure working at cryogenic temperatures and undergoing the phase transformation can be computed. As an example, a thin-walled cylinder (tube) subjected to combined loads and a expansion bellows (thin-walled shell) subjected to combined and cyclic loads were studied including the propagation of the phase transformation regions.

In the recent years, the applications of cryogenic technologies increased rapidly what generated the problem of correct design of engineering systems working in such extreme conditions. Constitutive modelling of materials for cryogenic temperatures becomes a key issue and has to include all physical phenomena taking place in the lattice in the extreme working conditions. Application of functionally graded structures created by the strain-induced martensitic transformation in the range of cryogenic temperatures may become a desired solution, especially taking into account the relatively easy method of production and possibility of numerical programming.

It is also possible to design optimum materials by changing the content of alloying elements in order to obtain favourable properties, such as the required maximum volume fraction of martensite at a given temperature. Such material design was performed in the case of the Large Hadron Collider compensation system where special on-purpose austenitic steel was designed and manufactured in order to reduce the intensity of phase transformation at 1.9K down to a necessary minimum.

One may ask a question related to the ratio between the gain and the technological effort when creating the functionally graded structural members (FGSM). The gain can be attributed within the following domains:

- enhanced strength of the outer, reinforced layers and resistance against mechanical damage;
- enhanced stability of FGSMs against buckling, especially in the case of columns of circular cross-section;
- enhanced resistance against fracture because of the mechanism of martensite inclusions acting as the stoppers for macro-cracks propagating in the two-phase continuum;
- enhanced fatigue life of FGSMs due to fast shakedown when subjected to cyclic loads in the presence of sustained load (verified for tension/compression and twisting configurations);
- wide range of operational conditions, the maximum temperature without evolution of γ/α' ratio being of the order of 400°C.

The technological effort is definitely small because of the following arguments:

- technology of bending or twisting is very well mastered;
- no sophisticated equipment is required – simple liquid nitrogen (77K) or helium (4.2K) bath is sufficient;
- the process is fast and the FGSM immediately ready for use;
- the only drawback consists in the necessity of cutting off small portions of the beam subjected to bending.

An example of evolving micro-structure of material created in the FGSM by means of $\gamma\rightarrow\alpha'$ phase transformation is shown in *Fig. 8.1*.

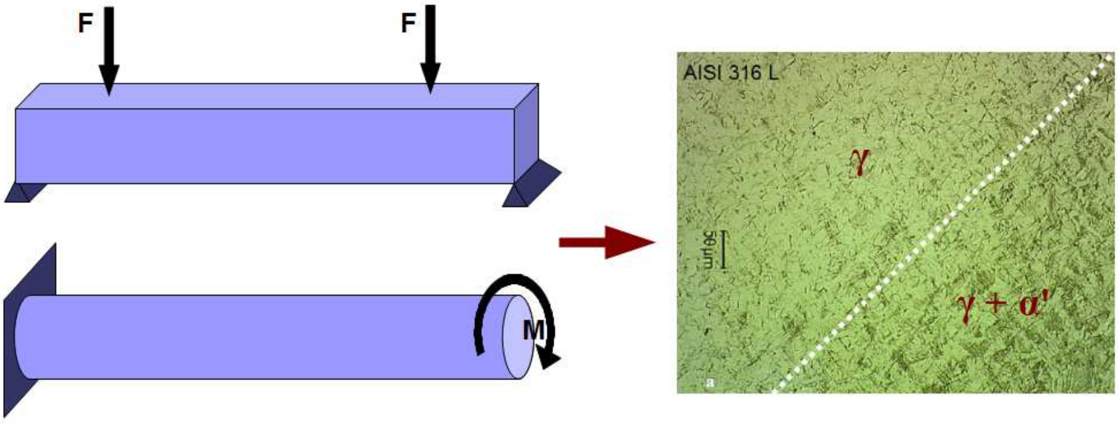

Figure 8.1: Creation of functionally graded structural members (FGSM).

BIBLIOGRAPHY

[1]: M. Cyrot, D. Pavuna, *Introduction to Superconductivity and High-Tc Materials.*, World Scientific Publishing Co. Pte. Ltd., 1992.

[2]: S. W. Van Sciver, *Helium Cryogenics.*, Plenum Press, New York, 1986.

[3]: J. W. Ekin, *Experimental Techniques for Low-Temperature Measurements*, Oxford University Press, 2006.

[4]: R. P. Reed, *Recent advantages in the development of cryogenic steels*, Supercollider, Vol. 3, pp. 91-106, 1991.

[5]: B. Skoczeń, *Compensation Systems for Low Temperature Applications*, Springer, 2004.

[6]: M. Hillert , *Phase Equilibria, Phase Diagrams and Phase Transformations: Their Thermodynamic Basis.* , Cambridge University Press, 2007.

[7]: P. Papon, J. Leblond, P. Meijer, *The Physics of Phase Transitions*, Springer, 2006.

[8]: G. Jaeger, *The Ehrenfest Classification of Phase Transitions: Introduction and Evolution*, Archive for History of Exact Sciences, Vol. 53, pp. 51-81, 1998.

[9]: L. Tisza, *The Theory of Liquid Helium.*, Physical Review, Vol. 72, pp. 838 - 854, 1947.

[10]: L. Dresner, *Transient Heat Transfer in Superfluid Helium - Part II.*, Advances In Cryogenic Engineering, Vol. 29, pp. 323–333, 1984.

[11]: M. Sitko, B. Skoczeń, *Modelling He I–He II phase transformation in long channels containing superconductors.*, International Journal of Heat and Mass Transfer, Vol. 52, pp. 9-16, 2009.

[12]: C. J. Gorter, *On the Thermodynamics of the Two Fluid Model of Helium II.*, Physica, Vol. 15, pp. 523-531, 1949.

[13]: M. Cohen, G. B. Olson, P. C. Clapp, - Proceedings of the International Conference on Martensitic Transformations, 1979.

[14]: G. B. Olson, M. Cohen, *Kinetics of strain-induced martensitic nucleation*, Metallurgical transactions, Vol. A, pp. 791-795, 1975.

[15]: S. Stupkiewicz, H. Petryk, *Finite-strain micromechanical model of stress-induced martensitic transformations in shape memory alloys.*, Materials Science and Engineering, Vol. A, pp. 126–130, 2006.

[16]: G. Kostorz, *Phase Transformations in Materials*, Wiley-VCH, 2001.

[17]: M. Koizumi, *FGM activities in Japan*, Composites Part B, Vol. 28B, pp. 1-4, 1997.

[18]: Y. Miyamoto, W. A. Kaysser, B. H. Rabin, A. Kawasaki, R. G. Ford, *Functionally graded materials: design, processing and applications*, Springer, 1999.

[19]: J. D. Eshelby, *The determination of the elastic field of an ellipsoidal inclusion and related problems*, Proceedings of the Royal Society, Vol. A241, pp. 376-396, 1957.

[20]: I. Doghri , A. Ouaar, *Homogenization of two-phase elasto-plastic composite materials and structures. Study of tangent operators, cyclic plasticity and numerical algorithms.*, International Journal of Solids and Structures, Vol. 40, pp. 1681–1712, 2003.

[21]: I. Doghri, C. Friebel, *Effective elasto-plastic properties of inclusion-reinforced composites. Study of shape, orientation and cyclic response.*, Mechanics of Materials, Vol. 37, pp. 45-68, 2005.

[22]: I. Doghri, L. Tinel, *Micromechanical modeling and computation of elasto-plastic materials reinforced with distributed-orientation fibers.*, International Journal of Plasticity, Vol. 21, pp. 1919–1940, 2005.

[23]: O. Pierard, C. Gonzalez, J. Segurado, J. LLorca, I. Doghri, *Micromechanics of elasto-plastic materials reinforced with ellipsoidal inclusions.* , International Journal of Solids and Structures, Vol. 44, pp. 6945–6962, 2007.

[24]: G.W. Greenwood, R.H. Johnson, *The deformation of metals under small stresses during phase transformation.*, Proceedings of Royal Society A , Vol. 283, pp. 403-422, 1965.

[25]: G. B. Olson, M. Cohen, *Kinetics of strain-induced martensitic nucleation*, Metallurgical transactions, Vol. A(6), pp. 791-795, 1975.

[26]: T. Narutani, G. B. Olson, M. Cohen, *Constituitve flow relations for austenitic steels during strain-induced martensitic transformation*, Journal de physique, Vol. 43(12), pp. 429-434, 1982.

[27]: R. G. Stringfellow, D. M. Parks, G. B. Olson , *Constitutive model for transformation plasticity accompanying strain-induced martensitic transformations in metastable austenitic steels*, Acta Metallurgica, Vol. 40(7), pp. 1703-1716, 1992.

[28]: Y. Tomita, T. Iwamoto, *Constitutive modeling of TRIP steel and its application to the improvement of mechanical properties*, International Journal of Mechanica Sciences, Vol. 37(12), pp. 1295-1305, 1995.

[29]: T. Iwamoto, T. Tsuta, Y. Tomita, *Investigation on deformation mode dependence of strain-induced martensitic transformation in TRIP steels and modelling of transformation kinetics*, International Journal of Mechanical Sciences, Vol. 40, pp. 173-182, 1998.

[30]: F. D. Fischer, E. R. Oberaigner, K. Tanaka, F. Nishimura, *Transformation induced plasticity revised an updated formulation*, International Journal of Solids and Structures, Vol. 35, pp. 2209-2227, 1998.

[31]: J. M. Diani, H. Sabar, M. Berveiller, *Micromechanical modelling of the transformation induced plasticity (TRIP) phenomenon in steels.*, International Journal of Engineering Sciences, Vol. 33(13), pp. 1921-1934, 1995.

[32]: J. M. Diani, D. M. Parks, *Effects of strain state on the kinetics of strain-induced martensite in steels*, Journal of the Mechanics and Physics of Solids, Volume , Issue 9, 14 September 1998, Pages , Vol. 46, pp. 1613-1635, 1998.

[33]: V. I. Levitas, A. V. Idesman, G. B. Olson, *Condinuum modeling of strain-induced martensitic transformation at shear band intersections*, Acta Mater., Vol. 47, pp. 219-

233, 1992.

[34]: F. D. Fischer, G. Reisner, E. Werner, K. Tanaka, G. Cailletaud, T. Antretter, *A new view on transformation induced plasticity (TRIP)*, International Journal of Plasticity, Vol. 16, pp. 723-748, 2000.

[35]: M. Cherkaoui, M. Berveiller, H. Sabar, *Micromechanical modeling of martensitic transformation induced plasticity (TRIP) in austenitic single crystals.*, International Journal of Plasticity, Vol. 14(7), pp. 597-626, 1998.

[36]: M. Cherkaoui, M. Berveiller, X. Lemoine, *Couplings between plasticity and martensitic phase transformation: overall behavior of polycrystalline TRIP steels*, International Journal of Plasticity, Vol. 16, pp. 1215–1241, 2000.

[37]: T. Iwamoto, T. Tsuta, *Computational simulation of the dependence of the austenitic grain size on the deformation behavior of TRIP steels.*, International Journal of Plasticity, Vol. 16, pp. 791-804, 2000.

[38]: Y. Tomita, T. Iwamoto, *Computational prediction of deformation behavior of TRIP steels under cyclic loading*, International Journal of Mechanical Sciences, Vol. 43(9), pp. , 2001.

[39]: H. N. Han, C. G. Lee, C.-S. Oh, T.-H. Lee, S.-J. Kim, *A model for deformation behavior and mechanically induced martensitic transformation of metastable austenitic steel.*, Acta Materialia, Vol. 52, pp. 5203–5214, 2004.

[40]: W.J. Dan, W.G. Zhang, S.H. Li, Z.Q. Lin, *A model for strain-induced martensitic transformation of TRIP steel with strain rate.*, Computational Materials Science, Vol. 40, pp. 101-107, 2007.

[41]: G. Baudry, R. Pineau, *Influence of strain-induced martensitic transformation on teh low-cycle fatigue behavior of a stainless steel.*, Materials Science and Engineering, Vol. 28, pp. 229-242, 1977.

[42]: J.-B. Vogt, J. Foct, C. Regnard, G. Robert, J. Dhers, *Low-temperature fatigue of 316L and 316LN austenitic stainless steels.*, Metallurgical Transactions A, Vol. 22A, pp. 2385-2392, 1991.

[43]: M. Botshekan, S. Degallaix, Y. Desplanques, *Influence of martensitic transformation on the low-cycle fatigue behaviour of 316LN stainless steels at 77 K.*, Materials Science and Engineering, Vol. A234-236, pp. 463-466, 1997.

[44]: M. Botshekan, S. Degallaix, Y. Desplanques, J. Polak, *Tensile and LCF properties of AISI 316LN SS at 300 and 77 K.*, Fatigue & Fracture of Engineering Materials & Structures, Vol. 21, pp. 651-660, 1998.

[45]: K. Suzuki, J. Fukakura, H. Kashiwaya, *Croegenic fatigue properties of 304L and 316L stainless steels compared to mechanical strength and increasing magnetic permeability.*, American Society for Testing and Materials, Vol. , pp. 190-197, .

[46]: C. Garion, B. Skoczeń, *Modeling of plastic strain-induced martensitic transformation for cryogenic applications*, Journal of Applied Mechanics, Vol. 69, pp. 755-762, 2002.

[47]: C. Garion, B. Skoczeń, S. Sgobba, *Constitutive modelling and identification of parameters of the plastic strain-induced martensitic transformation in 316L stainless steel at cryogenic temperatures*, International Journal of Plasticity, Vol. 22, pp. 1234-1264, 2006.

[48]: B. Skoczeń, *Functionally graded structural members obtained via the low temperature strain induced phase transformation*, International Journal of Solids and Structures, Vol. 44, pp. 5182-5207, 2007.

[49]: M. Sitko, B. Skoczeń, A. Wróblewski, *FCC-BCC phase transformation in rectangular beams subjected to plastic straining at cryogenic temperatures.*, International Journal of Mechanical Sciences, Vol. 52(7), pp. 993-1007, 2010.

[50]: Z. Mróz, G. Ziętek, *Dwupowierzchniowy model wzmocnienia plastycznego przy przemianie fazowej i deformacji cyklicznej.*, Acta Mechanica et Automatica, Vol. 1(1), pp. 67-70, 2007.

[51]: K. J. Lee, M. S. Chun, M. H. Kim, J. M. Lee, *A new constitutive model of austenitic stainless steel for cryogenic applications*, Computational Materials Science, Vol. 46, pp. 1152-1162, 2009.

[52]: M.-G. Lee, S.-J. Kim, H. N. Han, *Crystal plasticity finite element modeling of mechanically induced martensitic transformation (MIMT) in metastable austenite.*, International Journal of Plasticity, Vol. 26, pp. 688–710, 2010.

[53]: R. Hill, *A self-consistent mechanics of composite materials.*, Journal of the Mechanical and Physical Solids, Vol. 13, pp. 213-222, 1965.

[54]: D. Gross, T. Seelig, *Fracture mechanics: with an introduction to micromechanics*, Springer, 2006.

[55]: Z. Hashin, S. Shtrikman, *A variational approach to the theory of the elastic behaviour of multiphase materials.*, Journal of the Mechanics and Physics of Solids, Vol. 211, pp. 127-140, 1963.

[56]: A. V. Hershey, *The elasticity of an isotropic aggregate of anisotropic cubic crystal.*, Journal of Applied Mechanics, Vol. 21, pp. 236-240, 1954.

[57]: E. Kröner, *Berechnungen der elastischen Konstansten des Vielkristalls aus den Konstanten des Einkristalls.*, Zeitschrift für Physik, Vol. 151, pp. 504-518, 1958.

[58]: T. Mori, K. Tanaka, *Average stress in matrix and average energy of materials with mistfitting inclusions*, Acta Metallurgica, Vol. 21, pp. 571-574, 1973.

[59]: M. Życzkowski, *Combined loadings in the theory of plasticity*, PWN Polish Scientific Publishers, 1981.

[60]: *Guide to ANSYS User Programmable Features*, ANSYS Release 9.0 Documentation.

[61]: *ANSYS Elements Reference*, ANSYS Release 9.0 Documentation.

[62]: *ANSYS, Inc. Theory Reference*, ANSYS Release 9.0 Documentation.

[63]: C. Garion, B. Skoczeń, S. Sgobba, *Constitutive modelling and identification of parameters of the plastic strain-induced martensitic transformation in 316L stainless*

steel at cryogenic temperatures, International Journal of Plasticity, Vol. 22(7), pp. 1234-1264, 2006.

[64]: J. W. Morris, J. W. Chan, Z. Mei, *The influence of deformation-induced martensite on the cryogenic behavior of 300-series stainless steels*, Cryogenics, Vol. 32, ICMC Supplement, pp. 78-85, 1992.

[65]: *The Ehrenfest Classification of Phase Transitions: Introduction and Evolution.*, ANSYS Release 9.0 Documentation.

[66]: I. Roth, M. Kübbeler, U. Krupp, H.-J. Christ, C.-P. Fritzen, *Crack initiation and short crack growth in metastable austenitic stainless steel in the high cycle fatigue regime.*, Procedia Engineering, Vol. 2, pp. 941–948, 2010.

[67]: *Standards of the Expansion Joint Manufacturers Association, Inc.*, Expansion Joint Manufacturers Association, Inc., 6th edition, 1993.

[68]: C. Garion, *Material and structural mechanical modelling and reliability of thin-walled bellows at cryogenic temperatures. Application to LHC compensation system.* - PhD Thesis, Universite Blaise Pascal, Clermont Ferrand, France, 2003.

ILLUSTRATION INDEX